

UNIVERSITÀ DEGLI STUDI DI NAPOLI FEDERICO II



# Chemical Sciences Doctorate

XXXI CYCLE

*Dynamics and structure of hydrophilic polymers at  
the interface between two surfaces:*

*Smart Sealing in Short Time*

**Tutors:**

Prof. Finizia Auriemma

Prof. Claudio De Rosa

**Candidate:**

Annalisa Bellissimo

**Supervisor:**

Prof. Pompea Del Vecchio

**PhD School Coordinator:**

Prof. Luigi Paduano

UNIVERSITÀ DEGLI STUDI DI NAPOLI FEDERICO II



# Dottorato di Ricerca in Scienze Chimiche

XXXI CYCLE

*Dinamica e struttura di polimeri idrofilici  
all'interfaccia tra due superfici:  
Smart Sealing in Short Time*

**Tutor:**

Prof. Finizia Auriemma

Prof. Claudio De Rosa

**Relatore:**

Prof. Pompea Del Vecchio

**Candidata:**

Annalisa Bellissimo

**Coordinatore:**

Prof. Luigi Paduano





# Contents

Preface .....	v
Chapter 1 Introduction .....	1
1.1 Polyvinil-alcohol (PVA).....	2
1.1.1 PVA synthesis .....	3
1.1.2 PVA properties: influence of H-bonds .....	3
1.1.3 Crystalline structure of PVA .....	5
1.2 Welding between two polymer surfaces .....	7
1.3 Aim of the project.....	12
References .....	13
Chapter 2 Materials and Methods .....	17
2.1 Materials .....	18
2.1.1 Film preparation .....	21
2.1.2 Removal of additives from PVA-based commercial films ...	23
2.1.3 Film conditioning at controlled relative humidity.....	23
2.2 Methods .....	24
2.2.1 Wide Angle X-ray Scattering (WAXS).....	24
2.2.2 X-ray fiber diffraction .....	25
2.2.3 Small Angle X-ray Scattering (SAXS) .....	25
2.2.4 Differential Scanning Calorimetry (DSC).....	35
2.2.5 Thermogravimetric analysis (TGA) .....	36
2.2.6 Mechanical tests .....	36
2.2.7 T-Peel tests .....	36
2.2.8 Dynamic Vapor Sorption (DVS).....	37
2.2.9 Rheometry .....	38





A.1. Attenuated Total Reflectance characterization (ATR) .....	211
A.2. Headspace Gas-Chromatography.....	215
A.3. Nuclear Magnetic Analysis characterization (NMR) .....	215
A.4. Conditioning at controlled relative humidity (RH).....	221
References.....	223



# Preface

Over the past years, a huge interest is raised towards hydrophilic and biocompatible polymers. Themes as degradability, recyclability and biocompatibility of materials have been central topics in the last few decades. This is the motivation that has impelled the study of this particular class of polymers.

In this scenario, Poly vinyl Alcohol (PVA) is a promising material, thanks to the above-mentioned characteristics and its good solubility in water. The versatile properties allow a potential use in various fields, spreading from medical and pharmaceutical applications to textile industry. In most of the applications, because of the polymer hydrophilicity, the interaction between PVA and water affects the final properties, both in solution and in the solid state, as film or gel.

This project aims at investigating the processes occurring at the interface during the welding of two PVA surfaces in presence of water. An in-depth study of these phenomena is an interesting academic topic and, at the same time, can bring useful applicative implications in industrial field.

The present thesis is articulated as it follows. In Chapter 2 the materials analyzed in the thesis and the methods adopted for their characterization are illustrated. In Chapter 3 the neat PVA components and

characterized in detail, as far as the crystal structure, thermal and mechanical properties, with the aim of establishing the basic features of the samples in the as received state. The crystallization kinetics of the PVA samples is also analyzed in anhydrous conditions to establish the crystallization time scale of our grades in absence of water and at high

temperatures. In the Chapter 4 the effect of water inside the PVA film is analyzed by measuring the diffusion coefficient, probing its ability to dissolve PVA crystals, and the plasticizing role of water on amorphous phase. In addition, after amorphization of PVA by effect of water, the crystallization of PVA is analyzed during water evaporation. The aim of these measurements is establishing the relevant time scale for water to trigger phenomena at PVA interface possibly involved in the welding process, namely PVA dissolution in the addition step and PVA re-crystallization during evaporation. The diffusion of PVA chains in solutions in the dilute up to concentrate regime, is measured in Chapter 5, using conditions mimicking the concentration of PVA in the water layer used as adhesive, in the industrial welding process.

The key factors inducing welding in short time, with minimum amount of water are identified, and a model for the welding process of PVA is proposed. The last chapter is devoted to the conclusions, and the outlooks emerging from our research are also delineated.

# Chapter 1

## Introduction

*La professione del ricercatore deve tornare alla sua tradizione di ricerca per l'amore di scoprire nuove verità. Poiché in tutte le direzioni siamo circondati dall'ignoto e la vocazione dell'uomo di scienza è di spostare in avanti le frontiere della nostra conoscenza in tutte le direzioni, non solo in quelle che promettono più immediati compensi o applausi.*

*Enrico Fermi*

The comprehension of mechanisms that drive the dynamics of hydrophilic polymer chains at the interface between two surfaces is relevant for fundamental research as well as for application purposes. In particular, understanding all the involved processes at molecular level is useful to clarify and optimize the welding mechanism between hydrophilic polymers, identifying the key parameters which control an efficient sealing in a short time. In this framework, Polyvinil-alcohol (PVA) is selected as hydrophilic polymer and welding between polymer layers is carried out using the water as diffusivity enhancer.

### **1.1 Polyvinil-alcohol (PVA)**

Polyvinil-alcohol (PVA) is a semicrystalline, hydrophilic and biocompatible polymer with excellent film forming properties. As a water-soluble synthetic polymer, it has found a significant role in many industrial applications.

PVA, especially as hydrogel, is an ideal candidate for biomaterials [1]–[4]. Indeed, it is non-toxic, non-carcinogenic, and bioadhesive in nature. It also shows a high degree of swelling in water (or biological fluids) and a rubbery and elastic nature and therefore closely simulates natural tissue and can be readily accepted into the body [4].

PVA is used also as a stabilizer in emulsions for contact lenses, as a viscosity-increasing agent in ophthalmic formulations and in other pharmaceutical application, such as medical patches and drug-delivery systems [5]–[7].

Since its ability to form films, PVA is widely used in food packaging, as coating barrier film, as well as for optical uses, like polarizer, thanks to the capacity to form PVA/iodine complex [8]–[10].

Finally, it is very suitable to use in the building industry, papermaking and in

textile production. For instance, Soltex® is a commercial non-woven fabric, made using water-soluble (PVA) fibers.

### 1.1.1 PVA synthesis

PVA was synthesized for the first time by Hermann and Haehnel in 1924 by hydrolyzing polyvinyl acetate (PVAc) in ethanol with potassium hydroxide. The monomer, vinyl alcohol, does not exist in a stable form, rearranging to its tautomer, acetaldehyde. For this reason, PVA is obtained by hydrolysis of PVAc. The hydrolysis of PVAc does not convert all the acetate groups, giving rise to PVA polymers with a certain degree of hydrolysis that represents the percent conversion of acetate groups to hydroxyl groups and depends on the extent of the reaction (Figure 1.1).

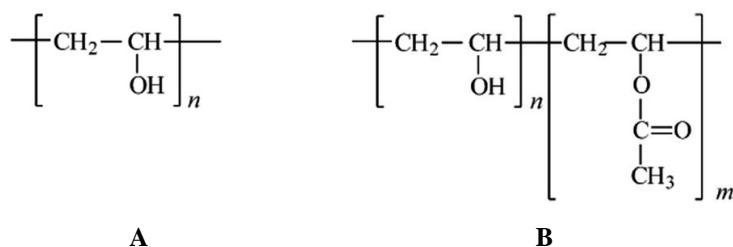


Figure 1.1: Totally (A) and partially (B) hydrolyzed PVA chains.

### 1.1.2 PVA properties: influence of H-bonds

In PVA, the polar interactions, i.e., hydrogen bonding, exert a great influence on chemical and physical properties. It is known that water solubility of PVA polymers depends on the degree of hydrolysis and molecular weight [11]. Any change in these factors influences the degree and character of

## Chapter 1

---

hydrogen bonding in the aqueous solutions, and hence the solubility of PVA. The higher the degree of hydrolysis of PVA grades, the lower the corresponding PVA solubility. Residual acetate groups in partially hydrolyzed PVA improve water solubility by disrupting polymer-polymer interchain and intrachain hydrogen bonding between hydroxyl groups and consequently promoting polymer-solvent interactions [11]. The larger number of hydroxyl groups in fully hydrolyzed PVA decreases the water solubility by promoting physical entanglements in solution through the preferential formation of polymer-polymer interchain and intrachain hydrogen bonds.

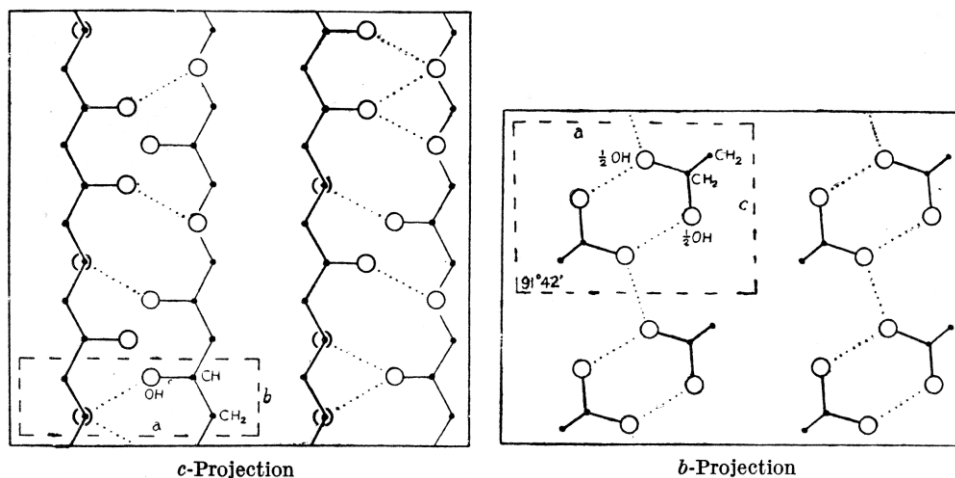
The nature of PVA implies that the polymer chains interact through formation of strong hydrogen bonds, both in the crystals and amorphous phase. For this reason, the stereoregularity of PVA was found to significantly affect the crystallizability [12]. Higher tacticity is not related to higher crystallinity. It has been demonstrated that the stereoregular structures do not favor crystallizability. Isotactic PVA (i-PVA) results in less crystalline samples than syndiotactic PVA (s-PVA) while atactic PVA is the most crystallizable form. On the other hand, both syndiotactic-rich and isotactic-rich PVA exhibited significantly higher water resistance than atactic material [12].

The reason can be sought in the differences in hydrogen bonding network. Syndiotactic samples are characterized by higher degree of intermolecular hydrogen bonding, resulting in higher solvent resistance. Their lower tendency to crystallize is probably due to a lowering in chain mobility. Isotactic form allows a higher probability of intramolecular hydrogen bonding. This interactions would lead to stiffening of the chain, lower intermolecular forces, lower crystallinity, and apparently higher solvent resistance [12].

Finally, it is worth noting that the molecular mass distribution of PVA is an important characteristic, able to affect many properties as crystallizability, mechanical strength and diffusivity.

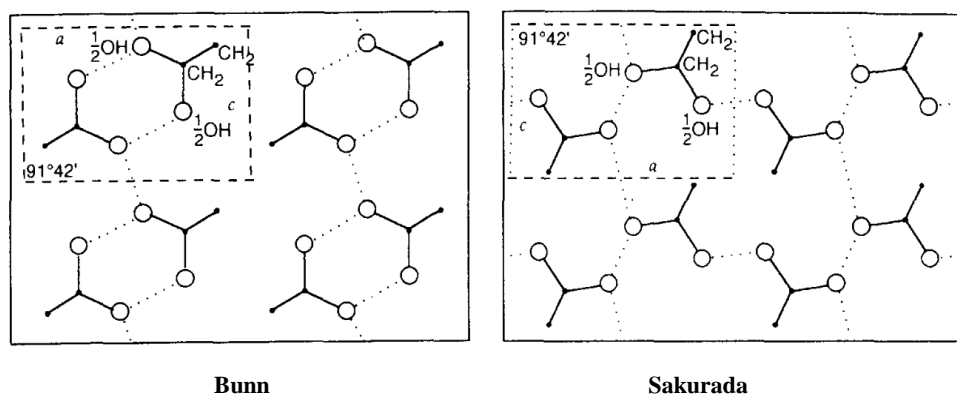
### 1.1.3 Crystalline structure of PVA

The crystalline structure of PVA has been resolved in 1948 by Bunn [13]. He proposed a crystal structure for PVA having a random distribution syndiotactic and isotactic units. The PVA crystal structure is characterized by chains in a trans-planar conformation, packed in a monoclinic unit cell with  $a=7.81\text{\AA}$ ,  $b=2.52\text{\AA}$  (chain axis),  $c=5.51\text{\AA}$  and  $\beta=91.42^\circ$ . In Figure 1.2, the  $ab$  and  $ac$  projections of the PVA crystal structure are drawn. The arrangement of molecules may be described as a layer structure; a double layer of molecules is held together by hydrogen bonds between hydroxyl groups. Each repeating monomer contains two hydroxyl sites, each with 50% occupancy, thus creating an atactic structure. Weaker Van der Waals forces operate between one double layer and the next layer. Bunn suggested two intermolecular hydrogen bonding directions, although successive molecular modeling studies showed that, in addition to the intermolecular hydrogen bonding, intramolecular hydrogen bonding is likely [14], [15].



**Figure 1.2:** *ab* and *ac* projections of the crystal structure of atactic PVA proposed by Bunn. Dotted lines represent hydrogen bonds. From [13].

A slightly different model was proposed by Sakurada et al. [16]. Both model structures are shown in Figure 1.3 for comparison. However, the Bunn model for the crystal structure of PVA fits better than the Sakurada structure the diffraction data, and corresponds to a lower packing energy [15], [17], [18]. The difference between the two structures lies in the orientation of the molecules and the resulting intermolecular hydrogen-bonding directions within a very similar lattice.



**Figure 1.3:** comparison of Bunn (on the left) and Sakurada (on the right) models for the crystal structure of atactic PVA. From [14].



---

## 1.2 Welding between two polymer surfaces

Welding between two contacting polymer surfaces, usually, is performed when the materials are brought above their glass transition temperature. This condition enhances interfaces processes that lead to the adhesion of the two surfaces. Factors such as welding temperature [19], [20] surface roughness [21], chemical bonding between the surfaces [22], the molecular weights [23]–[25] and the presence of solvents [26] directly affect the efficiency and the type of adhesion that can be achieved.

The most widespread theories for polymer-polymer adhesion at interfaces are the wetting theory and diffusion theory [25], [27]–[29].

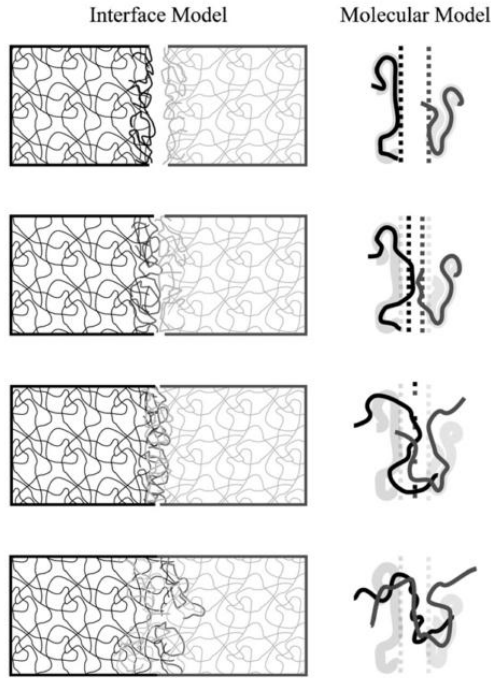
The wetting theory of adhesion is described in terms of the spreading coefficient,  $S$ , of the polymer surfaces [27]:

$$S = \Gamma_1 + \Gamma_2 - \Gamma_{12} \quad \text{eq. 1.1}$$

where  $\Gamma_1$  and  $\Gamma_2$  are the surface free energies of polymer surfaces 1 and 2, respectively, and  $\Gamma_{12}$  is the interfacial free energy between them. According to this theory, adhesion between two polymer surfaces is maximum when the surface 1 completely wets the surface 2. Values of the spreading coefficient greater than zero mean that the wetting is perfect. On the contrary, the wetting is poor when  $S$  is less than zero.

According to the second model, the welding process for an amorphous polymer is driven by the diffusion of the polymer chains [29], [30]. Figure 1.4 depicts the main steps of the model: the theory assumes that after the contact (a) a perfect wetting is established (b) and, at a certain time, the segments of the polymer chains start to diffuse across the interface (c), forming entanglements, until, at very long times, the polymer-polymer interface completely disappears becoming indistinguishable from the bulk polymer (d) [30]. The final adhesion

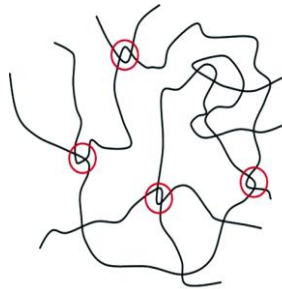
is guaranteed by the formation of chain entanglements between two contacting polymers and depends on the extent of interdiffusion and chain interpenetration across the welding interface.



**Figure 1.4:** schematic steps occurring in polymer welding via molecular interdiffusion. Adapted from [30].

The dynamics of the diffusing chains can be described by the *reptation* theory, developed by de Gennes [31] and lately redefined by Doi and Edward [32]. This model has found great success in the description of the diffusion of polymer chains in the melt and in concentrated solutions, resorting to the concept of *entanglement*. According to this model, the chain is confined in *tube-like* region and the only mechanism by which a polymer molecule diffuses is a back and forth one-dimensional Brownian motion, like a snake, within a tube created by the surrounding chains through the *entanglements*. Indeed, the

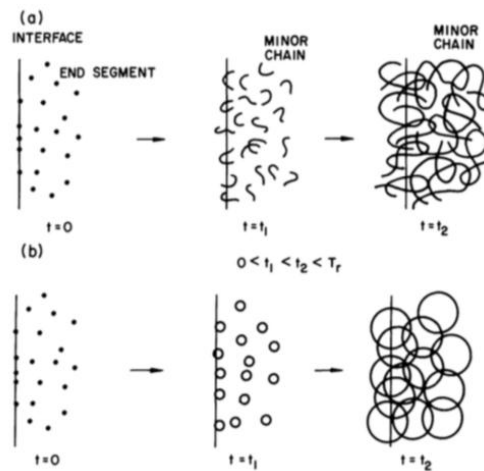
chain is topologically constrained by the *entanglements* of neighboring chains, which restrict the chain mobility in the bulk and in concentrated solutions. Qualitatively, one can envision an *entanglement* as a crossing of polymer chains (Figure 1.5) which, when subjected to a strain, remains intact and hence mechanically active. In other words, *entanglements* can be thought as the result of a temporary network, explaining the viscoelastic behavior. At a certain time, the polymer chain will be able to escape from the initial tube. This characteristic time, corresponding to the longest relaxation time of the chain, is called the *reptation time*,  $\tau_{\text{rep}}$ , and gives an idea of how long it takes for a polymer chain to draw around itself a completely new tube. From this perspective, the *reptation time* plays a key role in the sealing process because it is related to the mobility of polymer chains at the interface.



**Figure 1.5: Representation of an entangled polymer. The entanglements are highlighted with circles.**

Based on the above described diffusion model, Wool introduced the concept of *minor chains*, enriching the description of the chain motion at interface [33]. He analyzed the motion of polymer chain at shorter times than the *reptation time*. Indeed, at shorter times, short-range wriggling motion of the chain occurs. Based on this assumption, he proposed that before that the entire chain loses its initial configuration, portions of chain (i.e., minor chains) escape from the initial tube and can diffuse across the interface. As shown in Figure 1.6, the chain begins to reptate via chain ends, drawn as dots randomly distributed ( $t =$

0). This motion originates minor chains ( $t = t_1$ ) having a certain spherical envelope. The minor chains length and the correspondent spherical envelopment increase with time, as their penetration across the interface ( $t = t_2$ ). Initially, the chains have a non-Gaussian conformation due to the boundary conditions at the interface. Anyway, the conformations of the minor chains are always Gaussian in the bulk and at the interface as well. As the minor chains interdiffuse, the affected chains in the surface layer relax to Gaussian conformation.

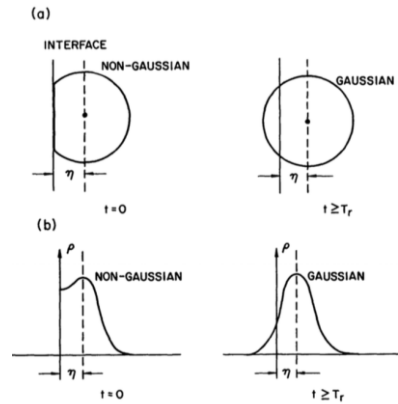


**Figure 1.6: Motion of minor chains (a) and growth of their spherical envelopments (b) during time across an interface. From [33].**

In Figure 1.7, the transition from a non-Gaussian to a Gaussian state is shown through the representation of the average shape and size of a chain (Figure 1.7-a) and of the segment density,  $\rho$ , (Figure 1.7-b), at the interface, before and after relaxation. The time required for this transition corresponds to the tube renewal time ( $T_r$ ).

Thus, according to the Wool model, the development of weld strength is due to the diffusion of minor chain at the interface and, as time approaches to the

*reptation* time, interpenetration and re-entanglement of chains are achieved obtaining at the interface the molecular properties of the bulk.



**Figure 1.7: Average shape and size of a chain (a) and the segment density,  $\rho$ , (b) at the interface before and after relaxation. From [33].**

All the models, discussed until now, describe amorphous systems and do not consider any effect due to the semicrystalline nature of such polymers. This is not surprising because the welding is a process involving, mainly, the amorphous phase. Therefore, less attention has been spent in semicrystalline polymer interfaces, both theoretically and experimentally [34].

For a more accurate comprehension of the welding process in semicrystalline polymers, the crystallization at the interface should be taken into account, in addition to the interdiffusion of polymer chains.

In particular, in the case of interfaces between semicrystalline polymers, it has been shown that the interfacial behavior depends on the location of nucleation sites. At low temperature, the nucleation occurs at the interface, hindering the interdiffusion and resulting in a small interfacial width. Increasing the temperature, the crystallization happens far away from the interface where the interdiffusion process is predominant, leading a larger interfacial width [35].

Moreover, the crystallization may induce changes at the interface causing free volume for interdiffusion and influencing the final interfacial width [36]–[38].

In conclusion, the effect of the competition or the synergy between crystallization and interdiffusion at the interface can determine the final interfacial properties.

### **1.3 Aim of the project**

In the present project, welding between two PVA films is performed by coating the film at the surface with a thin layer of water. As water is a good solvent for PVA, water acts as an adhesive triggering different processes at the interfaces.

It is reasonable to think that the welding process of PVA films is likely to involve not only the dynamics of the chains, and polymer dissolution by effect of water, but also the crystallization taking place at the interface including melting/recrystallization phenomena, nucleation and/or grown rate of the crystals, location of nuclei, etc.. Therefore, the presence of water, as plasticizing agent at the interface, may have strong effects on the segmental dynamics, the crystallization kinetics and the hydrogen bonding scheme.

With the aim to understand the welding of two PVA films triggered by water, it is crucial, in our approach, the molecular comprehension of polymer-solvent interactions and their diffusion mechanisms, as well as the role of crystallization at interface.

---

## References

- [1] H. S. Mansur, R. L. Oréface, and A. A. P. Mansur, "Characterization of poly(vinyl alcohol)/poly(ethylene glycol) hydrogels and PVA-derived hybrids by small-angle X-ray scattering and FTIR spectroscopy," *Polymer*, vol. 45, no. 21, pp. 7193–7202, 2004.
- [2] D. Zhang, W. Zhou, B. Wei, X. Wang, R. Tang, J. Nie, and J. Wang, "Carboxyl-modified poly(vinyl alcohol)-crosslinked chitosan hydrogel films for potential wound dressing," *Carbohydr. Polym.*, vol. 125, pp. 189–199, 2015.
- [3] L. Grover, "Poly ( vinyl alcohol ) modification of low acyl gellan hydrogels for applications in tissue regeneration," *Food Hydrocoll.*, no. September, 2014.
- [4] M. I. Baker, S. P. Walsh, Z. Schwartz, and B. D. Boyan, "A review of polyvinyl alcohol and its uses in cartilage and orthopedic applications," *J. Biomed. Mater. Res. - Part B Appl. Biomater.*, vol. 100 B, no. 5, pp. 1451–1457, 2012.
- [5] N. Krishna and F. Brown, "Polyvinyl alcohol as an ophthalmic vehicle. Effect on Regeneration of Corneal Epithelium.," *Am. J. Ophthalmol.*, vol. 57, pp. 99–106, 1964.
- [6] P. Colombo, R. Bettini, P. Santi, a. De Ascentiis, and N. a. Peppas, "Analysis of the swelling and release mechanisms from drug delivery systems with emphasis on drug solubility and water transport," *J. Control. Release*, vol. 39, no. 2–3, pp. 231–237, 1996.
- [7] J. C. Richardson, R. W. Bowtell, K. Mäder, and C. D. Melia, "Pharmaceutical applications of magnetic resonance imaging (MRI)," *Adv. Drug Deliv. Rev.*, vol. 57, no. 8, pp. 1191–1209, 2005.
- [8] M. H. Han, J. K. Shin, K. Il Oh, Y. J. Lee, D. H. Song, Y. Sik, Y. R. Lee, H. G. Choi, T. H. Oh, S. S. Han, and S. K. Noh, "Preparation of Recycled Poly ( vinyl alcohol ) ( PVA ) / Iodine Polarizing Film," vol. 18, no. 7, pp. 391–396, 2010.
- [9] T. Takahama, S. M. Saharin, and K. Tashiro, "Details of the intermolecular interactions in poly(vinyl alcohol)-iodine complexes as studied by quantum chemical calculations," *Polym. (United Kingdom)*,

- vol. 99, pp. 566–579, 2016.
- [10] T. M. C. Maria, R. A. de Carvalho, P. J. A. Sobral, A. M. B. Q. Habitante, and J. Solorza-Feria, “The effect of the degree of hydrolysis of the PVA and the plasticizer concentration on the color, opacity, and thermal and mechanical properties of films based on PVA and gelatin blends,” *J. Food Eng.*, vol. 87, no. 2, pp. 191–199, 2008.
- [11] R. K. Tubbs, “Sequence Distribution of Partially Hydrolyzed Poly(vinyl acetate),” *J. Polym. Sci. Part A-1 Polym. Chem.*, vol. 4, no. 3, pp. 623–629, 1966.
- [12] J. F. Kenney and G. W. Willcockson, “Structure-Property Relationships of Poly ( vinyl Alcohol ). III . Relationships between Stereo- regularity , Crystallinity , and Water Resistance in Poly ( vinyl Alcohol ),” *J. Polym. Sci. Part A-1*, vol. 4, pp. 679–698, 1966.
- [13] C. W. Bunn, “Crystal Structure of Polyvinyl Acohol,” *Nature*, vol. 161, no. 4102, pp. 929–930, 1948.
- [14] H. E. Assender and A. H. Windle, “Crystallinity in poly(vinyl alcohol). An X-ray diffraction study of atactic PVOH,” *Polymer* (., vol. 39, no. 18, pp. 4295–4302, 1998.
- [15] H. E. Assender and A. H. Windle, “Crystallinity in poly(vinyl alcohol) 2. Computer modelling of crystal structure over a range of tacticities,” *Polymer*, vol. 39, no. 18, pp. 4303–4312, 1998.
- [16] I. Sakurada, K. Fuchino, and N. Okada, “Crystal Structure of Polyvinyl Alcohol,” *Bull. Inst. Chem. Res. Kyoto Univ.*, vol. 23, pp. 78–79, 1950.
- [17] J. D. Cho, W. S. Lyoo, S. N. Chvalun, and J. Blackwell, “X-ray Analysis and Molecular Modeling of Poly (vinyl alcohol) s with Different Stereoregularities,” *Macromolecules*, vol. 32, pp. 6236–6241, 1999.
- [18] S. Krimm, C. Y. Liang, and G. B. B. M. Sutherland, “Infrared spectra of high polymers. V. Polyvinyl Acohol,” *J. Polym. Sci.*, vol. 22, pp. 227–247, 1956.
- [19] A. Yousefpour, M. Hojjati, and J. P. Immarigeon, “Fusion bonding/welding of thermoplastic composites,” *J. Thermoplast. Compos. Mater.*, vol. 17, no. 4, pp. 303–341, 2004.



- 
- [20] Y. M. Boiko, G. Guérin, V. A. Marikhin, and R. E. Prud'homme, "Healing of interfaces of amorphous and semi-crystalline poly(ethylene terephthalate) in the vicinity of the glass transition temperature," *Polymer*, vol. 42, no. 21, pp. 8695–8702, 2001.
- [21] H. J. Kim, K. J. Lee, and H. H. Lee, "Healing of fractured polymers by interdiffusion," *Polymer*, vol. 37, no. 20, pp. 4593–4597, 1996.
- [22] N. Avramova, "Study of the healing process of polymers with different chemical structure and chain mobility," *Polymer*, vol. 34, no. 9, pp. 1904–1907, 1993.
- [23] H. Zhang and R. P. Wool, "Concentration Profile for a Polymer-Polymer Interface. 1. Identical Chemical Composition and Molecular Weight," *Macromolecules*, vol. 22, no. 5, pp. 3018–3021, 1989.
- [24] C. M. Roland and G. G. A. Bohm, "Macromolecular Diffusion and the Autoadhesion of Polybutadiene," *Macromolecules*, vol. 18, no. 6, pp. 1310–1314, 1985.
- [25] W. C. Kim and H. Pak, "Interdiffusion at Interfaces of Binary Polymer Mixtures with Different Molecular Weights," vol. 20, no. 11, pp. 1323–1328, 1999.
- [26] C. B. Lim, S. Lee, and K. S. Liu, "Methanol-induced crack healing in poly(methyl methacrylate)," *Polym. Eng. Sci.*, vol. 30, no. 21, pp. 1399–1406, 1990.
- [27] E. Jabbari, E. Jabbari, N. A. Peppas, and N. A. Peppas, "Polymer-Polymer Interdiffusion and Adhesion," *J. Macromol. Sci. Part C Polym. Rev.*, vol. 34, no. 2, pp. 205–241, 1994.
- [28] A. J. Kinloch, "The science of adhesion - Part 1 Surface and interfacial aspects," *J. Mater. Sci.*, vol. 15, no. 9, pp. 2141–2166, 1980.
- [29] S. Prager, "The healing process at polymer-polymer interfaces," *J. Chem. Phys.*, vol. 75, no. 10, p. 5194, 1981.
- [30] D. Y. Wu, S. Meure, and D. Solomon, "Self-healing polymeric materials: A review of recent developments," *Prog. Polym. Sci.*, vol. 33, no. 5, pp. 479–522, 2008.
- [31] P. G. De Gennes, "Reptation of a polymer chain in the presence of fixed

- obstacles,” *J. Chem. Phys.*, vol. 55, no. 2, pp. 572–579, 1971.
- [32] S. F. Doi, M.; Edwards, *The Theory of Polymer Dynamics*. Clarendon Press: Oxford, U.K., 1986.
- [33] Y. H. Kim and R. P. Wool, “A Theory of Healing at a Polymer Polymer Interface,” *Macromolecules*, vol. 16, no. 7, pp. 1115–1120, 1983.
- [34] C. T. Lo and B. Narasimhan, “A new kinetic model for interdiffusion at semicrystalline polymer interfaces,” *Polymer*, vol. 46, no. 7, pp. 2266–2275, 2005.
- [35] C. T. Lo, F. C. Laabs, and B. Narasimhan, “Interfacial adhesion mechanisms in incompatible semicrystalline polymer systems,” *J. Polym. Sci. Part B Polym. Phys.*, vol. 42, no. 14, pp. 2667–2679, 2004.
- [36] Z. Bartczak, A. Galeski, and M. Pracella, “Spherulite nucleation in blends of isotactic polypropylene with isotactic poly(butene-1),” *J. Appl. Polym. Sci.*, vol. 54, no. 10, pp. 1513–1524, 1994.
- [37] Z. Bartczak and A. Galeski, “Changes in interface shape during crystallization in two-component polymer systems,” *Polymer*, vol. 27, no. 4, pp. 544–548, 1986.
- [38] S. K. Kumar and D. Y. Yoon, “Lattice Model for Interphases in Binary Semicrystalline/Amorphous Polymer Blends,” *Macromolecules*, vol. 22, no. 10, pp. 4098–4101, 1989.

# Chapter 2

## Materials and Methods

*Nothing exists until it is measured.*

*Niels Bohr*





[REDACTED]

The degree of hydrolysis, DH, was determined, for all the samples, by solution NMR (Nuclear Magnetic Resonance) characterization. This technique was employed also to investigate stereoregularity for PVA resin samples indicating that all samples are almost completely atactic, the syndiotactic triads *rr* being only slightly prevalent with respect to isotactic diads *mm*. NMR spectra were recorded for samples dissolved in two different deuterated solvents: D<sub>2</sub>O and dmsO-d<sub>6</sub>. Data are shown in the Appendix A.3. The results of NMR analysis are reported in Table 2.3. [REDACTED]

[REDACTED]

[REDACTED]

[REDACTED]

[REDACTED]

[REDACTED]







---

### 2.1.2

### 2.1.3 Film conditioning at controlled relative humidity

To test the effect of the storage at different relative humidity (RH) values on film samples, the films were equilibrated at room temperature in a closed desiccator using saturated salt solutions at RH of 50%, 66%, 70%, 79%. To obtain a dry ambient (RH  $\approx$  0%) silica gel was used while a 100%RH ambient was ensured by pure water in the desiccator. The consequent absorption/desorption of water was estimated by weighing the sample before and after the treatment by means of an analytical balance and via-thermogravimetry, obtaining comparable results. Measures were performed in triplicate, to check for the reproducibility of our results. The salts used to obtain specific RH value were chosen consulting the work of Greenspan [1]. However, to take into account possible variations of the environment, the value of RH, as well as the temperature, was measured during each experiment by a probe. In the Table A.3 of the Appendix, the list of the adopted salt solution is reported.

## 2.2 Methods

### 2.2.1 Wide Angle X-ray Scattering (WAXS)

#### Experimental Setup

Wide-angle X-ray Scattering profiles were collected at room temperature, with a multipurpose Empyrean diffractometer by PANalytical, using Ni filtered CuK $\alpha$  radiation ( $\lambda=1.5418\text{\AA}$ ) and scans at 0.005 deg ( $2\theta$ )/s in the  $2\theta$  range 5-60°. For hydrated and/or dry samples, to prevent the sorption/desorption of water due to the external environment, the recording of the diffraction data was performed using a home-made brass sample holder hermetically closed in a special brass chamber covered with a Kapton film. The sample holder was equilibrated at selected relative humidity to ensure the stability of the sample.

#### Working Principle

Wide Angle X-ray Scattering (WAXS) experiments allow obtaining information about the crystallinity in PVA samples.

A monochromatic X-ray beam is scattered by crystallographic planes within the crystalline structure, at a specific diffraction angle  $\theta$ . The relation between this diffraction angle and the regular spacing of the crystal planes  $hkl$   $d_{hkl}$  (in short  $d$ ) is given by Bragg's equation:

$$\lambda = 2d \cdot \sin\theta.$$

where  $hkl$  are the Miller indices of the planes.

The angle of the incident beam to the crystallographic plane is  $\theta$ , and the total diffraction angle between the incident and the diffracted beam is  $2\theta$ . Therefore, wide angle X-ray scattering (WAXS) patterns are plotted as the intensity versus  $2\theta$ .

A crystal structure consists of unit-cells, which are the smallest repeating units in the regular crystalline structure. The unit-cell dimensions are described by  $a$ ,  $b$  and  $c$  and their opponent angles  $\alpha$ ,  $\beta$  and  $\gamma$ . Within the crystal structure repeating crystallographic planes with a distance  $d$  are present. The crystallographic planes with miller indices  $(hkl)$  correspond to  $hkl$  reflections, and their spacing  $d$  is dependent on the unit-cell structure.

### **2.2.2 X-ray fiber diffraction**

Fiber diffraction patterns of PVA commercial films stretched at different uniaxial elongation were recorded using Ni filtered  $\text{CuK}\alpha$  radiation ( $\lambda=1.5418\text{\AA}$ ) by BAS-MS "Imaging Plate" (FUJIFILM) in a cylindrical camera (with radius  $R = 57.29$  mm). The images were recorded on the plate and elaborated by a digital reader Perkin Elmer Cyclone Plus (storage phosphor system).

### **2.2.3 Small Angle X-ray Scattering (SAXS)**

#### **Experimental Setup**

Small angle X-ray scattering (SAXS) data were obtained using a Kratky compact camera SAXSess (Anton Paar, Graz, Austria) in the slit collimation configuration with  $\text{CuK}\alpha$  radiation. The scattered radiation was recorded on a BAS-MS imaging plate (FUJIFILM) and processed with a digital imaging reader Perkin Elmer Cyclone Plus. The setup allowed collecting values of the scattering vector,  $q = 4\pi\sin\theta/\lambda$ , comprised between 0.08 and 24  $\text{nm}^{-1}$ . The background is measured recording the SAXS profile of the empty sample holder and is subtracted from the scattering of the sample. Then, the desmeared intensity was obtained by deconvolution of the experimental (slit smeared) data with the

intensity curve of the primary-beam in the infinite length approximation using the software SAXSquant 2.0.

### SAXS data analysis

In the assumption that SAXS intensity probes heterogeneities arising from a simple two phase structure at nanometer length scale, the SAXS desmeared data  $I(q)$ , after subtraction of the residual background intensity (approximated as a constant  $I_{back}$ ) has been extrapolated to high  $q$  values with the Porod law [7]:

$$I(q) = Kq^{-4} \quad \text{eq.2.1}$$

More precisely, in the hypothesis that no diffuse boundary between crystalline and amorphous layers occurs, the intensity  $I(q) = I_{obs}(q) - I_{back}$  in the high  $q$  region ( $q > 1.2 \text{ nm}^{-1}$ ) may be assumed to scale as (eq. 2.2):

$$\lim_{q \rightarrow \infty} [I_{obs}(q) - I_{back}] = K_p q^{-4} \quad \text{eq. 2.2}$$

$K_p$  is a quantity proportional to the Porod constant through a factor  $K$  due the fact that our intensity is in relative units. In this procedure the value of  $K_p$  has been found by selecting the value of background intensity  $I_{back}$  that maximizes the length of Porods's region [7].

The SAXS desmeared data  $I(q)$  have been extrapolated to  $q = 0$  using the Debye–Bueche equation [8]:

$$I_{obs}(q) - I_{back} = \frac{B}{(1 + C^2 q^2)^2} \quad \text{eq. 2.3}$$

where  $B$  and  $C$  are interpolation parameters.

The total scattered intensity  $I(q)$  has been transformed into one-dimensional intensity by multiplication for the Lorentz factor equal to  $4\pi(2\sin\theta/\lambda)^2 = q^2/\pi$  [7]. The average values of the lamellar long period  $L^*$  can be evaluated from the position  $q$  of the peak maxima ( $q^*$ ) in the Lorentz corrected SAXS intensities.

---

## Methods of SAXS data interpretation: Correlation Function (CF) and Interface Distribution Function

The following section will provide a short overview on two methods adopted for analysis of semicrystalline polymers, based on the calculation of the self-correlation function of electron density fluctuations (CF) and interface distribution function IDF. Besides, a short background of basic mathematical formalism, used to describe the intensity measured in a SAXS experiment is below reported, as described in the ref [9].

In the classical SAXS experiment, a sample is irradiated by an incident X-ray beam with wavelength  $\lambda$  and flux  $J_0$ . The scattered beam having flux  $J$  is detected as a function of the scattering angle  $2\theta$  at a certain distance from the sample. More in details, an incident plane wave with flux  $J_0$  is scattered by the electrons in the sample. The scattered spherical waves interfere with each other, resulting in an angle-dependent flux  $J$  of scattered radiation. The flux  $J_0$  of the incident plane wave corresponds to the energy transmitted per unit area and per unit time and the flux  $J$  of the scattered radiation to the energy transmitted per unit solid angle per unit time. The differential scattering cross section or scattered intensity is defined as the ratio between the flux  $J$  of the scattered beam and the flux  $J_0$  of the incident beam:

$$I(\vec{s}) = \frac{d\sigma}{d\Omega} = \frac{J}{J_0} \quad \text{eq. 2.4}$$

where  $(\vec{s})$  is the scattering vector, corresponding to the difference between the wave vector  $(\vec{k})$  associated to the scattered beam at an angle  $2\theta$  and the wave vector  $(\vec{k}_0)$  associated to the incident beam. The scattering vector and its absolute value are, hereby, reported:

$$\vec{s} = \frac{1}{2\pi} (\vec{k} - \vec{k}_0) \quad \text{eq. 2.5}$$

$$|\vec{s}| = \frac{2}{\lambda} \sin\vartheta \quad \text{eq. 2.6}$$

In alternative to  $s$ ,  $q = 2\pi s$  is often found in the SAXS formalism. The flux  $J$  of the scattered radiation is the square of the amplitude  $A$  of the scattered wave field.

$$J(\vec{s}) = |A(\vec{s})|^2 = A(\vec{s}) \times A(\vec{s})^* \quad \text{eq. 2.7}$$

$A(\vec{s})$  can be calculated as the sum of the amplitudes of the scattered waves originating from  $N$  scattering centers in the sample.

$$A(\vec{s}) = A_0 b_e \sum_{j=1}^N e^{-i2\pi\vec{s}\cdot\vec{r}_j} \quad \text{eq. 2.8}$$

where  $A_0$  is the amplitude of the incident beam and  $b_e = r_e[(1+\cos^2 2\theta)/2]^{1/2}$  is the scattering length of an electron with  $r_e$  the radius of an electron  $r_e = 2.818 \times 10^{-15}$  m and  $p = (1+\cos^2 2\theta)/2$  is the polarization factor, which is approximately 1 for small angles ( $2\theta \leq 8^\circ$ ), and therefore  $b_e \approx r_e$ .

At these angle values, a continuous electron density  $\rho(\vec{r})$  is used to describe the structure of the sample instead of single scattering centers. Hence, the sum in eq. 2.8 can be replaced by the integral over the scattering volume (irradiated sample):

$$A(\vec{s}) = A_0 b_e \int_V \rho(\vec{s}) e^{-i2\pi\vec{s}\cdot\vec{r}} d\vec{r} \quad \text{eq. 2.9}$$

Mathematically, the amplitude is proportional to the Fourier transform of the electron density  $\rho(\vec{r})$ .

In an experiment, a time-averaged intensity  $I(\vec{s})$  is measured, which in an equilibrium system is equivalent to the ensemble average:

$$I(\vec{s}) = \frac{J(\vec{s})}{J_0} = \left\langle \frac{|A(\vec{s})|^2}{|A_0|^2} \right\rangle = \left\langle |b_e \int_V \rho(\vec{s}) e^{-i2\pi\vec{s}\cdot\vec{r}} d\vec{r}|^2 \right\rangle \quad \text{eq. 2.10}$$

If  $g(\vec{r})$  is the three dimensional electron density correlation function:

$$g(\vec{r}) = \langle \rho(\vec{r}')\rho(\vec{r}' + \vec{r}) \rangle_{\vec{r}'} = \frac{1}{V} \int_V \rho(\vec{r}')\rho(\vec{r}' + \vec{r}) d\vec{r}' \quad \text{eq. 2.11}$$

Then  $I(\vec{s})$  can be rewritten as:

$$I(\vec{s}) = b_e^2 V \int_V g(\vec{r}) e^{-i2\pi\vec{s}\cdot\vec{r}} d\vec{r} \quad \text{eq. 2.12}$$

meaning that the intensity is proportional to the Fourier transform of the three-dimensional electron density correlation function  $g(\vec{r})$ .

Since, in SAXS experiments, the fluctuations of the electron density are more significant than the electron density itself,  $\rho(\vec{r})$  can be replaced by the deviation from the average electron density  $\delta\rho(\vec{r}) = \rho(\vec{r}) - \rho$ :

$$g(\vec{r}) = \langle \delta\rho(\vec{r}')\delta\rho(\vec{r}' + \vec{r}) \rangle_{\vec{r}'} + \langle \rho^2 \rangle \quad \text{eq. 2.13}$$

Lastly, the absolute intensity  $I_{abs}(\vec{s})$  is the intensity normalized to the scattering of a single electron and to the irradiated volume.

$$I_{abs}(\vec{s}) = \frac{1}{b_e^2 V} \frac{d\sigma}{d\Omega}(\vec{s}) = \int_V g(\vec{s}) e^{-i2\pi\vec{s}\cdot\vec{r}} d\vec{r} \quad \text{eq. 2.14}$$

It describes the scattering power of a material per volume in units of [e.u./nm<sup>3</sup>].

In first approximation, the morphology of semicrystalline polymer is well described by a two-phase system consisting in crystalline and amorphous phases, characterized by different electron densities, with sharp boundaries between them. This model structure produces a peak in the scattering intensity at a scattering vector  $s_p$  from which the average long period  $L = 1/s_p$  can be determined.

Assuming that the lateral dimensions of the lamellar stacks in the sample are larger than the interlamellar distance,  $L$ , only the electron density distribution along the normal of the lamellar stacks ( $z$ -direction) changes within the relevant length scale of a SAXS experiment (Figure 2.3). Therefore,  $g(\vec{r})$  is well described by a one-dimensional correlation function  $K(z)$ :

$$K(z) = \langle \delta\rho(z')\delta\rho(z' + z) \rangle_{z'} \quad \text{eq. 2.15}$$

Substituting  $K(z)$  into eq. 2.15:

$$I_{abs}(\vec{s}) = \int_{x,y,z} K(z) e^{-i2\pi\vec{s}\cdot\vec{r}} dx dy dz \quad \text{eq. 2.16}$$

After integration over  $x$  and  $y$  with  $\delta(t) = \frac{1}{2\pi} \int_{-\infty}^{\infty} e^{-i\omega t} d\omega$ :

$$I_{abs}(\vec{s}) = \delta(s_x)\delta(s_y) \int_{-\infty}^{\infty} K(z) e^{-i2\pi s_z z} dz \quad \text{eq. 2.17}$$

As the lamellar stacks are isotropically distributed inside the sample, the intensity in  $\pm s_z$  direction is distributed over the surface of a sphere with radius  $s_z$ :

$$I_{abs}(\vec{s}) = \frac{2}{4\pi s_z^2} \int_{-\infty}^{\infty} K(z) e^{-i2\pi s_z z} dz \quad \text{eq. 2.18}$$

The reverse Fourier transform gives

$$K(z) = \int_{-\infty}^{\infty} 2\pi s^2 I_{abs}(s) e^{-i2\pi s_z z} ds \quad \text{eq. 2.19}$$

Since  $K(z)$  and  $I_{abs}(s)$  are both even function ( $f(x) = f(-x)$ ), the Fourier transform becomes a cosine transform:

$$K(z) = 2 \int_0^{\infty} 2\pi s^2 I_{abs}(s) \cos(2\pi s z) ds \quad \text{eq. 2.20}$$

which means that the one-dimensional correlation function  $K(z)$  can be calculated directly from  $I(s)$ . The correlation function  $K(z)$  for an ideal lamellar stacks is shown in Figure 2.4-A. The “self-correlation triangle” centered at the origin, reflects the electron density correlation within a lamella. For a two-phase system, the maximum  $Q$  at  $z = 0$  is

$$Q = K(0) = \delta\rho^2 = \Delta\rho^2 \phi_a \phi_c \quad \text{eq. 2.21}$$



It depends only on the volume fractions of the two phases  $\phi_c$  and  $\phi_a$  and the electron density difference  $\Delta\rho = \rho_c - \rho_a$  that is  $Q$  does not depend on the detailed structure. Therefore, it is called *invariant*.

From the maximum at the origin,  $K(z)$  decreases linearly to a minimum value, namely, the baseline  $B$ , with the value

$$-B = -\phi_c^2 \Delta\rho^2 = \frac{\phi_c}{1 - \phi_c} \quad \text{eq. 2.22}$$

If the crystallinity is smaller than 50% ( $\phi_c \leq 0.5$ ), this minimum position corresponds to the crystalline thickness  $d_c$ . Otherwise, it corresponds to the amorphous thickness  $d_a$  and  $\phi_c$  has to be replaced by  $\phi_a = (1 - \phi_c)$ , in accordance with Babinet's principle.

The slope of  $K(z)$  at the origin is

$$\frac{dK}{dz} = -\frac{O_{ac}}{2} \Delta\rho^2 = \frac{\Delta\rho^2}{L} \quad \text{eq. 2.23}$$

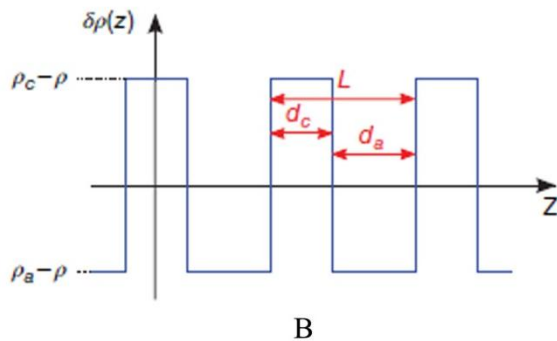
With  $O_{ac}$  as the specific inner surface per unit volume of the interfaces between crystalline and amorphous regions.

$$O_{ac} = \frac{2}{L} = \frac{2\phi_c}{d_c} \quad \text{eq. 2.24}$$

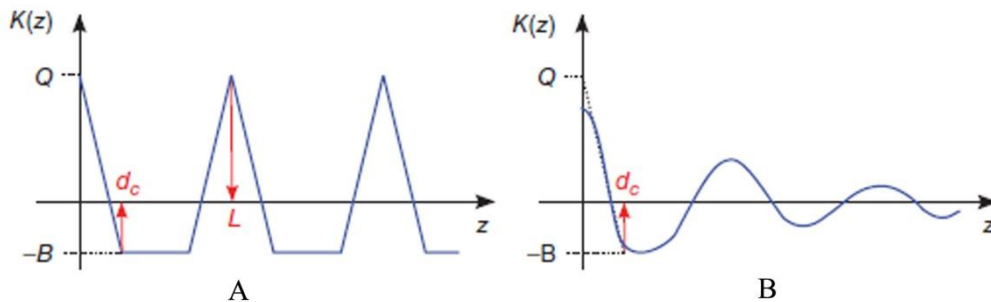
The second maximum in  $K(z)$  is located at the long period  $L$ . The crystallinity and the square of the electron density then follow by:

$$\phi_c = \frac{d_c}{L} = \frac{B}{B + Q} \quad \text{eq. 2.25}$$

$$\Delta\rho^2 = \frac{Q}{\phi_c(1 - \phi_c)} = \frac{(B + Q)^2}{B} \quad \text{eq. 2.26}$$



**Figure 2.3:** Electron density difference along the  $z$ -direction of the ideal lamellar structure of a semicrystalline polymer consisting of crystalline lamellae with thickness  $d_c$  and amorphous regions with thickness  $d_a$  alternating along the  $z$ -direction with periodicity  $L=d_c+d_a$ . From [9].

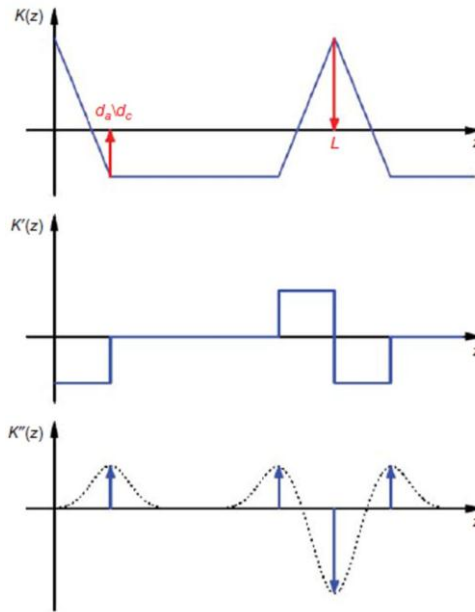


**Figure 2.4:** Correlation function for an ideal lamellar stack (A) and effect of deviations from ideality (B). From [9].

In a real system, deviations from the ideal structure exist, such as variations of the lamellar and crystalline thicknesses or diffuse interphases. The effect of deviation from ideality is drawn in Figure 2.4-B. Around the origin,  $K(z)$  is flattened. The first minimum does not necessarily reach the value of the baseline anymore. In addition, higher order maxima of  $K(z)$  are damped due to the thickness variations of the crystalline and amorphous phase, leading to an overestimated long period [10].

An alternative way of analyzing SAXS data of a lamellar two-phase system is evaluating the interface distribution function  $K''(z)$  (IDF). The method has been described by Ruland [11] For an ideal lamellar two-phase system, the second

derivative of the one-dimensional correlation function  $K''(z)$  has only contributions ( $\delta$ -functions) at positions that correspond to the distance of any two interphases, with the first three giving the structure parameters  $d_a$ ,  $d_c$ , and  $L$ . Figure 2.5 shows the correlation function and the first and second derivative  $K'(z)$  and  $K''(z)$ . Deviations from an ideal lamellar structure, for example, varying amorphous and crystalline thicknesses, lead to a broadening of the  $\delta$ -peaks (Figure 2.5).



**Figure 2.5: Correlation function  $K(z)$  for an ideal lamellar stack and the first and second derivatives  $K'(z)$  and  $K''(z)$ . Deviations from the ideal lamellar structure lead to a broadening (dotted line) of the  $\delta$ -Peaks (arrows). From [9].**

$K''(z)$  can be calculated directly from  $I_{abs}(s)$  using the common expression for the Fourier transform of derivatives [12]:

$$\mathcal{F}[K''(z)] = (i2\pi s)^2 \mathcal{F}[K(z)] \quad \text{eq. 2.27}$$

$$K''(z) = -8\pi^3 \int_{-\infty}^{\infty} s^4 I_{abs}(s) e^{i2\pi s z} ds \quad \text{eq. 2.28}$$

## Chapter 2

---

The triangular shape of  $K(z)$  around the origin leads to a  $\delta$ -function for  $K''(z)$  at  $z = 0$ , which gives a constant contribution in reciprocal space for  $s \rightarrow \infty$ , which has to be subtracted [13]:

$$\lim_{s \rightarrow \infty} I_{abs}(s)s^4 = \text{const} = P \quad \text{eq. 2.29}$$

This means that for  $s \rightarrow \infty$  it is assumed that the experimental SAXS intensity responds to the Porod law [14]:

$$I_{abs}(s) = Ps^{-4} \quad \text{eq. 2.30}$$

The Porod parameter  $P$  is related to the specific inner surface  $O_{ac}$  and the electron density difference  $\Delta\rho$ :

$$P = \frac{O_{ac}\Delta\rho^2}{8\pi^3} \quad \text{eq. 2.31}$$

A decrease of  $I(s) \propto s^{-4}$  is characteristic for a two-phase system with sharp boundaries [14]. After subtracting the contribution at  $z = 0$ , eq. 2.32 yields:

$$K''(z) = 8\pi^3 \int_{-\infty}^{\infty} [\lim_{s \rightarrow \infty} I_{abs}(s)s^4 - s^4 I_{abs}(s)] e^{i2\pi sz} ds \quad \text{eq. 2.33}$$

The inverse Fourier transform:

$$\left[ \lim_{s \rightarrow \infty} I_{abs}(s)s^4 - s^4 I_{abs}(s) \right] = \int_{-\infty}^{\infty} \frac{K''(z)}{8\pi^3} e^{i2\pi sz} dz \quad \text{eq. 2.34}$$

Since  $K''(z)$  is an even function the latter equation is equivalent to

$$\left[ \lim_{s \rightarrow \infty} I_{abs}(s)s^4 - s^4 I_{abs}(s) \right] = 2 \int_0^{\infty} \frac{K''(z)}{8\pi^3} \cos(2\pi z) dz \quad \text{eq. 2.35}$$

With  $s^4 I_{abs}(s)$  being an even function, the eq. 2.33 becomes:

$$K''(z) = 16\pi^3 \int_0^{\infty} [\lim_{s \rightarrow \infty} I_{abs}(s)s^4 - s^4 I_{abs}(s)] \cos(2\pi sz) ds \quad \text{eq. 2.36}$$

For an ideal system,  $K''(z=0)$  as defined in eq. 2.34 is zero, corresponding to the fact that there are no interfaces with zero distance, as they would occur, for example, at the edges of lamellar crystals. For laterally extended lamellae, this contribution is negligible also in a real lamellar system [9]. The scattering

intensity  $I_{abs}(s)$  is measured in absolute units as defined in eq. 2.14. In addition to scattering, absorption takes place in the sample, following the Lambert–Beer law [7] as it does for visible light. For SAXS, the transmitted and the scattered beams are attenuated by the same amount. The transmission measured for the primary beam can therefore be used to correct the scattering signal  $I_{exp}(s)$  for absorption effects. The absorption factor  $A$  is the ratio of the primary beam intensity with and without the sample.

$$A = \frac{J_0 (Sample)}{J_0 (Background)} \quad \text{eq. 2.37}$$

$$I_{exp,abs}(s) = A^{-1}I_{exp}(s) \quad \text{eq. 2.38}$$

Absorption also needs to be taken into account when subtracting the background  $I_{exp,BG}(s)$ , caused, for example by the empty sample holder. This is the last step by which the experimental data have to be corrected before calculating the correlation function or the IDF.

$$I_{abs}(s) = I_{exp,abs}(s) - I_{exp,BG}(s) \quad \text{eq. 2.39}$$

## 2.2.4 Differential Scanning Calorimetry (DSC)

Calorimetrical measurements were performed with a differential scanning calorimeter (DSC) Mettler Toledo DSC-822 calibrated against an indium standard ( $T_m=156.6^\circ\text{C}$ ) reaching the minimum temperature of  $-70^\circ\text{C}$  while DSC Mettler Toledo 001 was used to reach temperatures below  $-100^\circ\text{C}$  using liquid  $\text{N}_2$ . In all experiments, small amounts of the sample were analyzed at a heating rate of  $10^\circ\text{C}/\text{min}$  in a flowing nitrogen atmosphere.

The analysis on samples at variable water content, were performed in hermetically sealed aluminum pans in order to prevent water loss.

For all the measurements, the reference was an empty pan.

### 2.2.5 Thermogravimetric analysis (TGA)

Thermogravimetric analysis (TGA) measurements were made using a TGA 4000 by Perkin Elmer. Samples of approximately 5 mg were placed in an alumina crucible and heated from 30 to 900 °C, with a heating rate of 10 °C/min under nitrogen or air flow.

### 2.2.6 Mechanical tests

Mechanical tests were performed at room temperature on films obtained by solution casting with a Zwick Roell mechanical tester (*Zwicky* model), following the *Standard test method for tensile properties of thin plastic sheeting* - ASTM D882-83. Rectangular specimens 5 cm long, 5 mm wide were stretched up to the break. In the mechanical tests, the ratio between the drawing rate and the initial length was fixed equal to 0.1 mm/(mm×min) for the measurement of Young's modulus and 10 mm/(mm×min) for the measurement of stress-strain curves and the determination of the other mechanical properties (stress and strain at break and tension set). The reported values of the mechanical properties are averaged over at least seven independent experiments.

All the measurements were carried out at controlled relative humidity and temperature in the ambient chamber of which the dynamometer is provided.

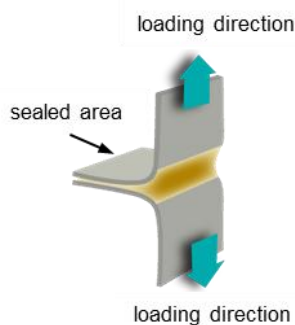
### 2.2.7 T-Peel tests

T-peel tests were performed by means of an Instron mechanical tester, adapting the *Standard Test Method for Peel Resistance of Adhesives (T-Peel Test)* – ASTM D1876-01 [REDACTED]

[REDACTED] The T-peel test is a type of tensile test performed upon two flexible substrates that have been bonded together and

placed into peel test grips such that one substrate sticks up and the other sticks down while the bonded area sticks out horizontally so that the entire setup forms a “T” shape (Figure 2.6).

Rectangular specimens 25 mm wide and 50 mm long, and sealed over 24 mm of their length, were prepared and stretched up complete separation of the sealed area or break of the specimen, at rate of 24 mm/min. The resistance of the welding is expressed as Peel strength (N/m). The broken specimens were considered negative tests, and the reported data (see Chapter 6) are relative only to trial tests terminated by the complete separation of the specimens in the welding zones. As the operative conditions selected for the welding (*vide infra*) were selected to prevent rupture, the percentage of specimens experiencing full separation in the welded regions in the peel test was  $\approx 80\text{-}90\%$ .



**Figure 2.6: Typical specimen used for T-Peel test.**

## 2.2.8 Dynamic Vapor Sorption (DVS)

A Dynamic Vapor Sorption (DVS) device (SPS32, ProUmid) was employed to perform water sorption experiments at controlled water vapor activity. The DVS analyzer regulates the activity inside the chamber whereas an internal microbalance monitors the weight change of the samples. The used device is equipped by a multisampling

system, composed by a carousel of 11 pans/sample holders, allowing testing more samples at the same time.

Each experiment is composed by two steps: an absorption step from 10% to 80% water vapor activity, followed by a desorption step from 80 to 10% water vapor activity. Activity increments of 10% were set: when the sample reaches the equilibrium, corresponding to weight stabilization, an instantaneous raise of water vapor activity of 10% occurs.

The reported data are an average over three tests, carried out on independent specimens, for each PVA film.

### **2.2.9 Rheometry**

#### **Experimental setup**

The rheological properties of the PVA solutions were measured by a stress-controlled rheometer (Anton Paar-MCR-302). Cone-plate geometry was adopted, with a cone having diameter of 49.9 mm, an angle of  $1.982^\circ$  and a truncation of 206  $\mu\text{m}$ . The rheometer was equipped with a Peltier system to control the temperature. Before each test, the solutions were held at  $20^\circ\text{C}$  temperature for 3 min to eliminate their thermal and shear histories. Frequency sweep tests were carried out at  $20^\circ\text{C}$  in an oscillatory mode over the range from 0.1 to 600 rad/s, within the linear viscoelastic regime (LVE). Before each frequency sweep test, amplitude sweep experiments were performed at 1 Hz over the strain range 0.01-100% to determine the LVE region, in which  $G'$  and  $G''$  are practically constant and independent of the strain amplitude. Viscosity measurement have been carried out at  $20^\circ\text{C}$ .

#### **Sample preparation**

PVA samples were dissolved in deionized water at  $85^\circ\text{C}$ , under magnetic stirring, using a reflux condenser to avoid solvent evaporation. The dissolution





[REDACTED]

[REDACTED]

[REDACTED]

[REDACTED]

[REDACTED]

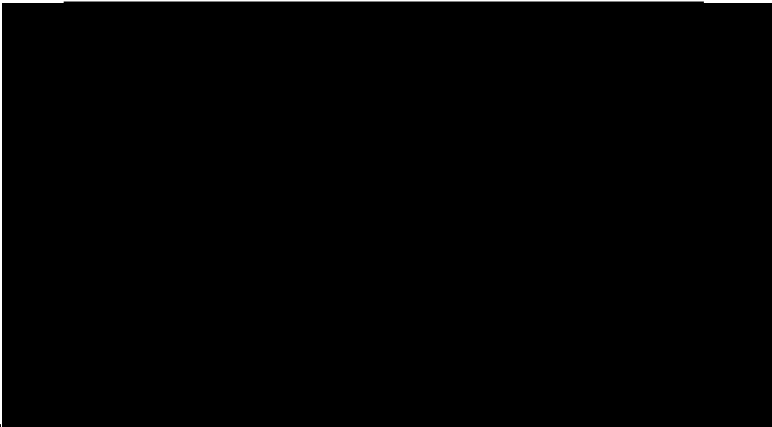
[REDACTED]

[REDACTED]

[REDACTED]

[REDACTED]

[REDACTED]



[REDACTED]

[REDACTED]

[REDACTED]

[REDACTED]

[REDACTED]

[REDACTED]

[REDACTED]

[REDACTED]

[REDACTED]





[REDACTED]

### References

- [1] L. Greenspan, "Humidity fixed points of binary saturated aqueous solutions," *J. Res. Natl. Bur. Stand. Sect. A Phys. Chem.*, vol. 81, no. 1, pp. 89–96, 1977.
- [2] K. Katsuraya, K. Hatanaka, K. Matsuzaki, and S. Amiya, "Assignment of finely resolved  $^{13}\text{C}$  NMR spectra of poly (vinyl alcohol)," *Polymer*, vol. 42, pp. 9855–9858, 2001.
- [3] T. Moritani, I. Kuruma, K. Shibatani, K. Company, and R. April, "Tacticity of Poly(vinylalcohol) Studied by Nuclear Magnetic Resonance of hydroxyl protons," *Macromolecules*, vol. 5, no. 5, pp. 577–580, 1972.
- [4] T. K. Wu and D. W. Ovenall, "Proton and Carbon-13 Nuclear Magnetic Resonance Studies of Poly(vinyl alcohol)," *Macromolecules*, vol. 6, no. 4, pp. 582–584, 1973.
- [5] S. Amiya, S. Tsuchiya, R. Qian, and A. Nakajima, "The study of microstructures of poly(vinyl alcohol) by NMR," *Pure Appl. Chem.*, vol. 62, no. 11, pp. 2139–2146, 1990.
- [6] T. Moritani and Y. Fujiwara, " $^{13}\text{C}$ - and  $^1\text{H}$ -NMR Investigations of Sequence Distribution in Vinyl Alcohol-Vinyl Acetate Copolymers," *Macromolecules*, vol. 10, no. 3, pp. 532–535, 1977.
- [7] R. J. Roe, *Methods of X-Ray and Neutron Scattering in Polymer Science*, Oxford Uni. 2000.
- [8] P. Debye and A. M. Bueche, "Scattering by an inhomogeneous solid," *J. Appl. Phys.*, vol. 20, no. 6, pp. 518–525, 1949.
- [9] A. Seidlitz and T. Albrecht, "Small-Angle X-ray Scattering for morphological analysis of semicrystalline polymers," in *Polymer*

- Morphology: Principles, Characterization and Processing*, John Wiley., Q. Guo, Ed. New York, 2016, pp. 153–163.
- [10] C. Santa Cruz, N. Stribeck, H. G. Zachmann, and F. J. Baltá Calleja, “Novel Aspects in the Structure of Poly(ethylene terephthalate) As Revealed by Means of Small-Angle X-ray Scattering,” *Macromolecules*, vol. 24, no. 22, pp. 5980–5990, 1991.
- [11] W. Ruland, “The evaluation of the small-angle scattering of lamellar two-phase systems by means of interface distribution functions,” *Colloid Polym. Sci.*, vol. 255, no. 5, pp. 417–427, 1977.
- [12] T. Butz, *Fourier Transformation for Pedestrians*, Springer. 2006.
- [13] G. Strobl, *The Physics of Polymers: Concepts for Understanding Their Structures and Behavior*, Springer-V. Berlin Heidelberg, 2007.
- [14] G. Porod, “Die Röntgenkleinwinkelstreuung von dichtgepackten kolloiden Systemen,” *Colloid Polym Sci*, vol. 124(2), pp. 83–114, 1951.
- [15] F. C. C. MacKintosh and C. F. F. Schmidt, “Microrheology,” *Curr. Opin. Colloid Interface Sci.*, vol. 4, no. 4, pp. 300–307, 1999.
- [16] A. Mukhopadhyay and S. Granick, “Micro- and nanorheology,” *Curr. Opin. Colloid Interface Sci.*, vol. 6, no. 5–6, pp. 423–429, 2001.
- [17] T. A. Waigh, “Microrheology of complex fluids,” *Reports Prog. Phys.*, vol. 68, no. 3, pp. 685–742, 2005.
- [18] M. J. Solomon and Q. Lu, “Rheology and dynamics of particles in viscoelastic media,” *Curr. Opin. Colloid Interface Sci.*, vol. 6, pp. 430–437, 2001.





# Chapter 3

## Characterization of PVA samples

*The natural desire of good men is knowledge.*

*Leonardo da Vinci*

### 3.1 Introduction

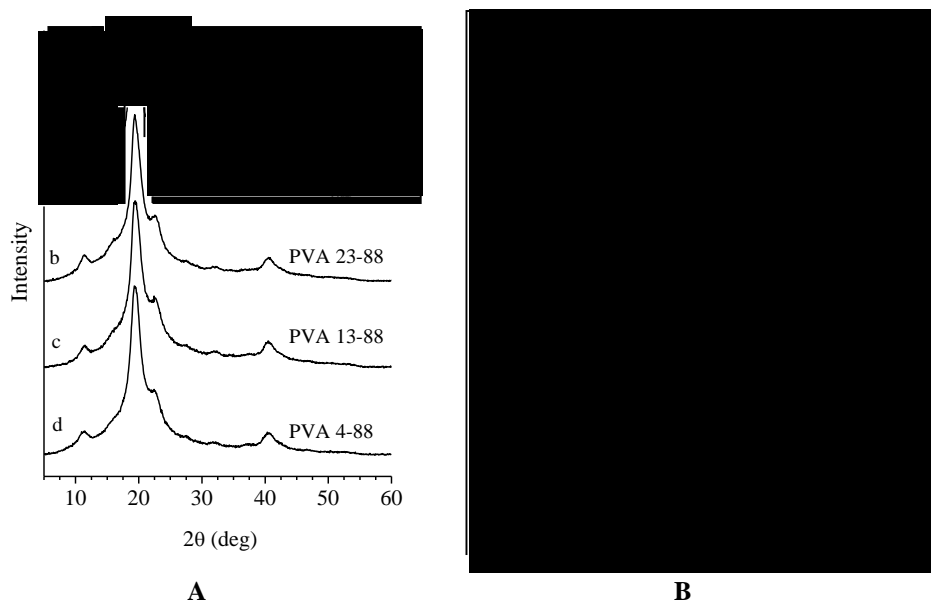
In this chapter, a characterization of PVA samples in absence of added water is reported. The main characteristics of the samples are reported in Table 2.1. The investigation techniques include X-ray analysis at wide angle (WAXD), Differential Scanning Calorimetry (DSC), Thermo-Gravimetric (TGA), Attenuance Total Reflection (ATR) (Appendix A.1), solution  $^1\text{H}$  and  $^{13}\text{C}$  NMR (Nuclear Magnetic Resonance) (Appendix A.3), and mechanical tests.

The aim of this characterization is establishing the structure and thermal properties of as received samples. In addition, the crystallization kinetics of PVA samples is also analyzed in anhydrous conditions to establish the crystallization time scale of our grades in absence of water and at high temperature.

### 3.2 Structural characterization

The X-ray powder diffraction profiles at wide angle (WAXD) of PVA samples are reported in Figure 3.1.

The diffraction profiles indicate that all samples are crystallized in the monoclinic form of PVA proposed by Bunn [1]. The diffraction profiles of Figure 3.1 are, in fact, characterized by an intense reflection at  $2\theta = 19.4^\circ$ , relative to the planes  $(10\bar{1})$  of the monoclinic form of PVA.

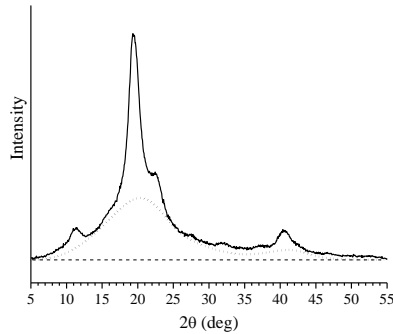


**Figure 3.1: WAXS-profiles of PVA samples: resins (A) and sharp reflections in B (curves b and c) are due to the crystalline additives.**

The degree of crystallinity ( $x_c$ ) can be estimated from the ratio of the integrated intensity of Bragg peaks associated with crystalline reflections to the total integrated area of the profiles, subtracting the profiles, after subtraction for the background, approximated by a straight line:

$$x_c = \frac{A_c}{A_t} \quad \text{eq. 3.1}$$

where  $A_c$  is the area of the crystalline fraction and  $A_t$  is the total integrated area (Figure 3.2).  $A_c$  is obtained by the subtraction of the amorphous area to the total area. This procedure is based on an oversimplification of the true nature of system, since it does not account for the differences in scattering efficiency of the crystalline and amorphous regions, assuming an additive contribution from crystalline and amorphous intensities. The so-calculated values of the degrees of crystallinity ( $x_c$ ) are reported in Table 3.1.



**Figure 3.2: WAXS profiles of PVA sample (solid curve) and of amorphous PVA (dotted curve) after subtraction of the background (dashed line). The profile of amorphous PVA is taken from [2].**

Moreover, it should be taken into account that our systems are not two-phase systems (crystalline PVA and amorphous PVA) but contain also water and other additives. Indeed, beside the solvent molecules inserted between the chains during the film formation, [REDACTED]

[REDACTED]. Resins do not contain additives but have a small content of water, trapped during the synthetic step and/or absorbed from air. To evaluate quantitatively the effective composition of the samples TGA technique was used (see section 3.3.1). [REDACTED]

[REDACTED]

All the resins have similar degree of crystallinity of  $\approx 45\%$ , [REDACTED] exhibiting a crystallinity value slightly lower than other samples ( $\approx 40\%$ ).

[REDACTED]

Table 3.1: Degree of crystallinity ( $x_c$ ) from WAXD-data calculated by eq. 3.1.

Sample	$x_c$ (%)
[REDACTED]	[REDACTED]
PVA 23-88	45
PVA 13-88	45
PVA 4-88	45
[REDACTED]	[REDACTED]
[REDACTED]	[REDACTED]
[REDACTED]	[REDACTED]
[REDACTED]	[REDACTED]

### 3.3 Films composition and thermal behavior of PVA samples

#### 3.3.1 Thermogravimetric analysis (TGA)

Thermogravimetry (TGA) allowed us to quantify the content of water trapped during synthesis or storage of PVA samples. [REDACTED]

[REDACTED] and to follow the steps of the polymer degradation.

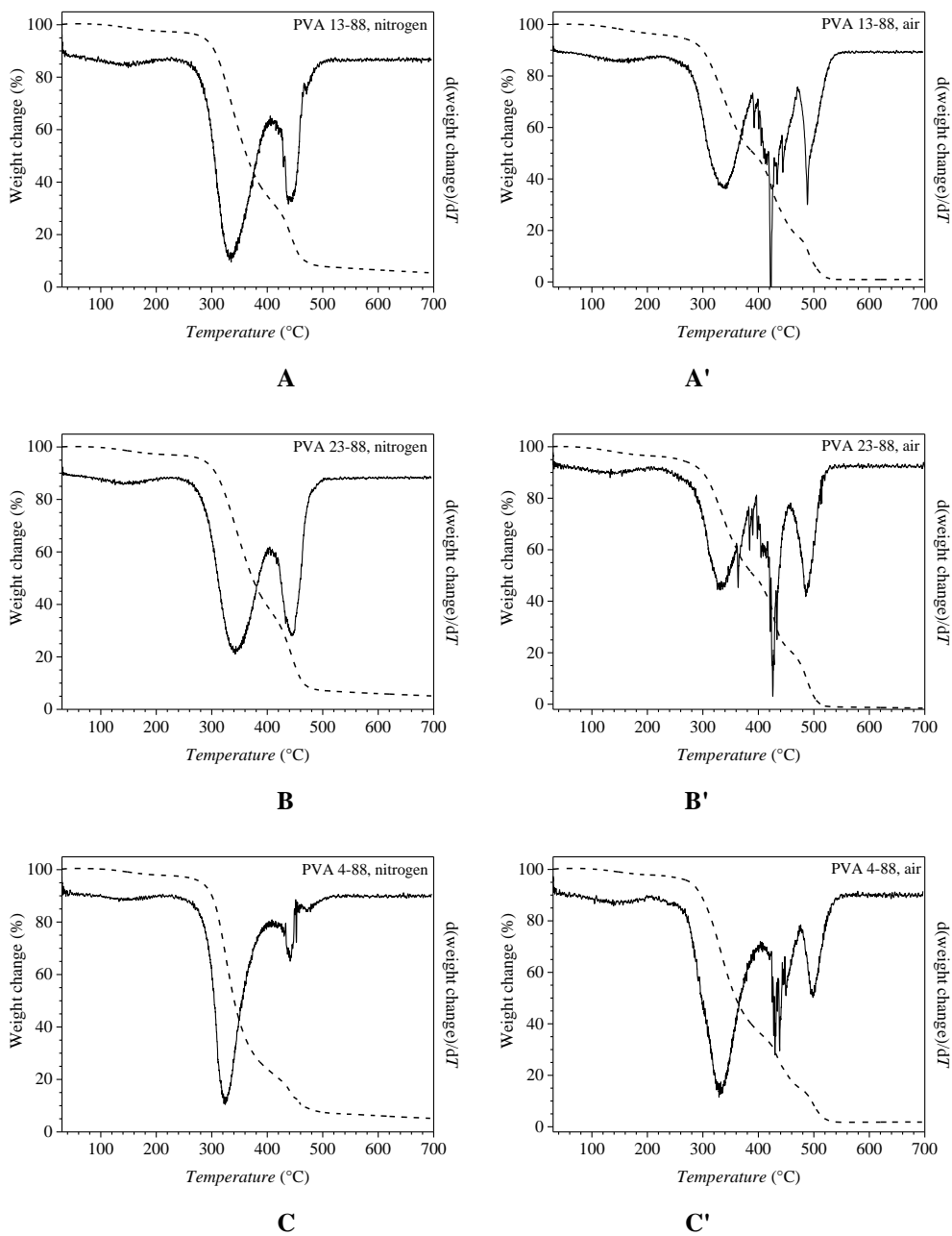
The analyses were performed both under nitrogen and air flow from 30°C until a maximum temperature of 900°C, at scan rate of 10°C/min. [REDACTED]

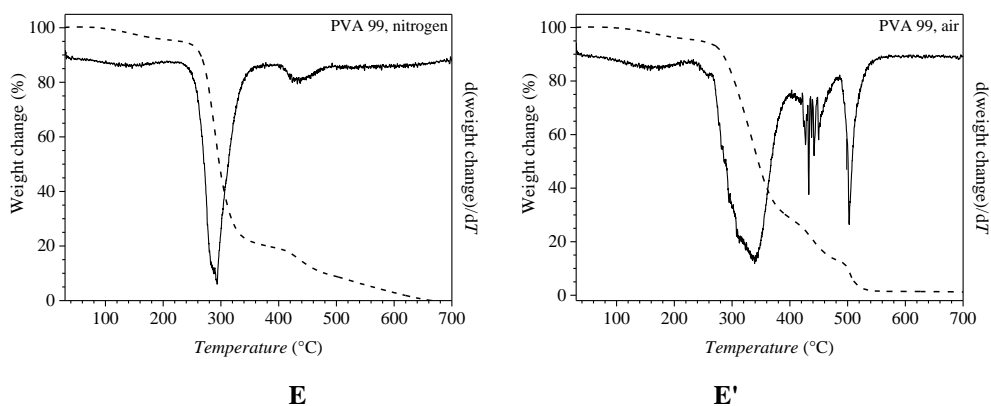


Figure 3.3 shows the TGA curves of the resins samples (left ordinate) and the correspondent derivative (right ordinate). For comparison the TGA curves

## Chapter 3

of a PVA grade commercialized by Aldrich (PVA 99) are also reported in Figure 3.3-E, E'.





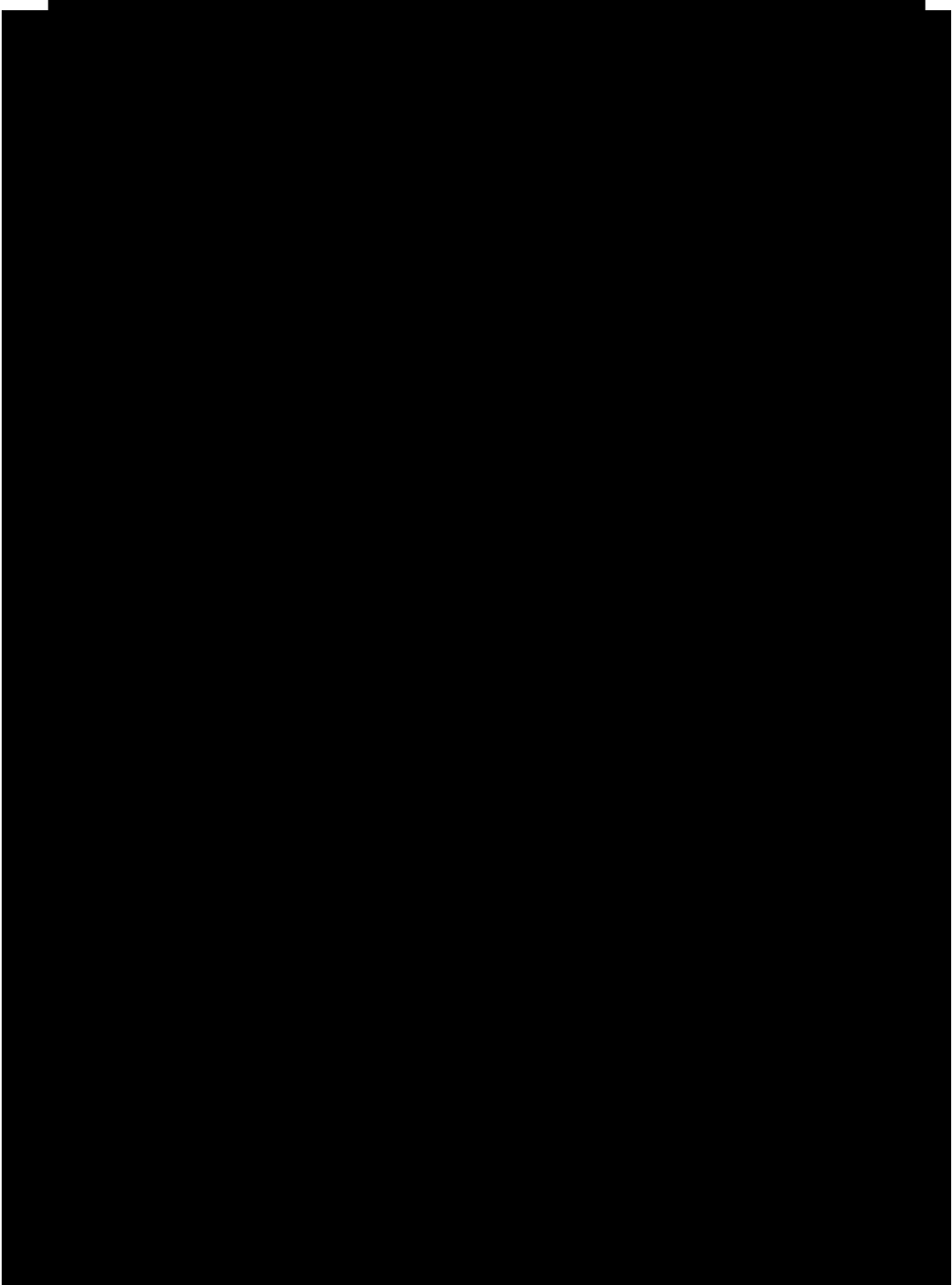
**Figure 3.3:** TGA curves (dashed lines, left axis) of PVA 23-88, PVA 13-88, PVA 4-88, [REDACTED] and PVA 99 recorded in air (A-E) and nitrogen flow (A'-E'). The corresponding derivative curves (right axis) are shown on each graph as solid line.

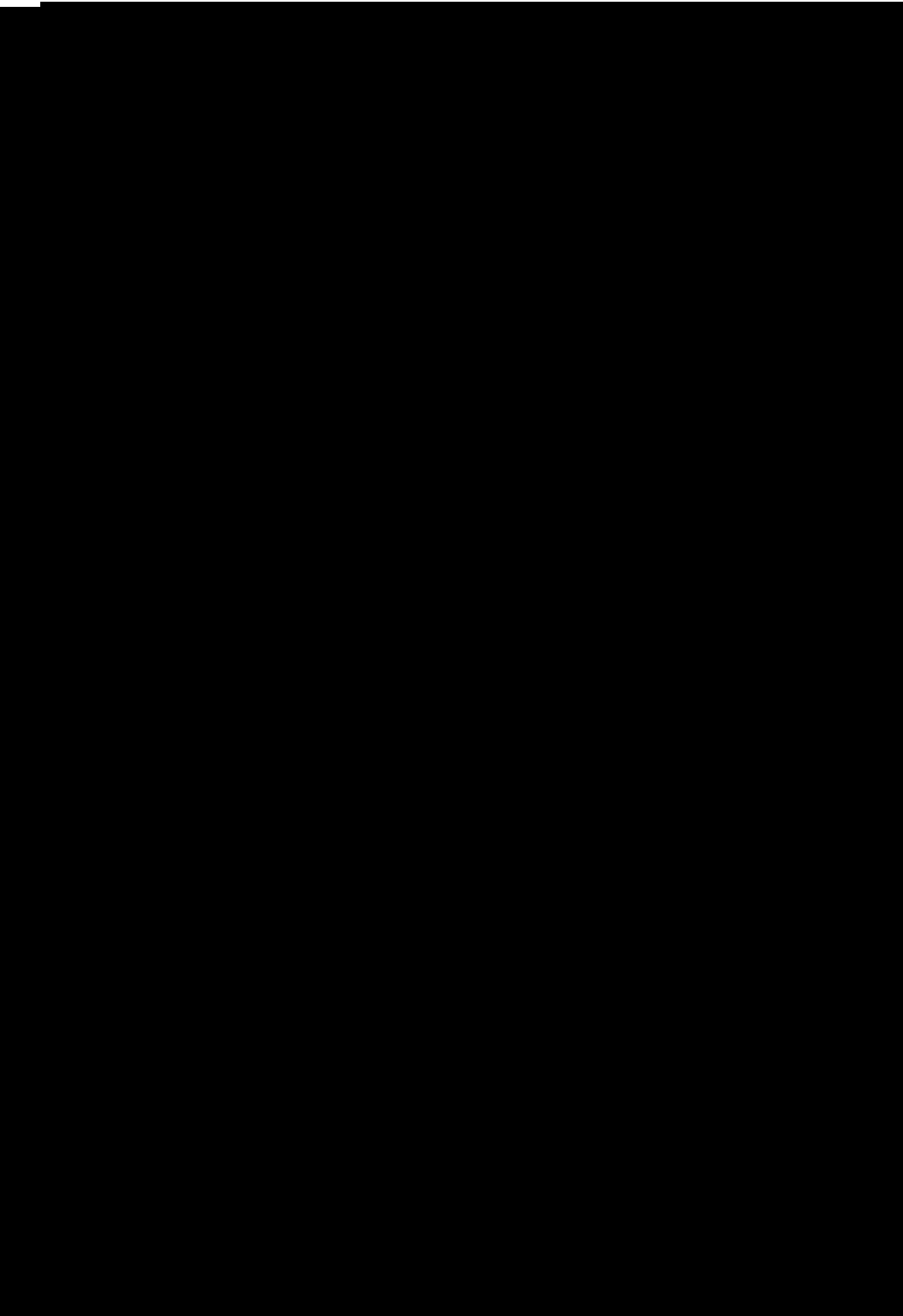
The PVA resins decompose, after the water loss, in a two-steps process in inert atmosphere ( $N_2$ ) [3]. The thermal degradation starts for all the resins at about 250°C. [REDACTED]

[REDACTED] During this step the degradation proceeds by elimination of the hydroxyl and acetate side groups chain (Figure 3.4). In the second degradation step at  $\approx 400^\circ\text{C}$  (Figure 3.3- A-E, Table 3.2)., the pyrolysis occurs producing organic volatile groups [3]–[5].







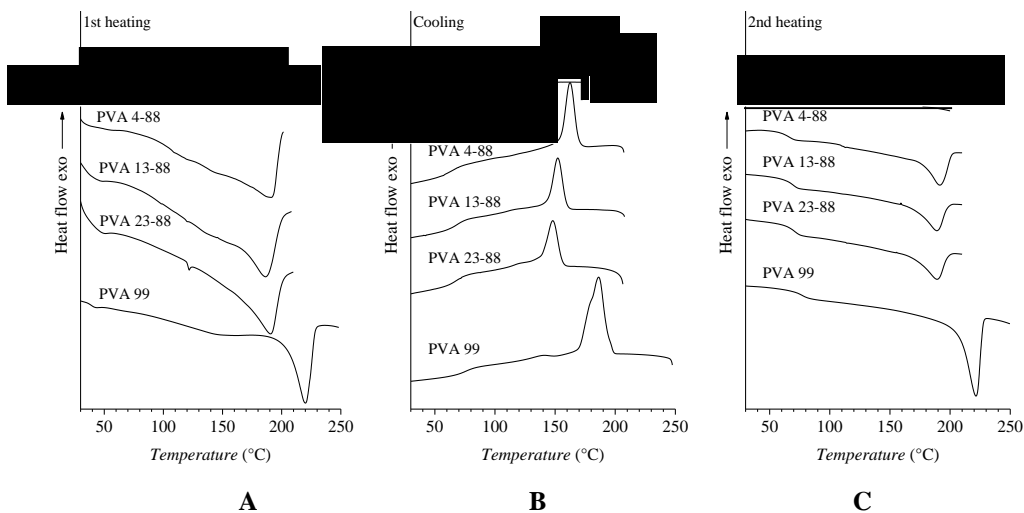


**Table 3.2: Water and additive contents, starting decomposition temperatures of the first and the second degradation steps and solid residue at 700°C. The parameters are extracted from Figure 3.3 for PVA resins samples**

Sample	Water content wt(%)	Additives content wt(%)	Decomposition temperature (°C)		Second step decomposition (°C)		Solid Residue wt(%)	
			N <sub>2</sub>	air	N <sub>2</sub>	air	N <sub>2</sub>	air
			PVA 23-88	3.3	-	255	237	405
PVA 13-88	3.1	-	257	232	408	398	5.5	-
PVA 4-88	2.6	-	240	228	410	406	5.4	-
PVA 99	4.5	-	230	236	400	413	-	-

### 3.3.2 DSC characterization

A thermal characterization was carried out for all the samples by means of DSC. The thermograms relatives to the four resins are shown in Figure 3.7. In each experiment, the samples were first heated from 25°C to 210°C, then cooled up 25°C and re-heated up 210°C at a scan rate of 10°C/min. The sample PVA-99, used as reference, was also analyzed reaching a maximum temperature in the heating step of 250°C.



**Figure 3.7:** DSC thermograms of PVA-resins recorded during the 1st heating (A), successive cooling (B) and 2nd heating (C) at scanning rate of 10°C/min.

The melting temperatures in the first and second heating,  $T_{m,1}$   $T_{m,2}$ , the crystallization temperature,  $T_c$ , and the glass transition temperatures,  $T_g$ , determined from DSC analysis are reported in Table 3.3. Compared with the reference PVA 99, melting at  $\approx 220^\circ\text{C}$ , all resins show a melting peak at  $\approx 190^\circ\text{C}$ , both in the first and second heating scan. Also the crystallization temperature of resins ( $T_c \approx 148\text{-}162^\circ\text{C}$ ) is lower than that of the reference sample ( $186^\circ\text{C}$ ).

On the other hand, all samples show a decrease of crystallization ability after the first heating scan, as indicated by the lower crystallization and melting enthalpies, measured in the second heating scan, compared to the melting enthalpy relative to the first

heating scan. This may due to the loss of water in the first heating scan, acting as a plasticizer, as indicated by the increase of glass transition temperature from  $\approx 50^\circ\text{C}$  to  $65\text{-}90^\circ\text{C}$  after the first heating scan.

**Table 3.3: Glass transition, melting and crystallization temperatures and related enthalpy value obtained from DSC curves of Figure 3.6.**

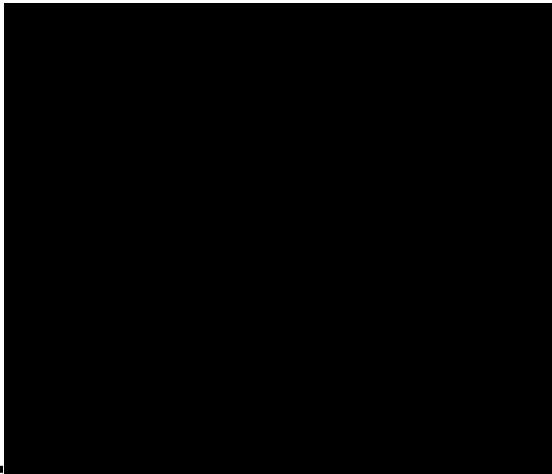
Sample	<sup>(a)</sup> $T_g^1$ ( $^\circ\text{C}$ )	<sup>(b)</sup> $T_g^2$ ( $^\circ\text{C}$ )	<sup>(c)</sup> $T_g^3$ ( $^\circ\text{C}$ )	$T_{m,1}$ ( $^\circ\text{C}$ )	<sup>(d)</sup> $\Delta H_{m,1}$ ( $\text{J/g}$ )	$T_c$ ( $^\circ\text{C}$ )	<sup>(d)</sup> $\Delta H_c$ ( $\text{J/g}$ )	$T_{m,2}$ ( $^\circ\text{C}$ )	<sup>(d)</sup> $\Delta H_{m,2}$ ( $\text{J/g}$ )
<b>PVA 4-88</b>	$\approx 50$	65	64	190	-110	162	33	191	-33
<b>PVA 13-88</b>	$\approx 50$	66	67	186	-40	152	28	189	-30
<b>PVA 23-88</b>	$\approx 50$	67	68	190	-50	148	34	189	-33
<b>PVA 99</b>	$\approx 50$	75	77	220	-150	186	67	221	-70

<sup>(a)</sup>Glass Transition,  $T_g^1$  determined in the 1st heating scan.

<sup>(b)</sup>Glass Transition,  $T_g^2$  determined in the cooling scan.

<sup>(c)</sup>Glass Transition,  $T_g^3$  determined in the 2nd heating scan.

<sup>(d)</sup> $\Delta H$  values are normalized for the mass of dry sample, determined by weighting the DSC pan before and after the scan.



[Redacted text block]

[Redacted text block]

[Redacted text block]

[Redacted text block]

[Redacted text block]

[Redacted text block]

[Redacted text block]

[Redacted text block]

[Redacted text block]

[Redacted text block]

[Redacted text block]

[Redacted text block]

[Redacted text block]

[Redacted text block]

[Redacted text block]

[Redacted text block]

[Redacted text block]

The degrees of crystallinity,  $x_c(\text{DSC})$ , of PVA resins samples and of PVA films in absence of plasticizers were determined as:

$$x_c(\text{DSC}) = \frac{\Delta H_m}{\Delta H_m^0} \times 100 = \frac{\text{PVA}_{\text{crystalline}}}{\text{PVA}_{\text{total}}} \times 100 \quad \text{eq. 3.2}$$

The eq. 3.2 is the ratio of the heat of second fusion,  $\Delta H_m$ , (normalized by the effective mass of the polymer) to the heat of fusion of a 100% crystalline PVA,

## Chapter 3

---

$\Delta H_m^0 = 138.6 \text{ J/g}$  [6]. The effective mass of the PVA sample is determined by weighting the DSC pan before and at the end of DSC scans.

Compared with the crystallinity index deduced from WAXS analysis of PVA samples not subjected to any thermal treatment, the values of degree of crystallinity obtained from DSC analysis are lower, due to the removal of water in the first heating scan acting as plasticizer, which prevents a more complete crystallization.

<b>PVA 23-88</b>	25
<b>PVA 13-88</b>	23
<b>PVA 4-88</b>	24
<b>PVA 99</b>	53



### 3.3.3 Isothermal crystallization

The crystallization kinetics of PVA resins in isothermal conditions were probed on the sole PVA resins. [REDACTED]

[REDACTED] It is worth noting that also for the other resins a limited range of temperatures could be explored because of the degradation problem.

The kinetics data were analyzed using the Avrami approach [7]–[9]. This model provides significant information about the overall crystallization, nucleation and growth process, as well as the half crystallization time (time at which half of the crystallizable materials is crystallized). Typically, the degree of undercooling and the chain length are important factors in the crystallization process of random copolymers. In our systems, also hydrogen-bonding and other hydroxyl interactions, such as the presence of water, can affect the crystallization. In the present case, the experimental settings allow a solvent-free investigation.

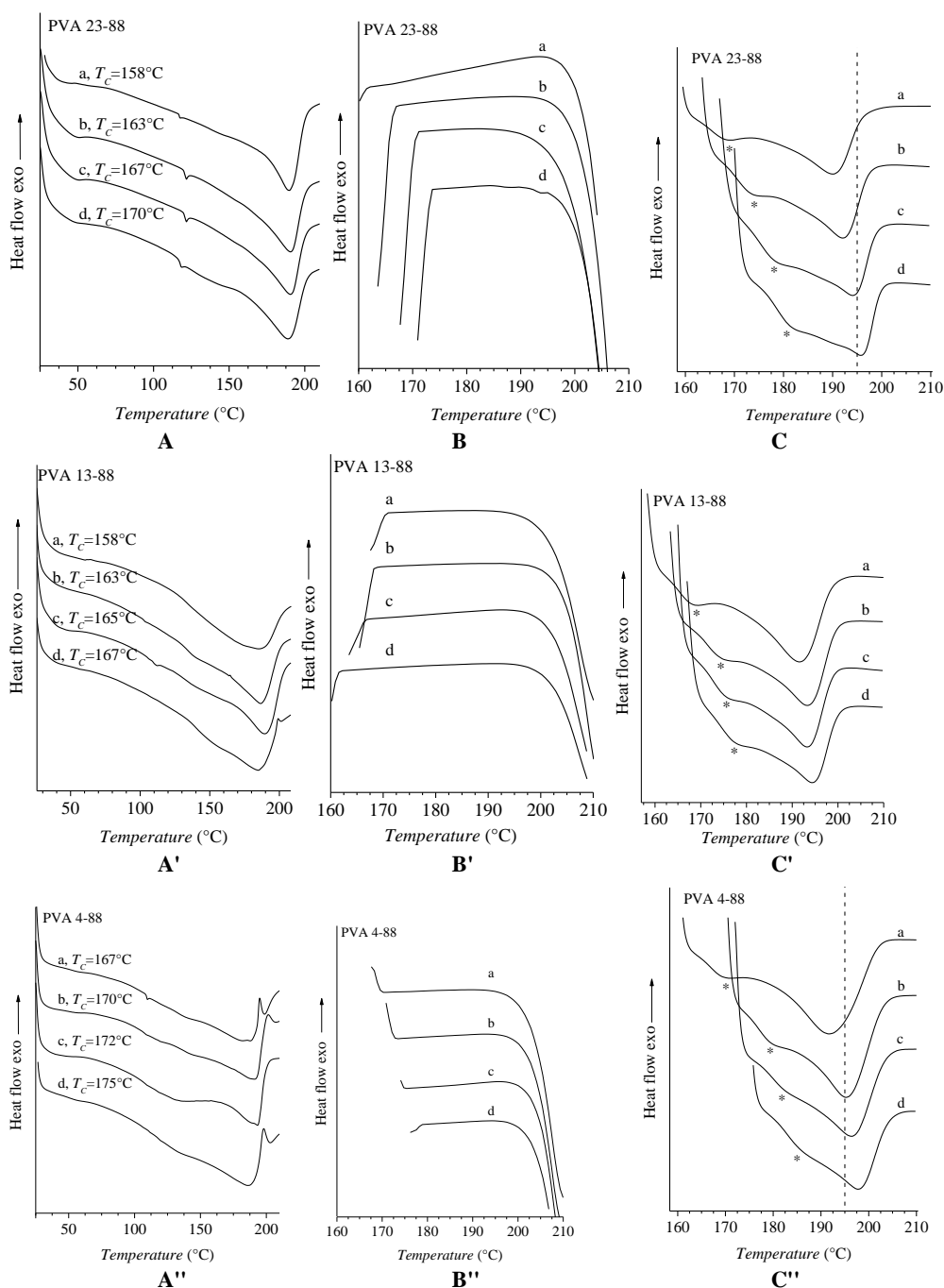
The results of isothermal crystallization analysis are reported in Figure 3.11-Figure 3.12. After a first heating up to 210°C (Figure 3.11-A-A"), DSC thermograms were recorded during isothermal crystallization at different crystallization temperatures ( $T_c$ ) until complete crystallization at the selected  $T_c$  was achieved (Figure 3.11-B-B"). Then, each sample was heated from  $T_c$  to 210 °C (Figure 3.11-C-C"). The isothermal crystallization temperatures,  $T_c$ , were selected in the range between the  $T_c$  and  $T_m$  determined from DSC thermograms of Figure 3.7.

The crystallization isotherms at different  $T_c$  are reported in Figure 3.12 as a function of time. They present a bell-shaped single peak (Figure 3.12, A-C). The DSC curves recorded during the successive heating (Figure 3.11, C- C"),

## Chapter 3

---

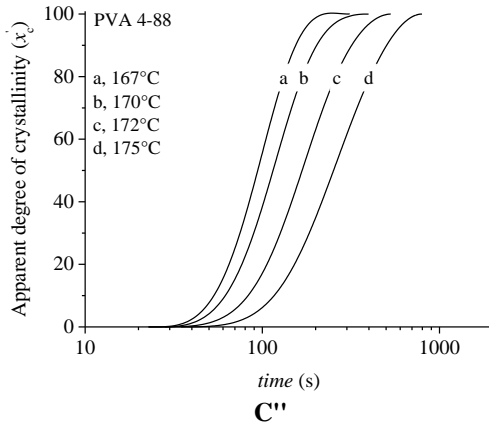
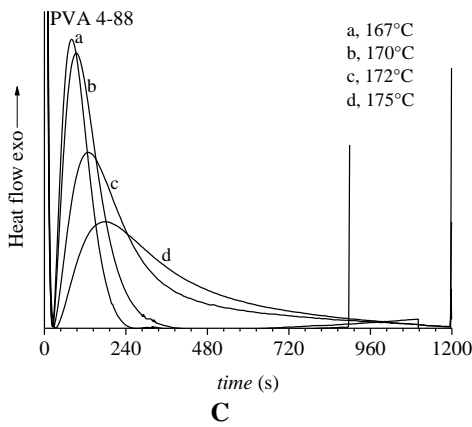
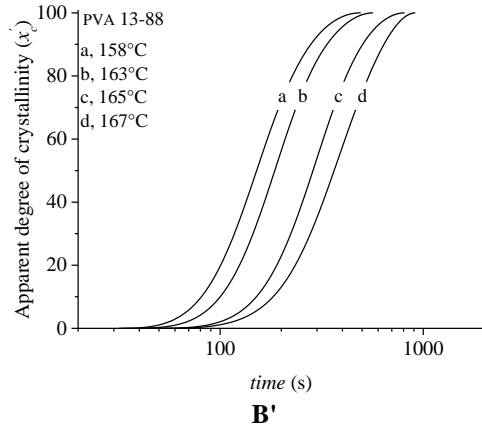
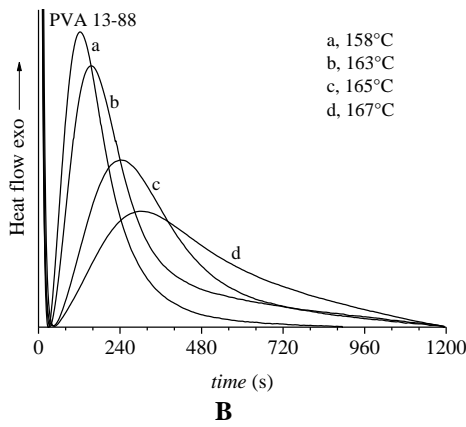
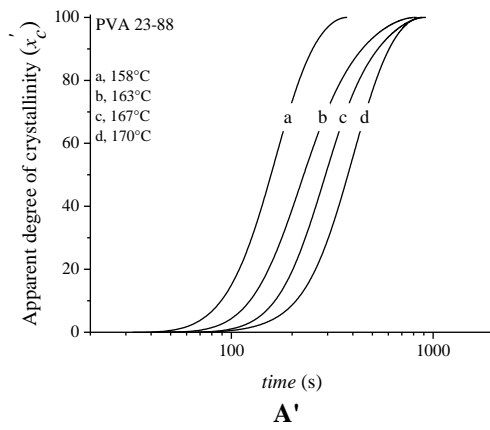
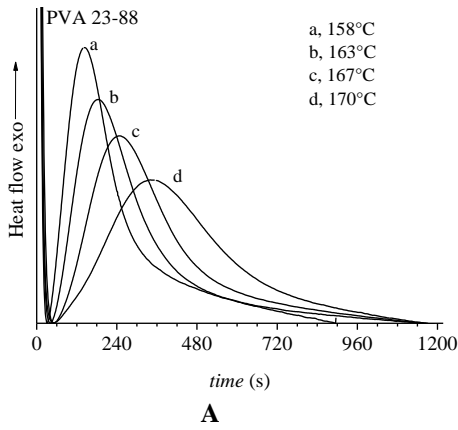
instead, show broad and complex endotherms. In particular, it is apparent that the melting starts immediately above the crystallization temperature (starred peaks). The fact that melting starts immediately above the crystallization temperature may be attributed to the presence of not yet well formed crystals during the isothermal crystallization step. The melting peak is present at temperatures that increase with  $T_c$  (Figure 3.11, C-C"). In this analysis special attention was dedicated to the selection of the maximum temperature achieved in the melt (210°C), in order to prevent degradation phenomena. Moreover, the isothermal crystallizations were performed on independent specimens and each measurement was repeated at least three times in independent experiments to probe the reproducibility.



**Figure 3.11:** DSC thermograms of PVA-resins, recorded during the 1st heating (A-A''), successive isothermal step at different  $T_c$  (B- B'') and 2nd heating after the isothermal step (C- C'') at a scanning rate of  $10^\circ\text{C}/\text{min}$  for the samples PVA 23-88 (A-C), PVA 13-

# Chapter 3

88 (A'-C') and PVA 4-88 (A''-C''). Part B-B'' are reported to check the absence of crystallization during the cooling step from 210°C to the selected  $T_c$ .



**Figure 3.12: DSC thermograms recorded during the isothermal crystallization at the indicated crystallization temperatures  $T_c$  (A-C) and apparent crystallinity,  $x'_c$ , (A'-C') as a function of the crystallization time of PVA samples; relative to the sample PVA 23-88 (A-A'), PVA 13-88 (B-B') and PVA 4-88 (C-C').**

The DSC data, recorded during the isothermal crystallization at various  $T_c$  as a function of crystallization time were used to evaluate the apparent degree of crystallinity defined as:

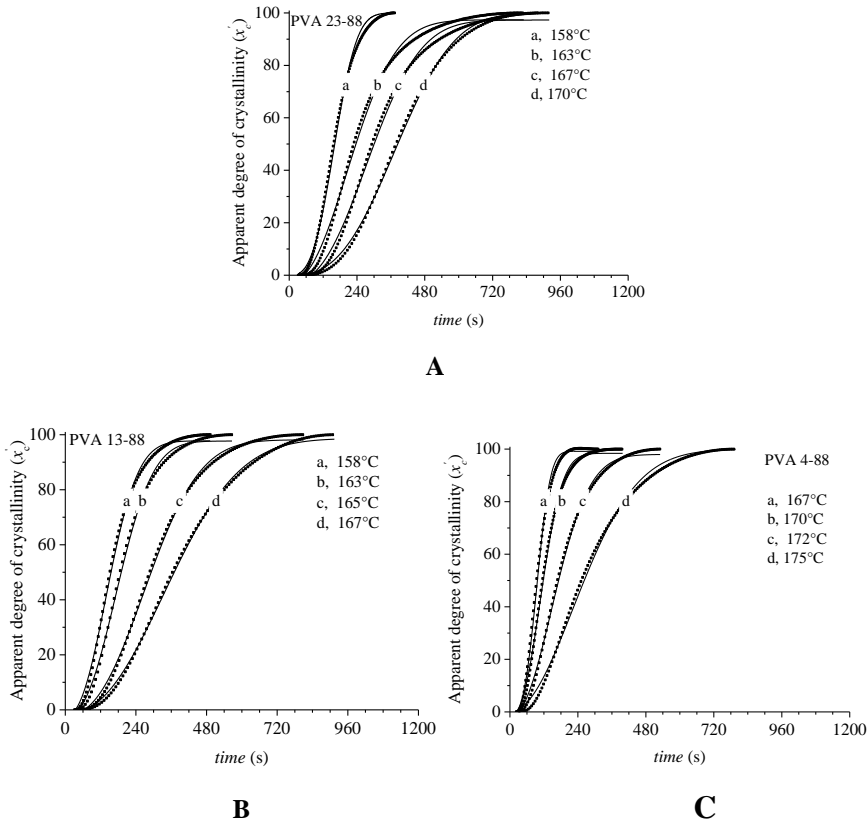
$$x'_c(t) = \Delta H_c(t) / \Delta H_\infty \quad \text{eq. 3.3}$$

where  $\Delta H_c(t)$  is the enthalpy of crystallization at time  $t$  and  $\Delta H_\infty$  is the total crystallization enthalpy evolved up to complete crystallization. The obtained classical sigmoidal curves are shown in Figure 3.12 A'-C' and in Figure 3.13. Experimental data can be fitted to the conventional Avrami equation [10]:

$$x'_c(t) = \left\{ 1 - \exp \left[ - \ln(2) (\Delta t / t_{1/2})^n \right] \right\} \quad \text{eq. 3.4}$$

where  $\Delta t$  is the elapsed time ( $t - t_{ind}$ ) from the induction time  $t_{ind}$  of incipient crystallization,  $t_{1/2}$  is the half crystallization time and  $n$  the Avrami exponent. This equation, derived for isothermal crystallization kinetics, follows the assumptions that nucleation rate is either zero (i.e. crystallization occurs due to the growth of pre-existing heterogeneous nuclei) or constant.[7]–[9]

The fitted curves are reported in Figure 3.13. The value of the Avrami exponent  $n$  reflects the type of nucleation and the geometry of the growth morphology. Generally, the Avrami exponent  $n$  is equal to 1, 2, 3 in case of heterogeneous nucleation, or equal to 2, 3, 4 in case of homogeneous nucleation and corresponds to growth in 1, 2 and 3 dimensions in the two cases, respectively. The fit to the data corresponds to Avrami exponents included in the range 2-3. This indicated either a heterogeneous nucleation in 2 or 3 dimensions, respectively, or homogeneous nucleation in 1 and 2 dimensions, respectively. The fitting parameters of kinetics data to eq. 3.4 are reported in Table 3.6.



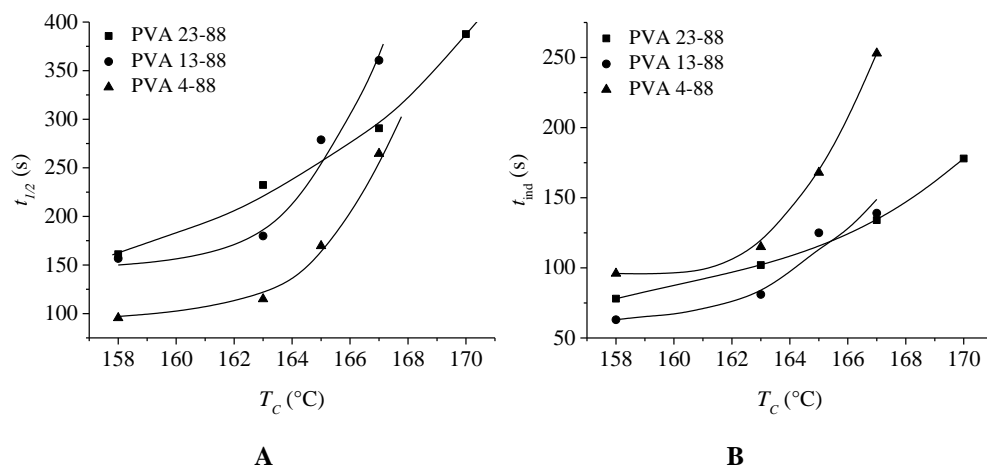
**Figure 3.13:** Apparent crystallinity,  $x'_c$ , as a function of the crystallization time at different  $T_c$ , for samples PVA 23-88 (A), PVA 13-88 (B) and PVA 4-88 (C). Experimental data points are shown as small dots and the corresponding fitted curves as solid lines.

**Table 3.6:** Values of induction time ( $t_{ind}$ ), half-crystallization time ( $t_{1/2}$ ) and Avrami exponent  $n$  for the PVA resins samples isothermally crystallized from the melt at the temperatures  $T_c$ .

Sample	$T_c$ (°C)	$t_{ind}$ (s)	$t_{1/2}$ (s)	$n$
PVA 23-88	158	78	161.0 ± 0.3	3.00 ± 0.01
	163	102	232.0 ± 0.7	2.50 ± 0.01
	167	134	291.1 ± 0.4	2.43 ± 0.01
	170	178	388.0 ± 0.3	3.00 ± 0.01
PVA 13-88	158	63	157.0 ± 0.4	2.00 ± 0.01
	163	81	180.1 ± 0.5	2.10 ± 0.01
	165	125	279.0 ± 0.5	2.20 ± 0.01
	167	139	360.0 ± 0.3	2.20 ± 0.01
PVA 4-88	167	44	96.0 ± 0.3	3.0 ± 0.1

<b>170</b>	49	$115.0 \pm 0.4$	$2.40 \pm 0.01$
<b>172</b>	63	$170.1 \pm 0.5$	$2.30 \pm 0.01$
<b>175</b>	78	$264.2 \pm 0.5$	$2.10 \pm 0.01$

The values of the half-crystallization time,  $t_{1/2}$ , for all resins as a function of the crystallization temperature are reported in Figure 3.14-A. The  $t_{1/2}$  of pure resins in isothermal conditions increases with increase of crystallization temperature achieving values of about 1-2 min at the lowest crystallization temperature and of  $\approx 7$  min at the highest crystallization temperature. As shown in Figure 3.14-B, the induction time increases with the crystallization temperature and it is of the order of  $\approx 60$  s at the lowest  $T_c$ . and  $\approx 250$  s at the highest temperature. The crystallization kinetics of the samples PVA 23-88 and 13-88 are similar, whereas the sample PVA 4-88 shows the highest crystallization rate due to the lower molecular mass.

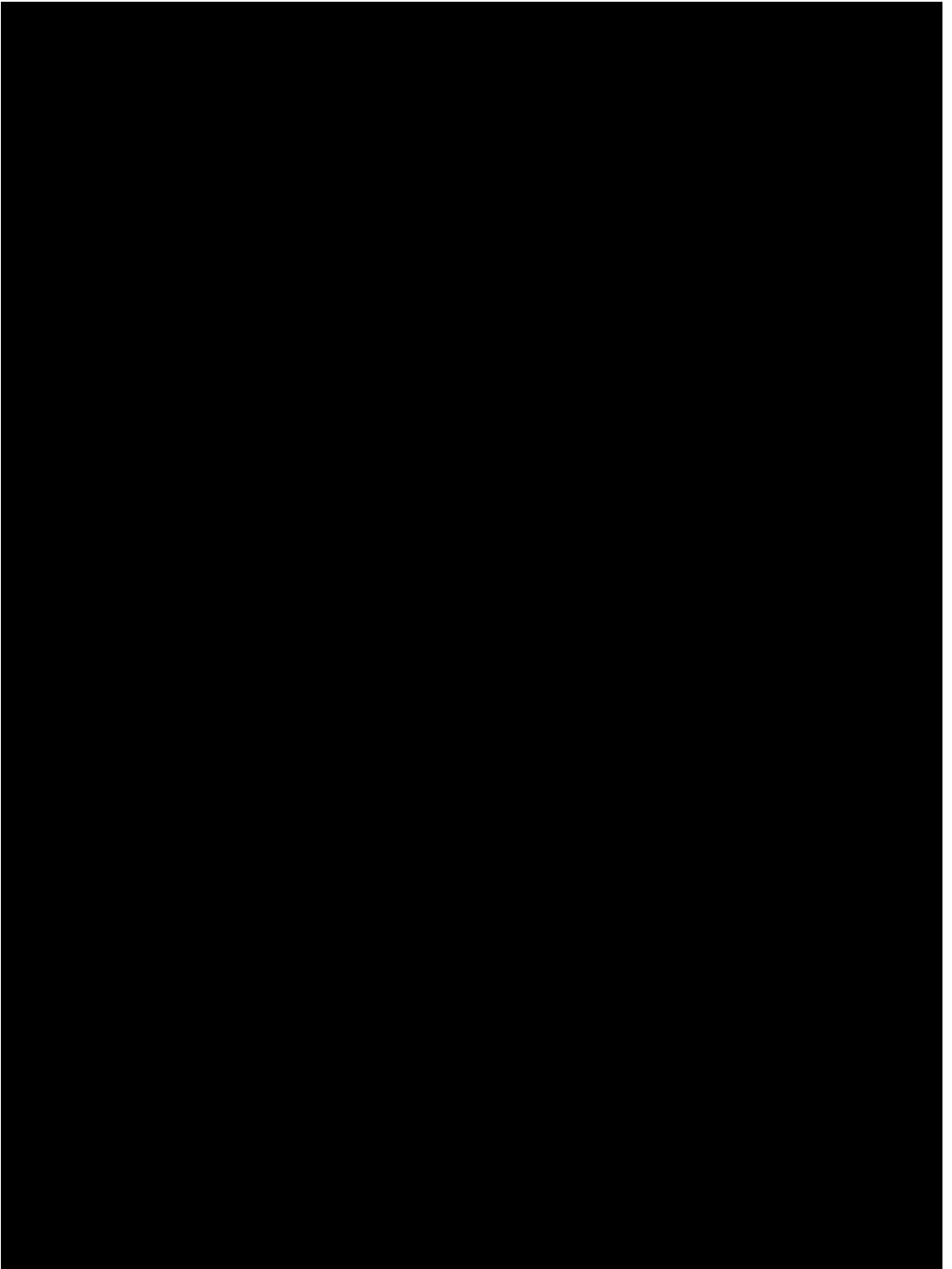


**Figure 3.14:** Half-crystallization time,  $t_{1/2}$ , (A) and induction time,  $t_{ind}$ , (B) as a function of the crystallization temperature,  $T_c$ , for the samples PVA 23-88 (squares), PVA 13-88 (circles) and PVA 4-88 (triangles). Solid lines are a guide to the eye.

The most important result of the present analysis consists in having established in anhydrous conditions the characteristic crystallization times of our resins. These characteristic times are of the order of few minutes at







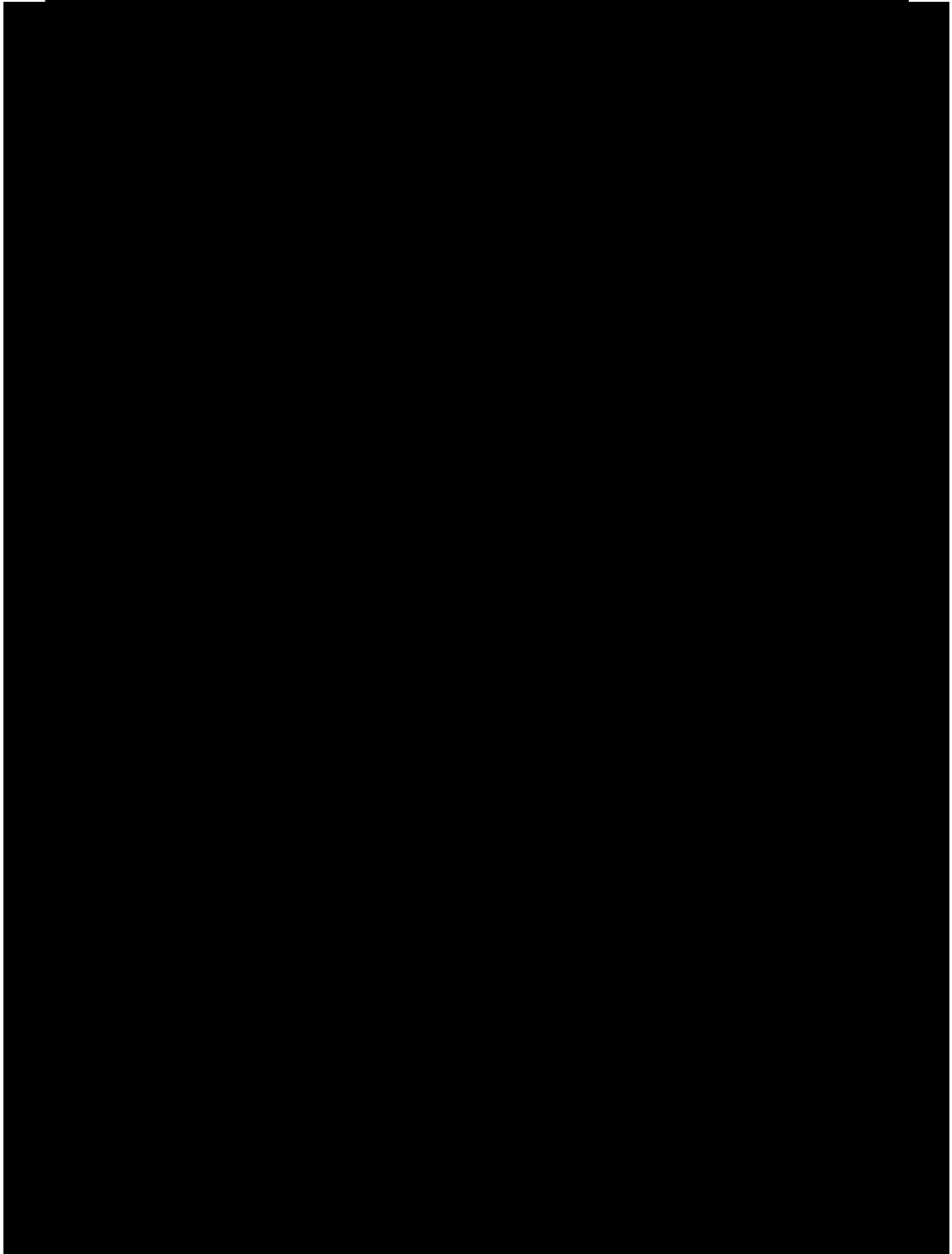
**Table 3.7: Mechanical parameters extracted from stress-strain curves of Figure 3.15.**

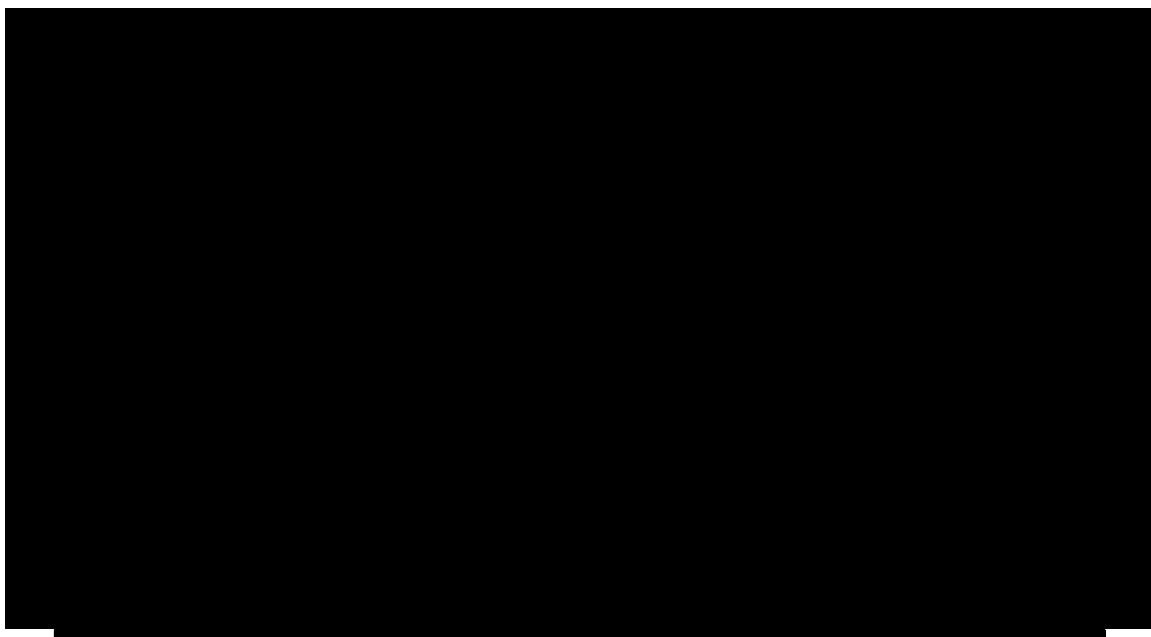
Sample	Modulus (GPa)	Yield Stress (MPa)	Ultimate Tensile Stress (MPa)	Strain at Yield (%)	Strain at Break (%)	Elongation at Break (%)
1	1.2	100	150	8.3	166.7	166.7
2	1.5	120	180	8.0	180.0	180.0
3	1.8	140	210	7.8	210.0	210.0
4	2.1	160	240	7.6	240.0	240.0
5	2.4	180	270	7.5	270.0	270.0

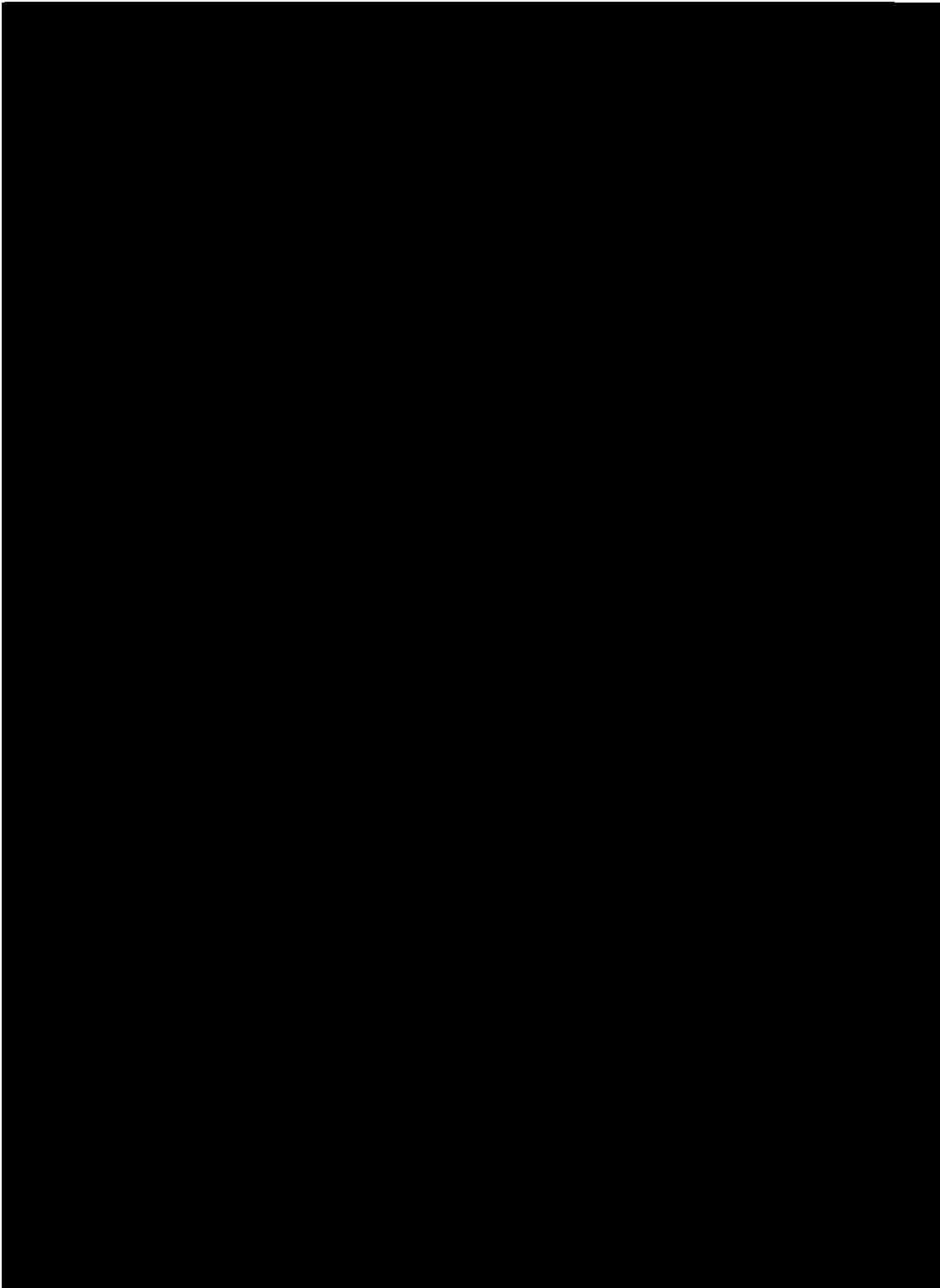
### 3.5 X-ray fiber diffraction analysis



The X-ray diffraction patterns of fibers of the stretched films at increasing values of strain,  $\epsilon$ , within a range from 0 to 200%, are shown in Figure 3.16-3.17. In both cases, stretching produces orientation of crystals without improving the crystallinity. This analysis confirms that not significant orientation of crystals is present in the non-oriented films.







### 3.6 Conclusion to Chapter 3

The preliminary characterization of the PVA grades and [REDACTED] [REDACTED] indicates that all the samples show a high level of crystallinity ( $\approx 30\%$  for the blends and  $\approx 45\%$  for the pure grades), relatively high melting temperatures ( $\approx 170\text{-}200\text{ }^{\circ}\text{C}$ ), good crystallization rates in anhydrous conditions, even at temperatures close to melting (temperature range  $158\text{-}170\text{ }^{\circ}\text{C}$ ), tendency to thermal degradation at temperatures close to  $200\text{-}250\text{ }^{\circ}\text{C}$ , Young moduli of the order of  $10\text{-}30\text{ MPa}$ , a high ductility with deformation at break higher than  $400\%$ , large strain hardening at high deformations, and high level of toughness. Moreover all the samples contain a non-negligible amount of water ( $5\text{-}10\text{ wt}\%$ ) in agreement with the hydrophilic nature of PVA.

---

## References

- [1] C. W. Bunn, “Crystal Structure of Polyvinyl Alcohol,” *Nature*, vol. 161, no. 4102, pp. 929–930, 1948.
- [2] R. Ricciardi, F. Auriemma, C. Gaillet, C. De Rosa, and F. Lauprêtre, “Investigation of the crystallinity of freeze/thaw poly(vinyl alcohol) hydrogels by different techniques,” *Macromolecules*, vol. 37, no. 25, pp. 9510–9516, 2004.
- [3] Y. Tsuchiya and K. Sumi, “Thermal decomposition products of poly(vinyl alcohol),” *J. Polym. Sci. Part A-1 Polym. Chem.*, vol. 7, no. 11, pp. 3151–3158, 1969.
- [4] B. J. Holland and J. N. Hay, “The thermal degradation of poly(vinyl alcohol),” *Polymer*, vol. 42, no. 16, pp. 6775–6783, 2001.
- [5] P. S. Thomas, J. P. Guerbois, G. F. Russell, and B. J. Briscoe, “FTIR study of the thermal degradation of poly(vinyl alcohol),” *J. Therm. Anal. Calorim.*, vol. 64, no. 2, pp. 501–508, 2001.
- [6] N. a Peppas and P. J. Hansen, “Crystallization Kinetics of Poly(vinyl Alcohol),” *J. Appl. Polym. Sci.*, vol. 27, pp. 4787–4797, 1982.
- [7] M. Avrami, “Kinetics of phase change. I: General theory,” *J. Chem. Phys.*, vol. 7, no. 12, pp. 1103–1112, 1939.
- [8] M. Avrami, “Kinetics of phase change. II Transformation-time relations for random distribution of nuclei,” *J. Chem. Phys.*, vol. 8, no. 2, pp. 212–224, 1940.
- [9] M. Avrami, “Granulation, phase change, and microstructure kinetics of phase change. III,” *J. Chem. Phys.*, vol. 9, no. 2, pp. 177–184, 1941.
- [10] R. Pantani, F. De Santis, F. Auriemma, C. De Rosa, and R. Di Girolamo, “Effects of water sorption on poly(lactic acid),” *Polym. (United Kingdom)*, vol. 99, pp. 130–139, 2016.

# Chapter 4

## Study of PVA/water systems

*Water is a very good servant, but it is a cruell maister.*

*William Bullein*



### **4.1 Introduction**

The interaction between PVA and water is a crucial parameter influencing the dynamic of the welding process and the final properties of PVA films and of the welding interface. Indeed, the properties of polymers, which have hydrophilic groups such as hydroxyl, carboxyl and carbonyl, are strongly influenced by the presence of water.

Depending on the degree of chemical or physical association between the water and polymer species, the hydrated polymer can exhibit different physical properties. The solvent can induce structural changes in the polymer matrix, act as plasticizer or even form stable bridges through hydrogen bonding, up to reduce the chain dynamics, thus, resulting in an anti-plasticizing effect. Moreover, the type of interaction between water and polymer chains leads to the presence of different population of absorbed water molecules, characterized by different mobility inside the polymer matrix, and can influence the absorption rate and the total amount of absorbed solvent molecules.

In this perspective, the effect of water on PVA films properties, as well as the absorption and the diffusion mechanisms were studied.

In the following sections, before the presentation of the experimental results, basic concepts on diffusion mechanisms of small molecules in a polymer matrix are discussed.

#### **4.1.1 Diffusion processes in polymeric matrices**

The absorption of small molecules, named diffusant or permeant, into a material is governed by the diffusion. The interpretation of the diffusion processes results quite complex in polymers. To have a trustworthy description

of the phenomenon, the properties of the diffusant, the polymer network, as well as the interactions taking place in the system, should be all considered.

Diffusion can be defined as the transport of matter in a system by means of random molecular motion, which acts to remove chemical potential differences and will eventually produce an equilibrium state of concentration [1]. The motion of the diffusant dissolved in a polymer can be thought of as a series of random walks between absorption sites.

At first instance, for a more clear description of the phenomenon, it is useful to split the diffusion in two different steps. The first step is the absorption at the interface happening for a small portion of volume where the equilibrium is locally reached. After this step, the penetrant is able to diffuse into the material until the final equilibrium, ruled by the characteristic diffusion times.

The chemical composition of the polymer has a strong influence on the solubility and diffusion properties of molecules in the polymeric matrix. In particular, the gyration radius of the polymer, and mesh size of the polymer network should play a key role. Intermolecular interactions or additional interactions between the molecules and polymer chain may induce structural transformation, such as swelling. On the other hand, also the type of diffusant influences the diffusion process, for instance, the dimension of the molecules and the plasticizing effect can affect the segmental mobility of the polymeric chains.

Lastly, in hydrophilic semicrystalline polymers, the diffusion becomes more complex because of the existence of specific interactions (non-polar or polar) and dynamic heterogeneities between amorphous and crystalline phases. For instance, the degree of crystallinity plays a crucial role in systems where the quantity of the diffusant absorbed by the crystalline phase is negligible with respect the fraction absorbed in the amorphous phase.

Over the past years, several theoretical models have been developed to interpret the mechanisms lying at the base of diffusion processes. Even if encouraging progress has been made in this field, the most part of the models presents some limitations and controversies between them are not uncommon. Thus, a certain attention should be put using a specific model to interpret experimental data. It still remains a challenge to predict the rate and the diffusion coefficient of a given diffusant in a given system under specific conditions.

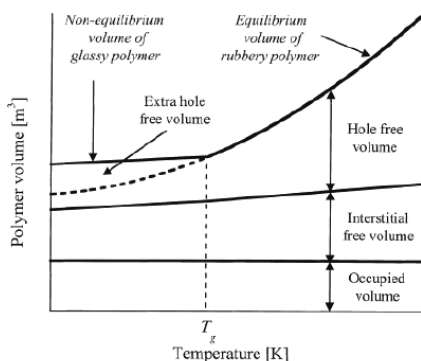
The following sections provide a short overview of few theories and physical models helping to describe diffusion through polymer matrices.

### **4.1.2 Free Volume Lattice (FVL) model**

One of the first physical models, describing the correlation between the permeant diffusion and the polymer structure, is the Free Volume Lattice model (FVL). Although this model was developed to describe self-diffusion in liquids by Cohen and Turnbull [2], it was rapidly extended to binary system consisting in a polymeric matrix and a relatively low molecular weight solvent [3]–[5]. The theories, developed starting from the FVL model, are based on the assumption that the free volume is the major factor controlling the diffusion rate of molecules.

According to this model, a molecule moves through jumps between thermally generated micro or nano-voids in the polymer matrix. The ensemble of micro or nano-cavities causes the free volume elements (FVE) or “holes” in the polymeric matrix, creating preferential pathways of diffusion. More precisely, the model envisions the volume in the matrix as core volume, occupied by the polymer chains, which is not involved in diffusion, and free volume that determines the transport properties. Free volume elements

continuously form and disappear because of thermal motions of the polymer chains. When a void forms adjacent to the diffusing molecule and is large enough to contain it, the molecule can jump into it, where it will remain until another favorable polymer chain thermal motion occurs, creating a new void of suitable size [6], [7]. It is found that diffusion mechanisms are different, whether the polymer is in the rubbery or glassy state. The reason lies in the differences of the polymer structure and dynamics below and above its glass transition temperature,  $T_g$ , resulting in differences of the free volume accessible (Figure 4.1).



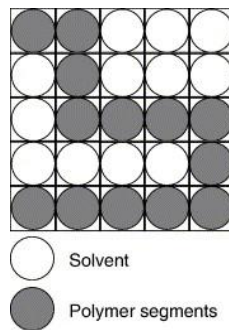
**Figure 4.1: The different contributions to a polymer's volume as a function of temperature. From [7].**

Above the  $T_g$ , when the polymer is in the rubbery state, a certain mobility of chains is allowed, originating holes from their imperfect packing. In this case, the free volume elements have a fluctuating nature, like in liquids, and are composed of hole components that require no energy for volume redistribution and interstitial components that become available to transport owing to energy fluctuations greater than  $kT$ . Cooling the system thermal motions are slowed down and consequently the free volume decreases. Below the  $T_g$ , the chain mobility is extremely reduced and the entire system can be considered as *frozen*. The excess of FVE is therefore trapped into the matrix and the polymer

is not in an equilibrium state. However, it should be noted that, although the thermal fluctuations of a glassy polymer are strongly reduced with respect to a rubbery polymer, they are not completely eliminated. This means that, eventually, the glassy polymer will reach equilibrium, redistributing the free volume and losing the excess of free volume. This densification process usually happens on longer timescales of weeks or years and depends on the size and the shape of the polymer sample [7].

### 4.1.3 Thermodynamic description of diffusion in binary systems: the *Flory-Huggins* theory

The *Flory-Huggins* theory is based on a *lattice fluid* model where polymer and diffusant particles occupy imaginary positions, as shown in Figure 4.2, where the macromolecule is considered linear and constituted of  $r$  segment that occupy a volume  $V_2 = rV_1$ , in which  $V_1$  is the solvent volume.



**Figure 4.2: Flory-Huggins two dimensional lattice representation.**

The only contribution to the entropy of the system is given by the configurational entropy expressed by the Boltzmann relation:

$$S_{conf} = k \ln W \quad \text{eq. 4.1}$$

where  $k$  is the Boltzmann constant and  $W$  is the number of accessible states of the system. In other words,  $W$  corresponds to the number of modes to collocate  $N_1$  molecules of solvent and  $N_2$  molecules of polymer in the lattice sites. If the

first segment of the polymer has  $N_1+rN_2$  positions available into the lattice, the second segment will be able to occupy only  $z$  positions, according to the coordination number of the lattice  $z$ ; the third will have  $(z-1)$  free positions and so on. To calculate correctly the number of modes of the system a statistical approach is needed.

Without reporting any detailed treatment of the statistical calculus, the entropic energy of mixing of the species is given by:

$$\Delta S_{mix} = R(n_1 \ln v_1 + n_2 \ln v_2) \quad \text{eq. 4.2}$$

where  $v_{1,2}$  are volume fraction respectively of solvent and polymer and  $n_{1,2}$  the moles of solvent and polymer:

$$v_1 = \frac{n_1}{n_1 + rn_2}; v_2 = \frac{rn_2}{n_1 + rn_2} \quad \text{eq. 4.3}$$

The internal energy of mixing  $\Delta H_{mix}$  can be written as:

$$\Delta H_{mix} = RT\chi_{12}n_1v_2 \quad \text{eq. 4.4}$$

In eq. 4.4,  $\chi_{12}$  is the *Flory-Huggins* parameter which arises from the variation in internal energy, owing to the interactions between the two species and is constant for a given polymer-solvent pair in isotherm conditions.

From eq. 4.2 and eq. 4.4, the free energy is obtained, leading to the *Flory-Huggins* equation:

$$\Delta G_{mix} = RT[\ln v_1 + n_2 \ln v_2 + n_1v_2\chi_{12}] \quad \text{eq. 4.5}$$

Finally, for a given polymer-solvent pair, the variation of chemical potential, expressed as difference between  $\mu_1$ , the chemical potential of the one mole of penetrant into the polymer and  $\mu_1^0$ , the reference chemical potential for a standard state (0), is given by:

$$\mu_1 - \mu_1^0 = RT[\ln \phi_1 + \phi_2(1 - 1/r) + \phi_2\chi_{12}] \quad \text{eq. 4.6}$$

Over the years, many theories have been developed, starting from the *Flory-Huggins* model, introducing modification to describe the diffusion of molecules into polymers above the  $T_g$ , such as the *Sanchez-Lacombe* [8]–[10] and the *Simha-Somcinsky* models [11] or introducing parameters to consider specific interaction between the polymer and solvent, as in the *Panayiotou-Sanchez* model that accounts for H-bonding interaction[12], [13].

#### 4.1.4 Fickian diffusion

The first mathematical treatment of diffusion was established by Fick who developed a law for diffusion in one dimension. The second Fick's law is here reported:

$$\frac{dc}{dt} = D \frac{d^2c}{dx^2} \quad \text{eq. 4.7}$$

where  $c$  is the penetrant concentration at the time  $t$  and position  $x$  and  $D$  is the diffusion coefficient [1]. By integration of the equation, it can be obtained the theoretical concentration the profile  $c(x, t)$  as a function of time and space, using a proper physical model able to describe the diffusion. Indeed, eq. 4.7 is the starting point of numerous models of diffusion in polymer systems.

From the second Fick's law, Crank [14] derived the equation of the concentration profile in a polymeric film of width  $2l$ , assuming that the concentration of the diffusant is initially uniform within the material and that the surface concentration is immediately brought to zero. More in details, integrating the concentration over the width  $2l$ , the second Fick's law can be replaced by the following equation [14]:

$$\frac{M(t)}{M_\infty} = 4 \left( \frac{Dt}{l^2} \right)^{1/2} \cdot \left[ \frac{1}{\pi^{1/2}} + 2 \sum_{n=0}^{\infty} (-1)^n \text{ierfc} \frac{nl}{2(Dt)^{1/2}} \right] \quad \text{eq. 4.8}$$

where  $M(t)$  is mass of the diffusant at time  $t$  and  $M_\infty$  is the equilibrium mass at long times. In the eq. 4.8,  $\text{ierfc}(x)$  corresponds to:

$$\text{ierfc}(x) = \int_x^\infty \text{erfc}(\xi) d\xi = \frac{1}{\pi^{1/2}} e^{-x^2} - x \text{erfc}(x) \quad \text{eq. 4.9}$$

where  $\text{erfc}(x)$  is the complementary error function of  $\text{erf}(x)$  defined as

$$\text{erf}(x) = 1 - \frac{2}{\sqrt{\pi}} \int_0^x \exp(-u^2) du \quad \text{eq. 4.10}$$

For small values of  $t$ , eq. 4.8. can be approximated to:

$$\frac{M(t)}{M_\infty} = 4 \left( \frac{Dt}{\pi l^2} \right)^{1/2} = \left( \frac{16D}{\pi l^2} \right)^{1/2} \cdot t^{1/2} \quad \text{eq. 4.11}$$

The Crank model can be applied to Fickian cases where the diffusion coefficient is independent from the concentration of the diffusant and, as shown in eq. 4.11,  $M(t)/M_\infty$  is a linear function of  $t^{1/2}$ .

Limited examples of Fickian diffusion are reported in literature while a plethora of non-Fickian cases can be found. For this reason, modeling the non-Fickian diffusion has been a challenge in the latest decades.

### 4.1.5 Non Fickian diffusion

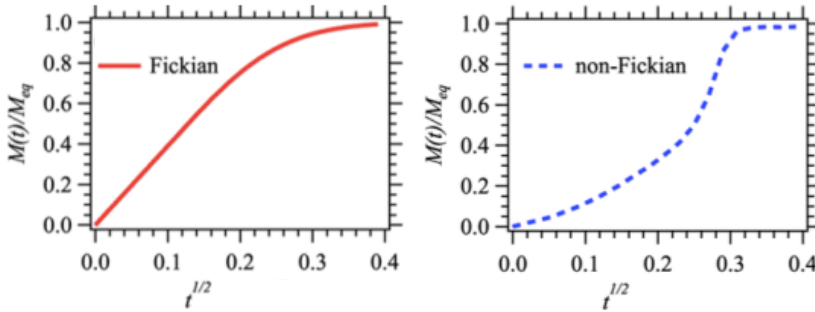
The eq. 4.12 is a general equation that can be used to describe solvent diffusion behaviors for any polymer-penetrant system whatever the temperature and the penetrant activity:

$$M(t) = kt^n \quad \text{eq. 4.12}$$

where  $k$  is a constant and  $n$  a parameter related to the diffusion mechanism, whose value lies between  $1/2$  and 1. In the previous paragraph, the dependence of  $M(t)$  on  $t^{1/2}$  has been demonstrated for the Fickian case. Experimentally, non-Fickian diffusion can be defined as lack of linearity in the initial part of



the curve  $M(t)$  vs  $t^{1/2}$ . For Case II diffusion,  $n$  is typically equal to 1, while anomalous behaviors show intermediate values between  $1/2$  and 1.



**Figure 4.3:**  $M(t)$  vs  $t^{1/2}$  trends for Fickian (on the left) and non-Fickian (on the right) diffusion cases. Adapted from [15].

Alfrey et al. [16] suggested a classification based on the solvent diffusion rate and the polymer relaxation rate according to which the mechanisms can be classified as: Fickian or Case I and non-Fickian mechanisms, distinguished in Case II and anomalous case diffusion. Fickian and Case II diffusions are considered as limiting types of transport processes whereas anomalous diffusion lies in between.

In Case I, the polymer relaxation rate is faster than the diffusion ( $R_{\text{diff}} \ll R_{\text{relax}}$ ). Indeed, the Fickian behavior is mainly observed in the rubbery state, when the temperature is well above the glass transition temperature of the polymer,  $T_g$ . This condition makes the penetration of the solvent easier, due to the high chains mobility [17]. Thus, the solvent diffusion rate is slower than the polymer relaxation rate.

On the contrary, in Case II diffusion, the solvent diffusion rate is faster than the polymer relaxation process ( $R_{\text{diff}} \gg R_{\text{relax}}$ ), whereas in anomalous diffusion the solvent diffusion rate and the polymer relaxation are about the same order of magnitude ( $R_{\text{diff}} \approx R_{\text{relax}}$ ) [16]. This kind of diffusion occurs in polymers

below the  $T_g$  in the glassy state, as the chains have reduced mobility that obstacles the diffusion of the solvent in the polymer core [17].

Case II diffusion is particularly interesting because occurs in polymer-penetrant systems in which the penetrant substantially swells the polymer. The characteristics of this type of diffusion are the following: (1) a rapid increase in the solvent concentration in the swollen region which leads to a sharp solvent penetration front between the swollen region and the inner polymer core; (2) the solvent concentration is quite constant in the swollen region behind the solvent penetration front; (3) the solvent penetration front is sharp and advances at a constant rate, thus the diffusion distance is directly proportional to time; (4) there is an induction time of Fickian concentration profile which precedes the solvent penetration front into the polymer core [18]–[20].

Over the years, different models have been proposed to describe the non-Fickian behavior. Frish et al [21] proposed a modification of the Fick's law, introducing additional terms to correct the anomalous diffusional behavior. The chief drawback is that these terms have no physical meaning, even if their equation describes well the time dependence of some systems.

A second approach has been proposed by Peterlin [22], [23], who proposed that the diffusion front is preceded by a region of penetrant at low concentration which forms a precursor to the front, and results from essentially Fickian controlled diffusion ahead of the front. He described the sharp front as consequence of a strong dependence of solubility and diffusion coefficient on concentration [24]. The limitation of this model lays on the assumption that the front moves at constant velocity, thus the interpretation is unable to describe situations in which the front either decelerates with time [19] or accelerates

[25]. Thus, the model cannot predict the kinetics of Case II diffusion, probably the most interesting aspect of this diffusion type.

In a similar way, Astarita and Sarti [26] introduced variable boundary conditions to Fick's law to describe the diffusion in the swelling front. However, this approach is not taking into account the concentration dependence diffusion, typical of case II.

Finally, Thomas and Windle [20] suggested that the rate controlling step at the penetrant front is the time dependent mechanical deformation of the polymer in response to the thermodynamic swelling (osmotic) stress. In the same work they provided the thermodynamic description of a Case II diffusion reported in the following section.

#### 4.1.6 Case II thermodynamic approach

By definition, the diffusion is driven by differences in chemical potentials. Hereby, the thermodynamic treatment of the problem is reported, as described in ref. [18], focusing on the description in the case of a swollen polymer matrix. The chemical potential of a penetrant into a swollen polymer with reference to a standard state (0) is expressed by the following equation:

$$\mu_1 - \mu_1^0 = RT \left\{ \frac{G\bar{V}_1}{V_i} \left[ (1 - v_1)^{\frac{1}{3}} - (1 - v_1) \right] + \ln v_1 + (1 - v_1) + \chi(1 - v_1)^2 \right\} \quad \text{eq. 4.13}$$

In eq. 4.13,  $G$  represents the cross-link density of the polymer network,  $\bar{V}_1$  is the molecular volume of the diluent,  $V_i$  is the volume of the swollen polymer,  $v_1$  is the volume fraction of the solvent in the swollen polymer and  $\chi$  is the Flory interaction parameter between polymer and solvent. The first term in the square brackets refers to the change of entropy, due to the constraint of the molecular network upon swelling by effect of the penetrant (swelling is assumed to produce uniform deformation of the network). The other three

terms derive from mixing free energy, according to the Flory theory applied to polymer solutions[27].

If the swelling of the polymer matrix is opposed by an external hydrostatic pressure,  $P$ , which acts on polymer but not on the surrounding liquid, to absorb one mole of solvent of volume  $\bar{V}_1 N_A$  ( $N_A$  is the Avogadro number), an external work  $P\bar{V}_1 N_A$  should be also considered and the eq. 4.13 becomes:

$$\mu_1 - \mu_0^1 = P\bar{V}_1 N_A + RT \left\{ \frac{G\bar{V}_1}{V_i} [(1 - v_1)^{1/3} - (1 - v_1)] + \ln v_1 + (1 - v_1) + \chi(1 - v_1)^2 \right\} \quad \text{eq. 4.14}$$

The same equation can be applied to systems in which the opposition to the swelling comes from the kinetic immobility of the molecular network instead of an external pressure and, therefore, it can be applied also below the glass transition temperature. The pressure  $P$  can be considered as an additional pressure in the imbibed liquid which affects the chemical potential and points to the relevance of the osmotic analogy.

At this point, the activity,  $a_1$ , can be introduced using its more traditional definition:

$$\mu_1 - \mu_0^1 = RT \ln a_1 \quad \text{eq. 4.15}$$

This means that the activity will depend on pressure as well as concentration. Combining eq. 4.14 and eq. 4.15, the relationship between activity of the penetrant and its volume fraction and the additional pressure is obtained:

$$\ln a_1 = \frac{P\bar{V}_1 N_A}{RT} + \frac{G\bar{V}_1}{V_i} [(1 - v_1)^{1/3} - (1 - v_1)] + \ln v_1 + (1 - v_1) + \chi(1 - v_1)^2 \quad \text{eq. 4.16}$$

Therefore, introducing  $\bar{v}_1$  which is the ratio of volume fraction of penetrant,  $v_1$ , to the equilibrium volume fraction under conditions of zero extra pressure and unit activity, assuming that the chemical behavior is *ideal* it can be written:

$$\bar{V} = (a_1)_{P=0} \quad \text{eq. 4.17}$$

Using equation eq. 4.16 one obtains:

$$\ln \bar{V} = \frac{G\bar{V}_1}{V_i} [(1 - v_1)^{1/3} - (1 - v_1)] + \ln v_1 + (1 - v_1) + \chi(1 - v_1)^2 \quad \text{eq. 4.18}$$

and thus:

$$P = \frac{RT}{\bar{V}_1 N_A} - \ln \left\{ \frac{a_1}{\bar{V}} \right\} \quad \text{eq. 4.19}$$

which is one simple form of the osmotic pressure equation and is identically true for ideal solutions.

In this approach, the entire polymer volume is considered as consisting of the overlap of very thin elements (layers). It is assumed that, at the same instant that a tin element (layer) is put in contact with the penetrant (liquid), the penetrant achieves unit activity. The volume of this element increases by the effect of swelling and the viscosity of the polymer,  $\eta$ , decreases exponentially with increasing penetrant concentration. Therefore, the glassy state of entangled polymer network is taken into account by considering his resistance to volume expansion as dependent on the viscous response to the internal pressure. The simplified eq. 4.19 is used to put in relation the external hydrostatic pressure, acting on the polymer network for each slab, and the concentration of the penetrant, which depends on the viscosity, with the rate of expansion. The fractional swelling of each thin sheet element (slab) is, then, characterized by performing a numerical integration of the resultant equation slab by slab across the entire volume of the polymer film to obtain the concentration profile of the penetrant as a function of the time and the slab position.

In other terms, the Case II thermodynamic approach of ref. [18] explains the transport behavior of a penetrant in a glassy polymer in terms of diffusivity of the penetrant ( $D$ ) and in the hypothesis that the viscous flow rate of a glassy

polymer ( $1/\eta_0$ , where  $\eta_0$  is the viscosity of neat polymer), and its swelling resistance, play a key role.

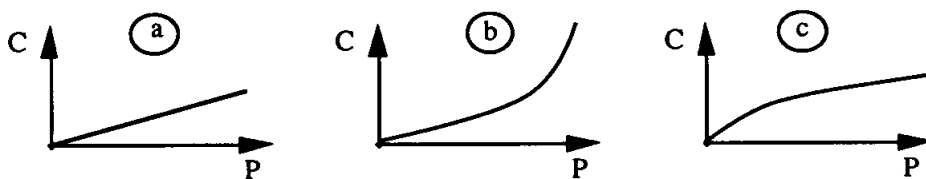
### 4.1.7 Absorption and solubility in polymer/gas systems

For gas penetrants, the solubility,  $S$ , is defined as the ratio between the concentration of the permeant into the material at the equilibrium point,  $c$ , and the external pressure of the penetrant,  $P$ :

$$S = \frac{c}{P} \quad \text{eq. 4.20}$$

At fixed temperature, the equilibrium concentration can be measured at different activity of the penetrant (corresponding to different external pressure), obtaining the so-called *sorption isotherm* curves.

The shape of the *sorption isotherm* curve is related to the interaction between diffusant and polymer [28]. As depicted in Figure 4.4, three types of sorption isotherms can be distinguished.



**Figure 4.4:** Types of sorption isotherm curves. From [28].

The first type corresponds to a linear sorption trend (Figure 4.4-a) where the solubility coefficient is constant and the behavior is described by Henry's law of gas penetrant in liquids in absence of interaction. This first case is often found in rubbery systems with non-polar small diffusant molecules that are weakly interacting with the sites of the polymer.

The second case is the upward isotherm (Figure 4.4-b). This behavior, well described by the Flory-Huggins theory, is more common in absorption of

relatively larger molecules interacting with the polymer in the rubbery state. It is also found that molecules of the diffusant having a certain affinity can form clusters, swelling the host matrix and increasing the free volume and the absorbent capacity of the material. As last case, the downward isotherm (Figure 4.4-c) is associated typically to sorption behavior of glassy polymers.

### 4.1.8 Diffusion and solubility in semicrystalline polymers

As aforementioned, the semicrystalline nature of the polymers affects the diffusion of solvents. Generally, the crystalline phase is less permeable than amorphous region. This is associated to the free volume concept (see paragraph 4.1.2).

The permeability, expressed by the permeability coefficient,  $P$ , corresponds to the product between the diffusion coefficient,  $D$ , and the solubility,  $S$ :

$$P = D \cdot S \quad \text{eq. 4.21}$$

In the assumption that the solubility is negligible in the crystalline regions, and that  $S_a$ , the solubility of the penetrant in the amorphous phase is independent of the presence of crystalline phase,  $S$  can be expressed as:

$$S = S_a \cdot \phi_a \quad \text{eq. 4.22}$$

where  $\phi_a$  is the volume fraction of the amorphous phase [29].

On the other hand, it should be taken into account that the diffusion coefficient is influenced by the polymer morphology (presence of crystalline and amorphous phases). The crystalline regions, more closely packed, hinder the diffusion of the permeant, which is forced to go through longer paths, and introduce a more tortuous path. Moreover, the impermeable crystalline phase and the permeable amorphous phase are considered as interconnected by tie chains. These tie chains cause reduced mobility for the chains in the amorphous

phase. For this reason, generally, for a semicrystalline polymer,  $D$  is corrected as follows:

$$D = \frac{D_a}{\tau\beta} \quad \text{eq. 4.23}$$

$D_a$  is the diffusion coefficient of a completely amorphous polymer. The parameter  $\tau$ , named tortuosity factor, considers the longer different paths that the molecule of the penetrant is obligate to tread, while,  $\beta$ , the immobilization factor, takes into account the reduced mobility of polymeric chains at the interface between the amorphous and crystalline regions [29].

### 4.1.9 Plasticizing effect of solvent on polymer matrix

A plasticizer is usually a small molecule that, interacting with macromolecules, reduces secondary forces between them and creates additional free volume for localized rotational motion. Thus, a plasticizer, increasing the free volume, induces a decrease of the glass transition temperature,  $T_g$ .

For hydrophilic polymers, water can act as plasticizer and since these polymers spontaneously absorb water from the environment their  $T_g$  values depend on the water content.

In general, the glass transition temperature is a critical physical parameter which can drastically change the properties of a material in terms of chemical and physical stability and viscoelastic properties. The glass transition is a complex phenomenon, affected by parameters such as heating rate, ageing history, morphology, molecular weight. Over the years, different models have been developed on the nature of this transition. These theories are based on kinetic or equilibrium hypotheses. In the first case, the glass transition is seen as a dynamic process due to the motion of the chain segments at large scale.



Alternatively, the glass transition can be treated as a true second-order thermodynamic transition. Gibbs and Di Marzio explained the phenomenon in terms of conformational entropy and postulated that the conformational entropy becomes zero when a thermodynamic second-order transition is reached. Below this temperature, all conformations are essentially "frozen".

Several approaches have been proposed for estimating the glass transition temperature of polymers containing plasticizers. Although different in detail, the proposed relationships are all based on the additivity of basic thermophysical properties. Thus, the final behavior of the mixture can be predicted knowing the properties of the pure components. One of the most widely used equations for estimating glass transition temperatures is the Gordon-Taylor equation [30]:

$$T_{g,\text{mix}} = \phi_1 T_{g,1} + \phi_2 T_{g,2} \quad \text{eq. 4.24}$$

where  $T_{g,\text{mix}}$  and  $T_{g,1}$  and  $T_{g,2}$  are the glass transition temperature of the mixture and of component 1 and 2 while  $\phi_1$  and  $\phi_2$  are the volume fractions of each component. Expliciting  $\phi$  as  $\Delta\alpha \cdot w/\rho$  (where  $\Delta\alpha$  is the thermal expansion coefficient,  $w$  is the weight fraction and  $\rho$  is the density) eq. 4.24 becomes:

$$T_{g,\text{mix}} = \frac{w_1 \cdot T_{g,1} + k \cdot w_2 \cdot T_{g,2}}{w_1 \cdot k \cdot w_2} \quad \text{eq. 4.25}$$

where  $k = (\rho_1 \cdot \Delta\alpha_2)/(\rho_2 \cdot \Delta\alpha_1)$ . This equation is especially used for compatible polymer blends. The same equation has been derived for polymer/plasticizer systems by Kelley and Bueche [31].

Considering the Sihma-Boyer rule, according to which  $\Delta\alpha \cdot T_g \approx \text{const}$ ,  $k$  can be obtained from the density of two component. This is useful in the cases for which  $\Delta\alpha$  is unknown, as in the case of the water. Moreover, if the densities are equal, the glass transition temperatures are related as follows:

$$\frac{1}{T_{g,mix}} = \frac{w_1}{T_{g,1}} + \frac{w_2}{T_{g,2}} \quad \text{eq. 4.26}$$

It is reported that the glass transition of water is about  $-138^{\circ}\text{C}$  [32]. The eq. 4.26, known as Fox equation, is a simplification of the Gordon Taylor and has been experimentally verified [33].

## 4.2 Experimental results

In this section, the possible states of water molecules in the different PVA samples is analyzed as a function of water concentration. The states of water, indeed, depend on the possible formation of hydrogen bonds with the PVA chains belonging to the amorphous and crystalline phases, at low water concentration, and formation of weaker mutual interactions with increase of water content. The effect of water concentration is also analyzed on the PVA structure at unit cell length scale, resorting to WAXS analysis, and lamellar length scale, using SAXS measurements. Then, the effect of water content on the mechanical and thermal properties is investigated. Finally, we show the results obtained using classical gravimetry, X-ray diffraction and Dynamic Vapor Sorption (DVS) to probe the water diffusion kinetics in the PVA films.

[REDACTED]

[REDACTED]

[REDACTED]

[REDACTED]

[REDACTED]

[REDACTED]

[REDACTED]

[REDACTED]

[REDACTED]

[REDACTED]

[REDACTED]







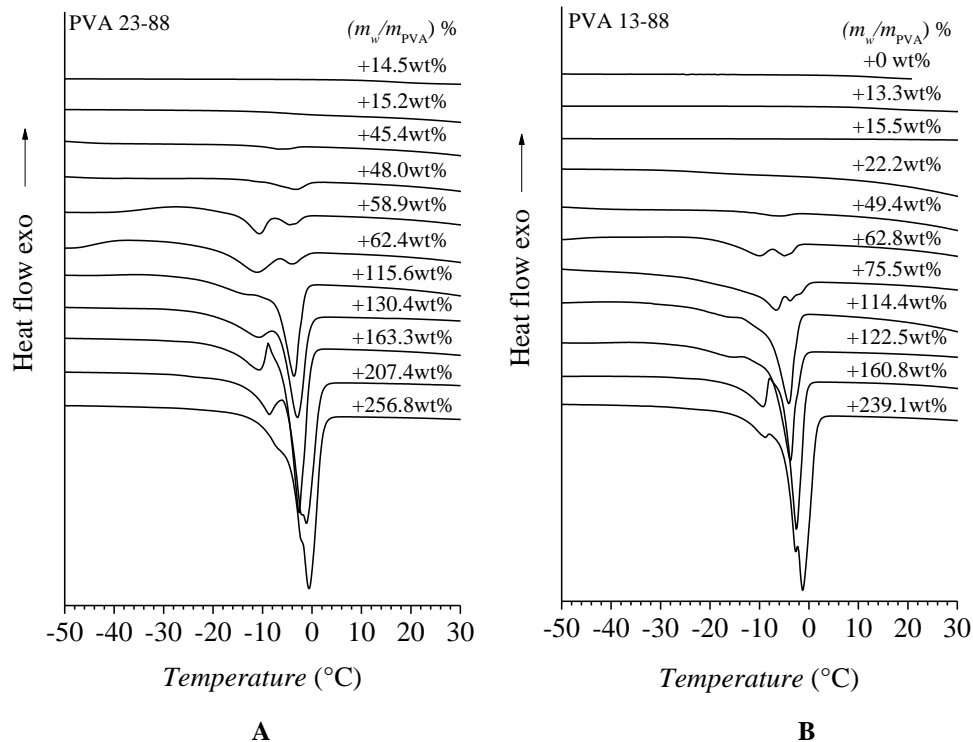
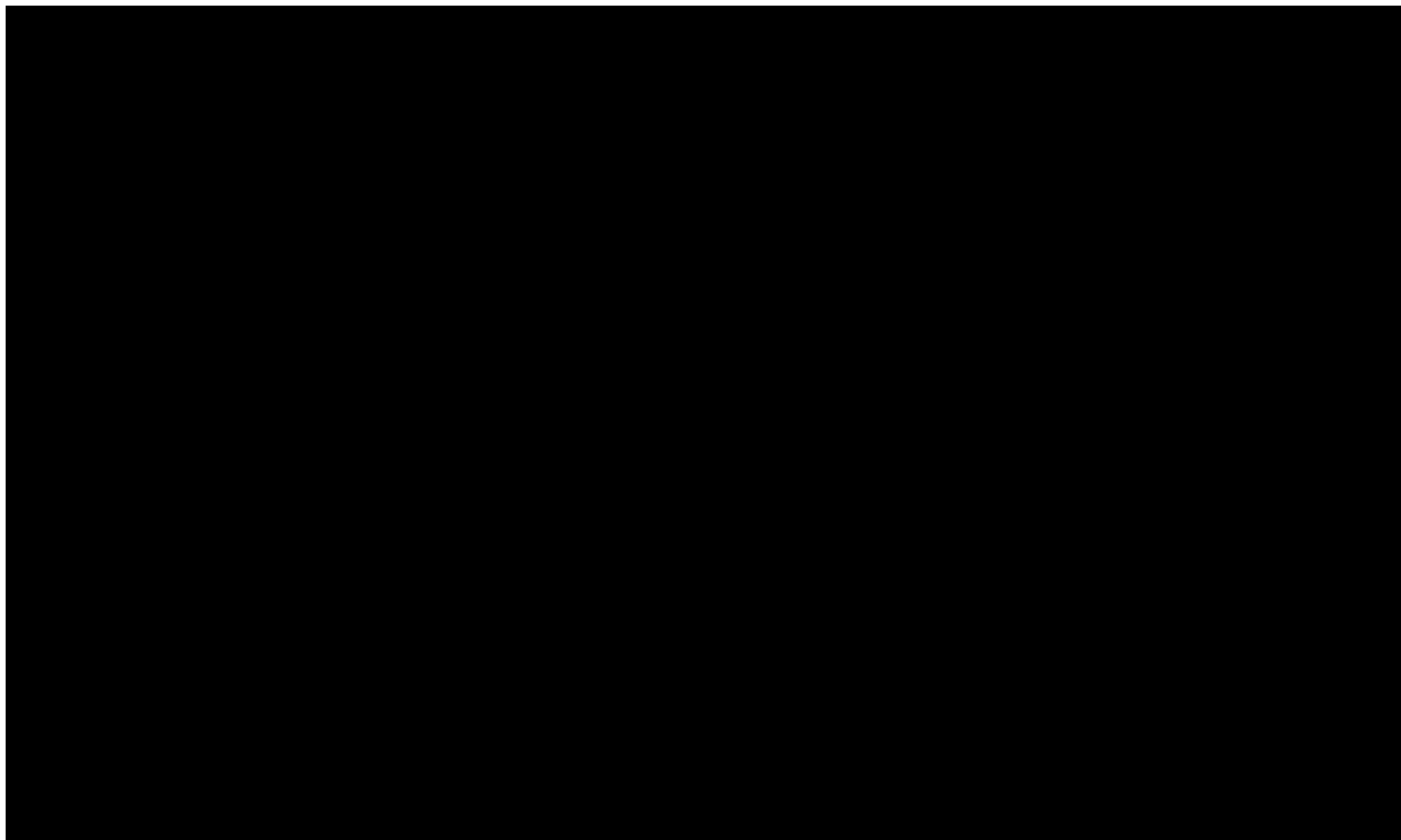
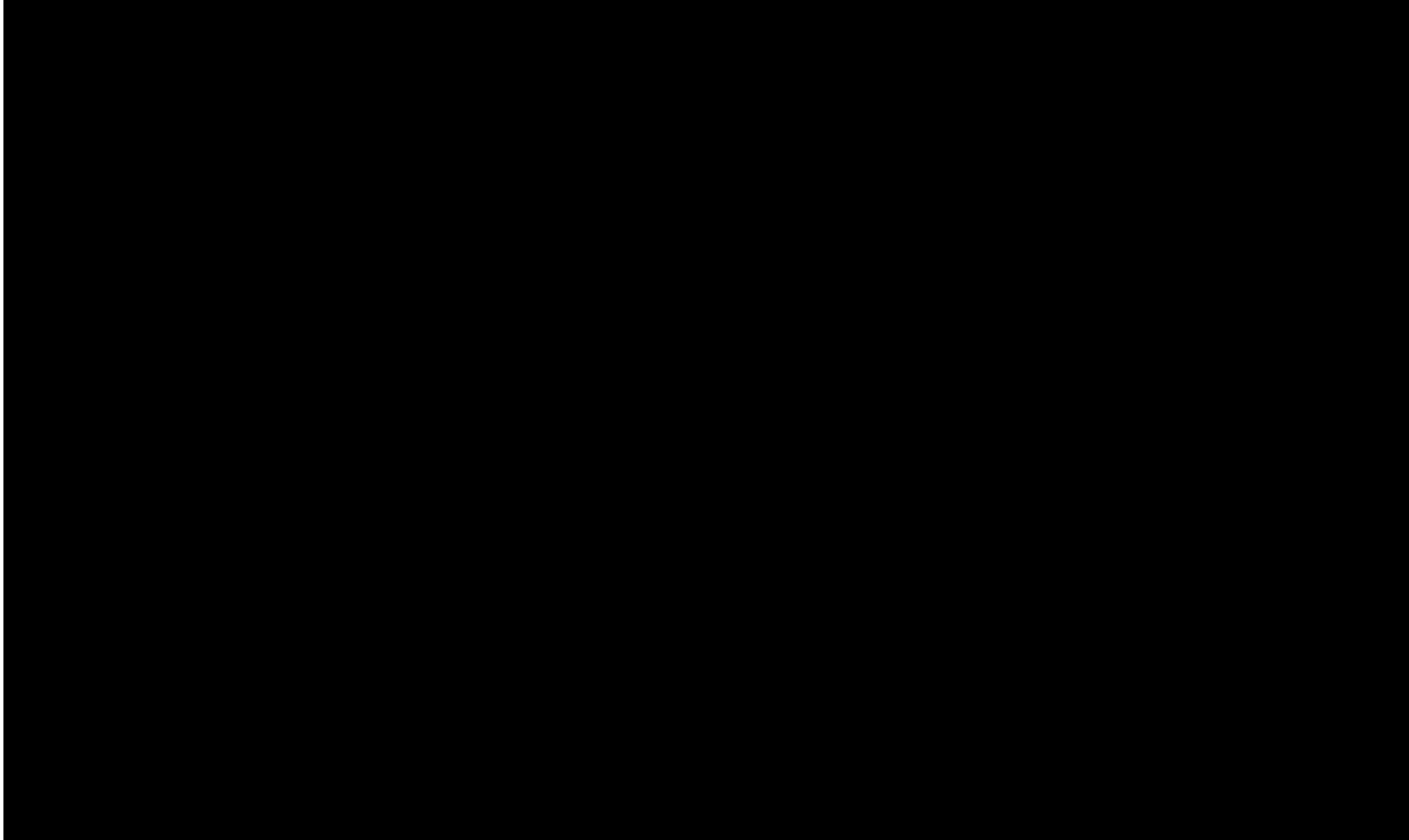
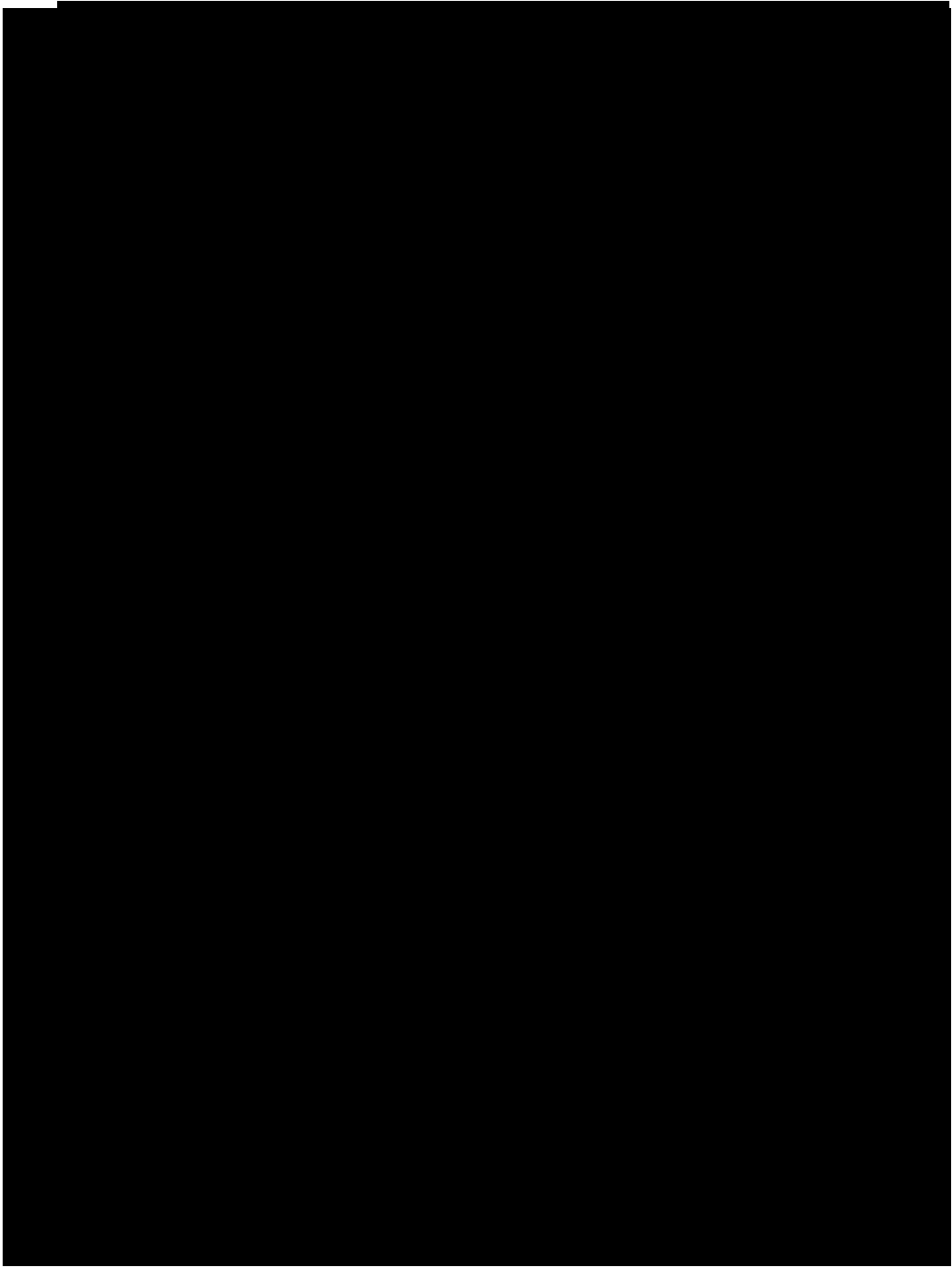


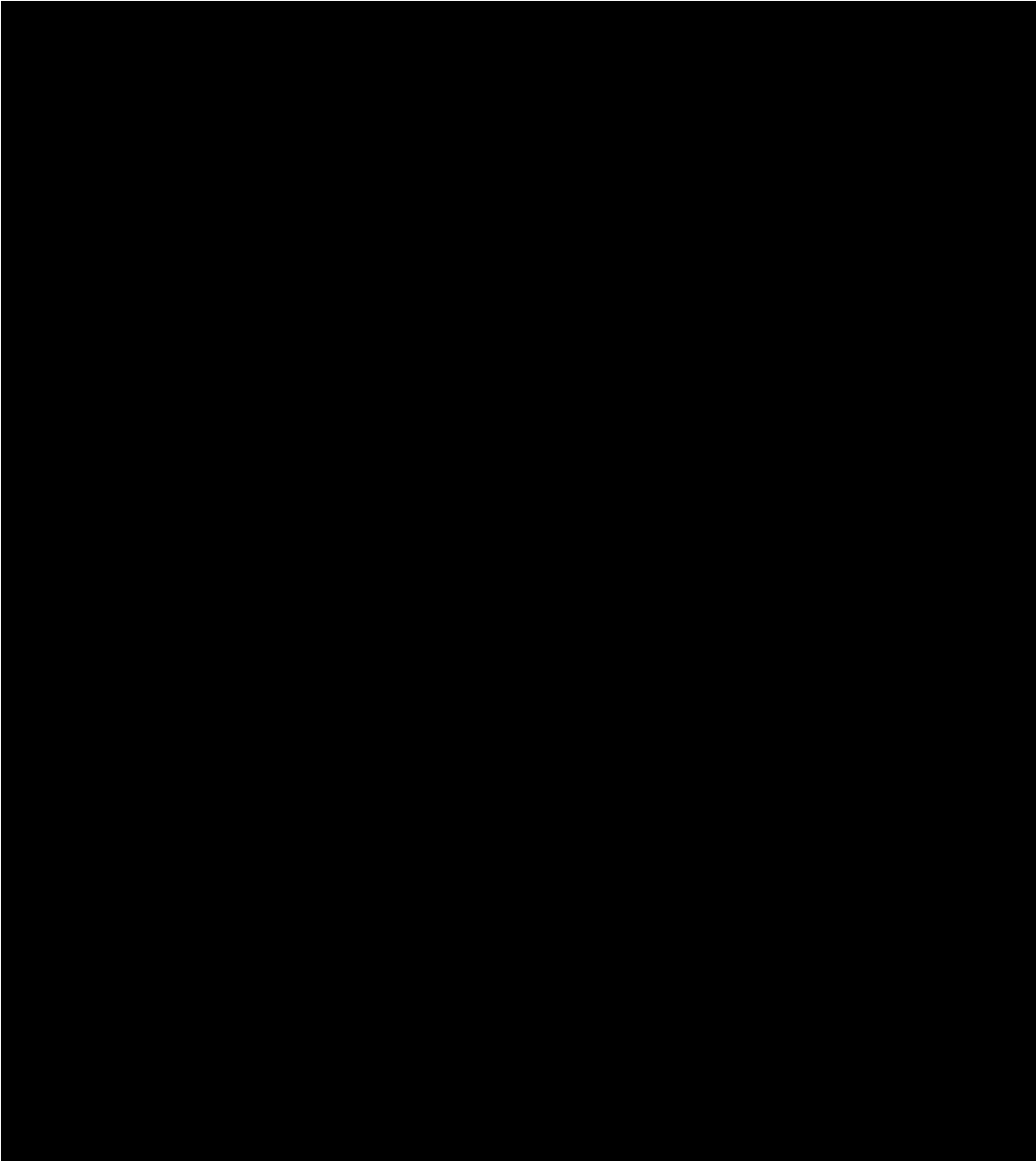
Figure 4.5: DSC thermograms of resins samples PVA 23-88 (A), PVA 13-88 (B) XXXXXXXXXX (C) recorded from -70 to 100°C with scanning rate of 10 °C/min, after different water additions, indicated by the labels. Measurements are performed on independent samples after storing them overnight at room temperature in sealed vials. The amount of added water per 100 parts of PVA ( $m_w/m_{PVA}$ %) is indicated close to each curve.

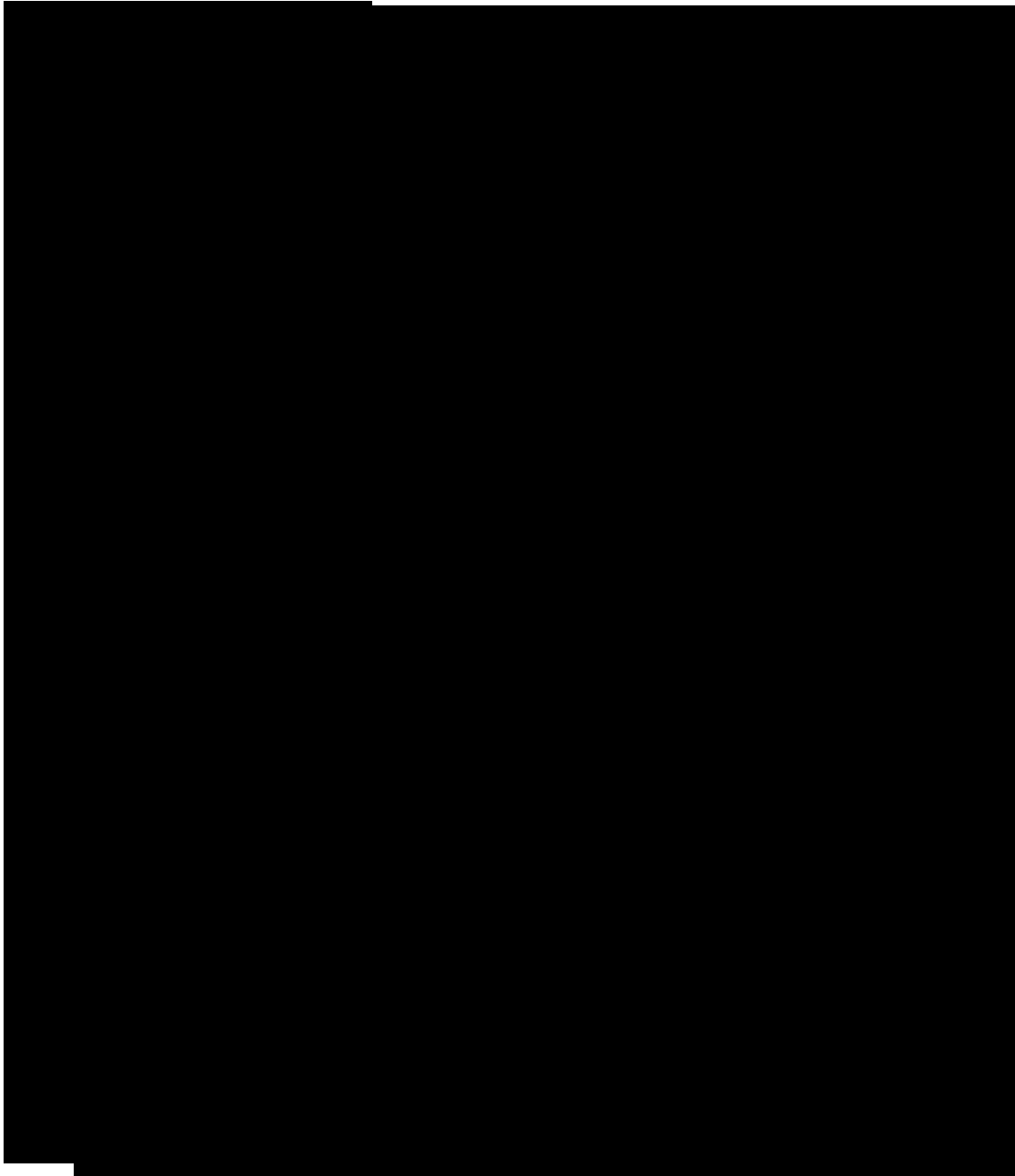


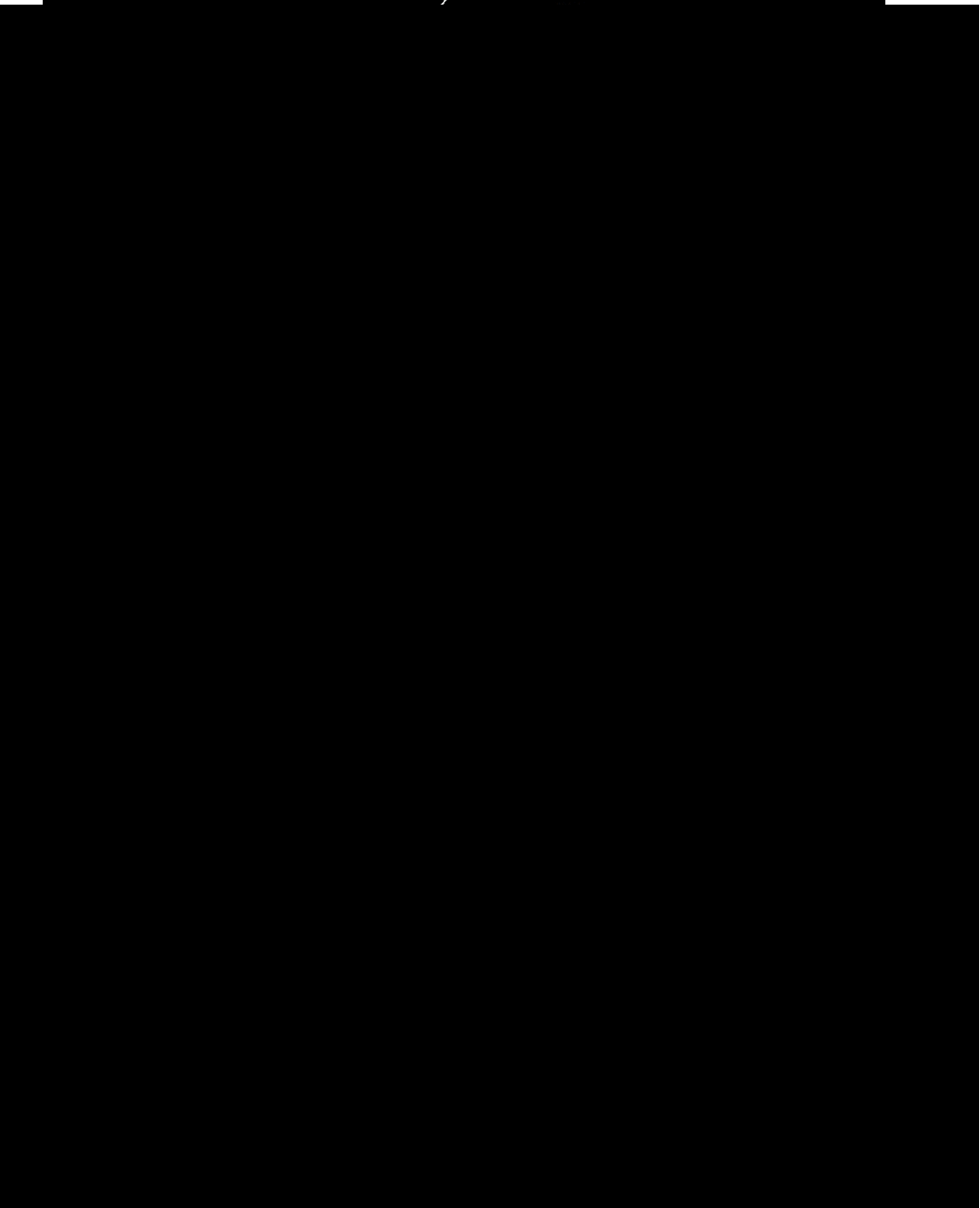












## 4.2.2 Effect of water on PVA structure: SAXS/WAXS analysis

Small-angle X-ray scattering (SAXS) probes relatively large-scale structures, in contrast to wide-angle X-ray scattering (WAXS) that deals mainly with the structure of crystals at atomic length scale. The simultaneous SAXS and WAXS techniques were used to investigate the effect of the water absorption on the structure of PVA [REDACTED]

[REDACTED] obtained from aqueous solution of pure PVA resins samples by casting were analyzed.

Data were collected on dry samples and after water addition, in a specific closed sample holder. In Figure 4.9-A, the desmeared SAXS curves of pure PVA sample 23-88 and 13-88 show, after an upturn in the low  $q$  region, a shoulder at  $q \approx 0.8 \text{ nm}^{-1}$ , followed by a long tail in the high  $q$  [REDACTED]

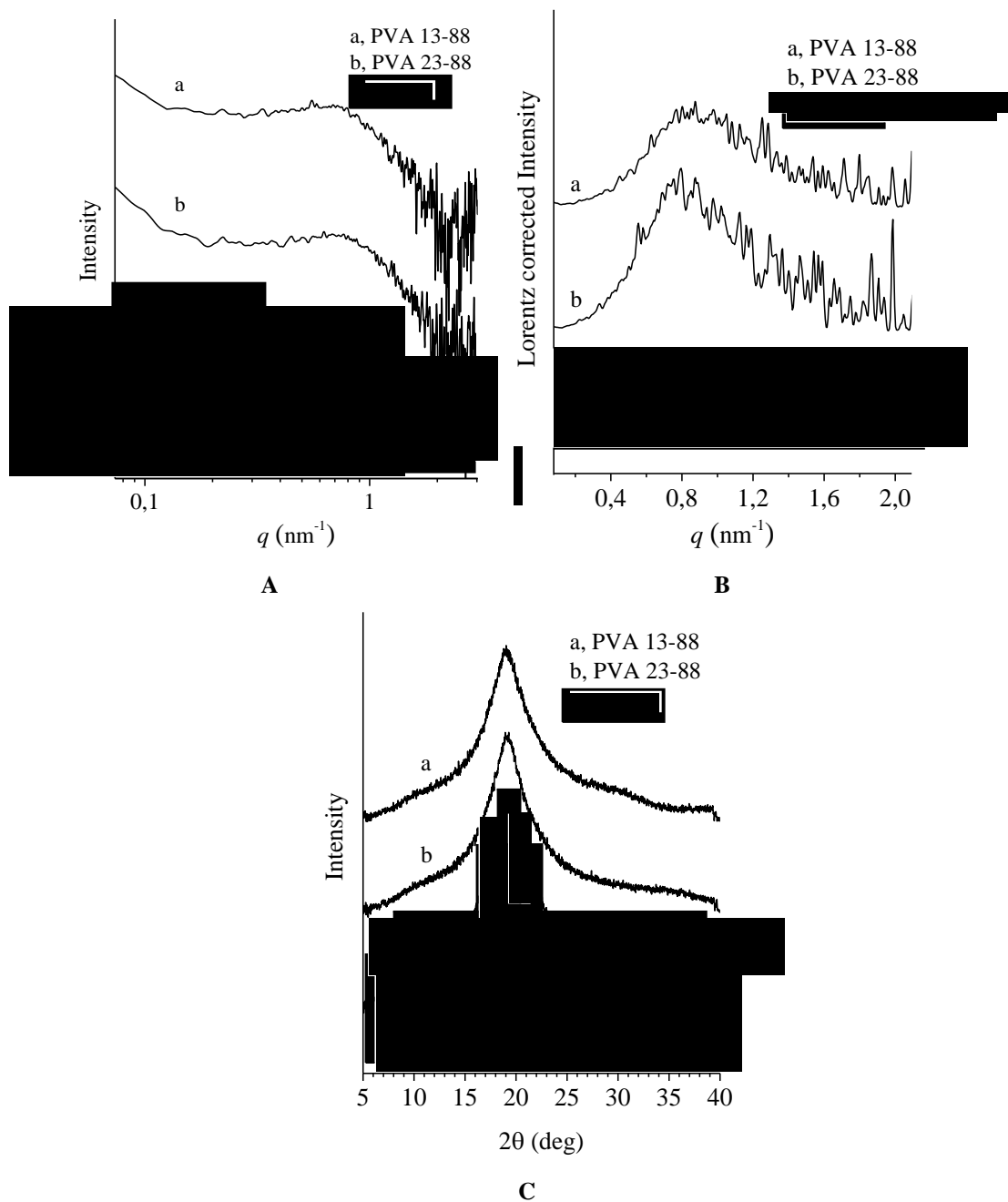
[REDACTED] After correction for the Lorentz factor, the SAXS profiles of the sample PVA 23-88 and PVA 13-88 show a broad correlation peak at  $q \approx 0.8 \text{ nm}^{-1}$  [REDACTED]

[REDACTED] Upon the addition of water to PVA, corresponding to  $(m_w/m_{PVA})\% = 300 \text{ wt}\%$  (with  $m_w$  the mass of added water and  $m_{PVA}$  the mass of the dry film), the correlation peak disappears in the case of PVA 23-88 and PVA 13-88 (Figure 4.10-B, 4.11-B). The WAXS profiles recorded simultaneously in the SAXS apparatus (Figure 4.10-C, 4.11-C) reveal that before addition of water the samples are crystalline, whereas after water addition, the samples become amorphous. This indicates that water above a threshold concentration, dissolves crystals and induces the formation of an amorphous gel where cross-links consist of entanglements or negligible

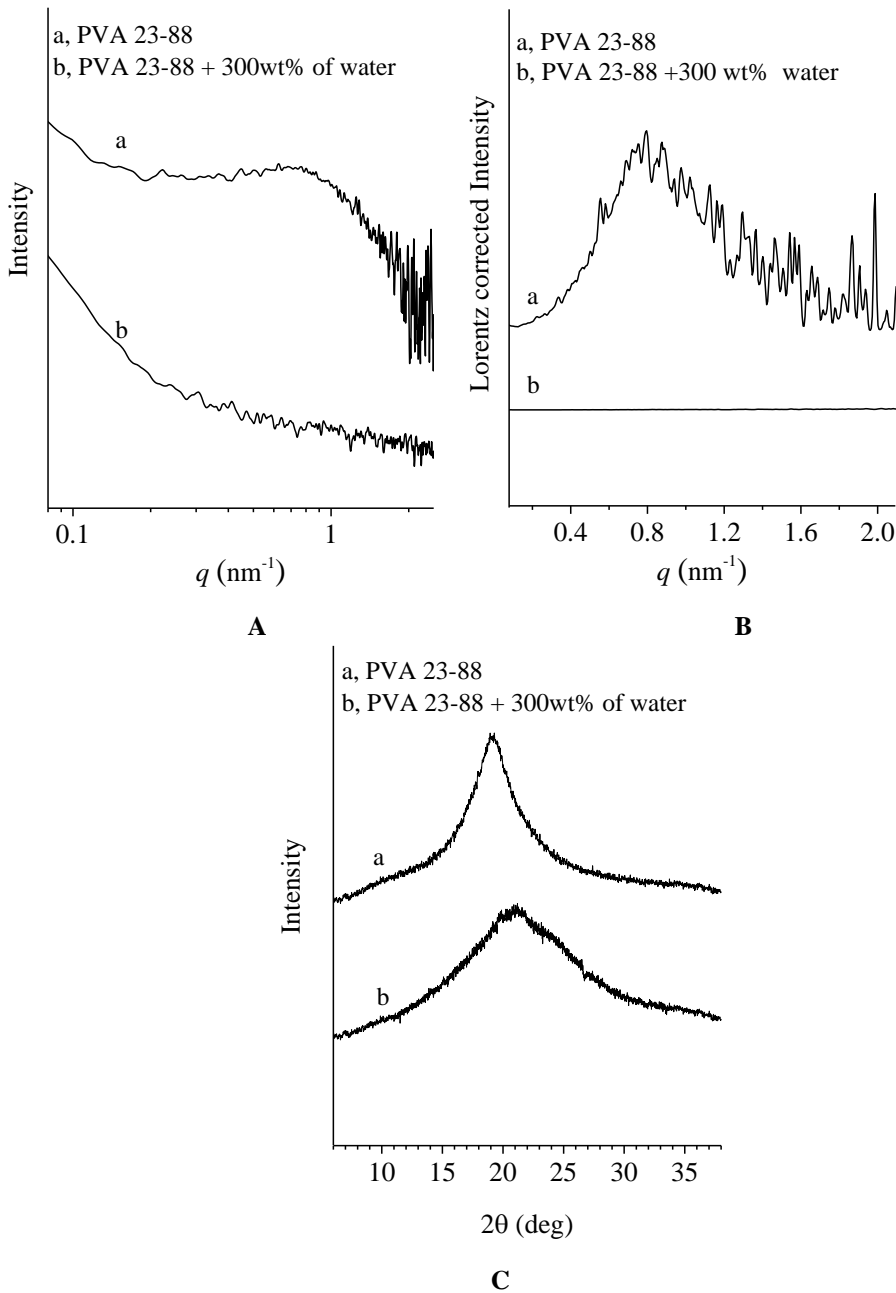
amount of small crystals not dissolved by water. Moreover, the absence of any correlation peak in the SAXS profiles of the crystalline sample PVA A (Figure 4.9, c), even if it is in anhydrous conditions, indicates that the lamellar crystals are isolated. In the case of the dry sample PVA 23-88 and PVA 13-88, instead, the presence of the correlation peak in the SAXS profiles is the hallmark that the lamellar crystals are organized in stacks. More in details, the system can be described as consisting in the alternation of lamellar crystals of thickness,  $l_c$ , and amorphous layers of thickness,  $l_a$ , following each other with periodicity (long spacing),  $L = l_c + l_a$ . The value of long spacing  $L$  may be roughly calculated using the Bragg law:

$$L^* = \frac{2\pi}{q_{\max}^*} \quad \text{eq.4.28}$$

where  $L^*$  is the long spacing value, resulting from rough evaluation of  $q_{\max}^*$ , which is the position of the maximum extracted from the profiles corrected by the Lorentz factor.

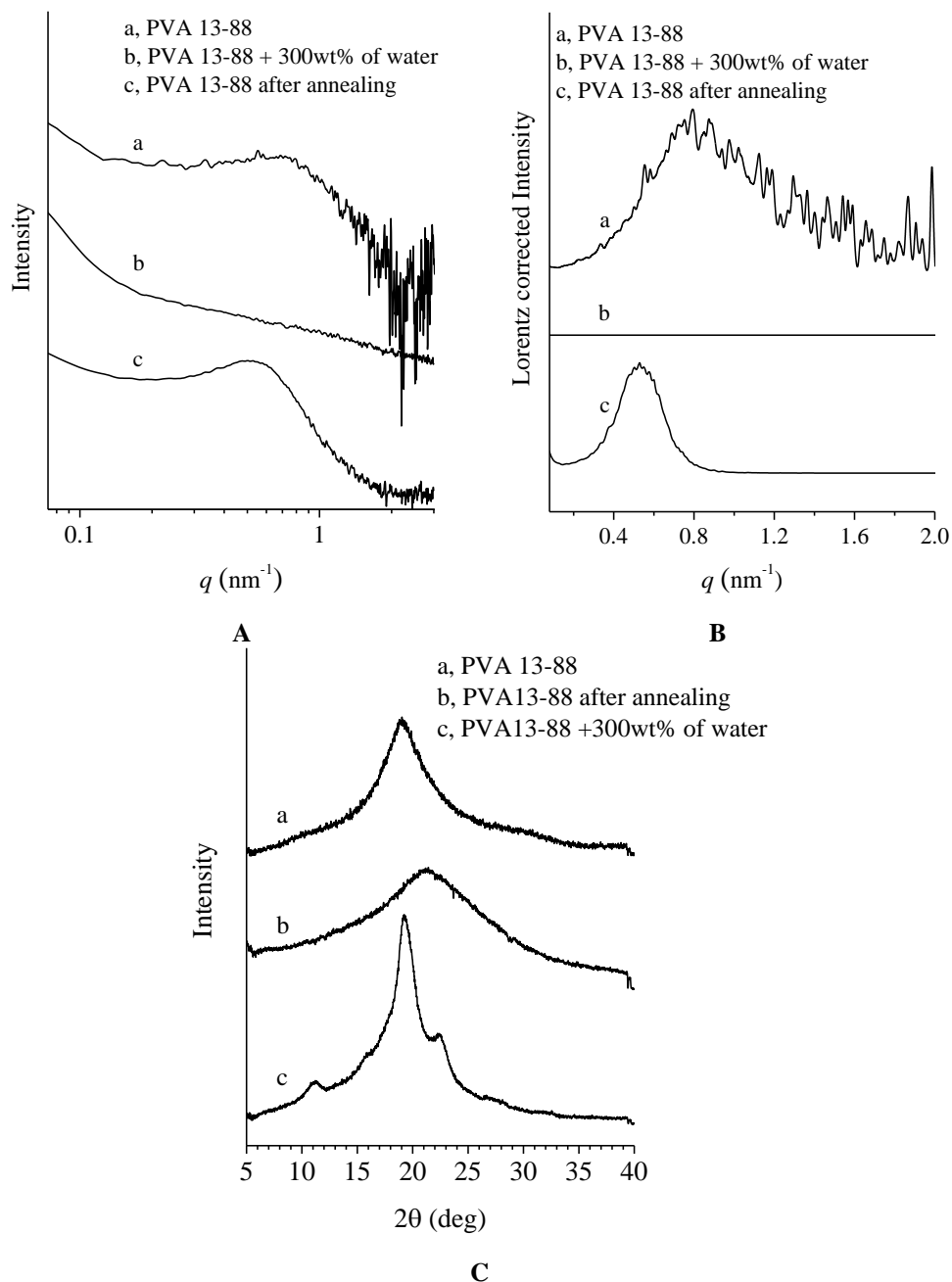


**Figure 4.9:** Desmeared SAXS profiles before (A) and after (B) Lorentz correction and WAXS profiles (C) of the films obtained by casting water solution of sample PVA 23-88 (a), PVA 13-88 (b) and [redacted] recorded at room temperature.



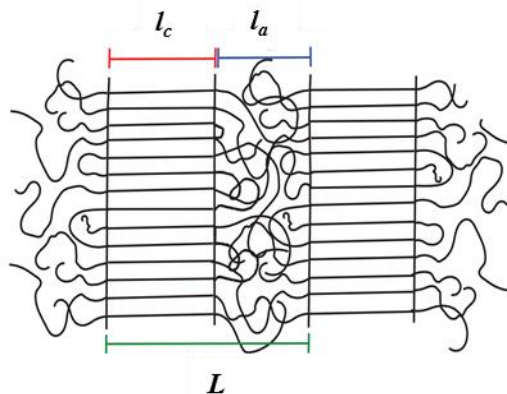
**Figure 4.10:** Desmeared SAXS profiles before (A) and after (B) Lorentz correction and WAXS profiles (C) of the film obtained by casting water solution of sample PVA 23-88. Data are recorded, at room temperature, for the dry film (a) and after hydration (b), by adding a water amount,  $m_w$ , 3 times higher than the mass of the dry PVA film,  $m_{\text{PVA}}$  ( $m_w/m_{\text{PVA}}\% = 300\text{wt}\%$ ).





**Figure 4.11:** Desmeared SAXS profiles before (A) and after (B) Lorentz correction and WAXS profiles (C) of the film obtained by casting water solution of sample PVA 23-88. Data are recorded, at room temperature, for the dry film (a) and after hydration (b), by adding a water amount,  $m_w$ , 3 times higher than the mass of the dry PVA film,  $m_{\text{PVA}}$  ( $m_w/m_{\text{PVA}}$ )

$m_{PVA})\% = 300\text{wt}\%$ ) and for the annealed film (c) kept at  $170^\circ\text{C}$  for 10 min.



**Figure 4.12: Model of lamellar stacks of a semicrystalline polymer, where the lamellae of thickness  $l_c$  are alternated to amorphous layers of thickness  $l_a$ . The long spacing,  $L$ , is the sum  $l_c + l_a$ . Adapted from [37].**

A schematic representation of the model of lamellar stacks is drawn in Figure 4.12. Analyses on the film obtained by casting water solution of the sample PVA 13-88, after a specific thermal annealing treatment, have given further evidence for the crystalline nature of the correlation peak in the SAXS curve. The cast film of sample PVA 13-88 was kept at  $170^\circ\text{C}$  for 10 minutes and then analyzed at room temperature (Figure 4.11, c). As a result of the annealing treatment, an improvement of the crystallinity occurs, as indicated by the WAXS profile of Figure 4.11. Moreover, the correlation peak in the SAXS profile of Figure 4.11-A, B (curves c), becomes better defined while shifting toward lower  $q$  values. This indicates that the long spacing increases. From the value of  $L^*$ , evaluated from the maximum of the Lorentz corrected SAXS intensity, the values of the lamellar thickness,  $l_c^*$  and of the thickness of the amorphous layers,  $l_a^*$ , can be calculated, using the Bragg law, as:

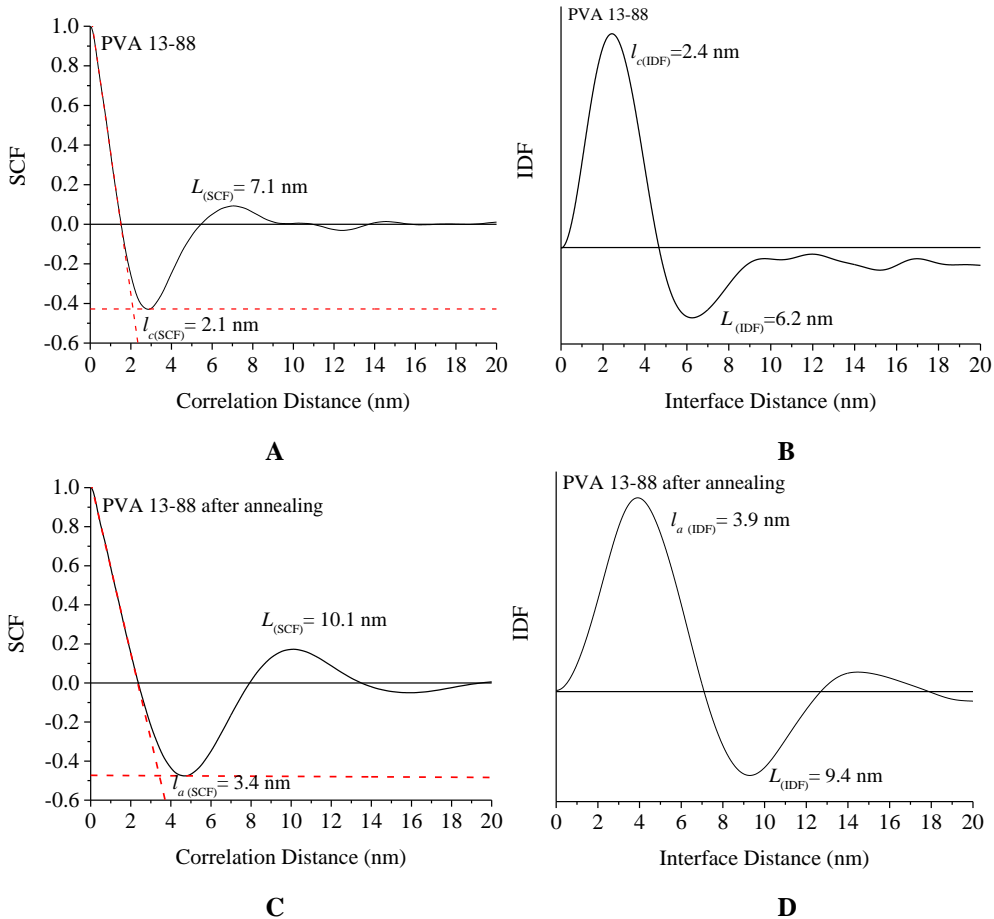
$$l_c^* = L^* \cdot x_{c(\text{WAXS})} \quad \text{eq. 4.29}$$

$$l_a^* = L^* - l_c^* \quad \text{eq. 4.30}$$

where  $x_{c(\text{WAXS})}$  is the crystallinity index evaluated from WAXS data of Figure 4.11. Assuming the lamellar stacks morphology (Figure 4.12), the values of the lamellar parameters ( $L$ ,  $l_a$ ,  $l_c$ ) can be also evaluated resorting to the calculation of the interface distribution function IDF and the self-correlation function of electron density fluctuation SCF (or  $K(z)$ , as indicated in Chapter 2), and reported in Figure 4.13.

The values of the morphological parameters found by the Lorentz corrected SAXS profiles ( $L^*$ ,  $l_a^*$ ,  $l_c^*$ ), by the self-correlation functions SCF ( $l_{c(\text{SCF})}$ ,  $l_{a(\text{SCF})}$ ,  $L_{(\text{SCF})}$ ) and by the intensity distribution function IDF ( $l_{c(\text{IDF})}$ ,  $l_{a(\text{IDF})}$ ,  $L_{(\text{IDF})}$ ) are reported in Table 4.2. Moreover, the ratio  $l_{c(\text{SCF})}/L_{(\text{SCF})}$  and  $l_{c(\text{IDF})}/L_{(\text{IDF})}$ , which are indicative of the crystallinity, are calculated before and after annealing and are also reported in Table 4.2.

It is apparent that by effect of annealing, the long period  $L$  increase, and this increase is due to the increase of lamellar thickness,  $l_c$ , in agreement with the sharpening of Bragg reflection in the WAXS profiles of Figure 4.11c. Coherently, upon the annealing, the linear crystallinity, evaluated as  $l_{c(\text{SCF})}/L_{(\text{SCF})}$  and  $l_{c(\text{IDF})}/L_{(\text{IDF})}$ , from SCF and IDF, respectively, also increase in agreement with increase of the crystallinity index  $x_{c(\text{WAXS})}$  extracted from WAXS data (Table 4.2). The differences between the values of lamellar parameters extracted through the different methods is due to the presence of large amount of disorder in the lamellar stacking arrangement of PVA crystals (Figure 4.12), entailing a wide distribution of lamellar thickness and thickness of the amorphous layers, typical of semicrystalline copolymers. Moreover, the higher values of linear crystallinity values  $l_c/L$  extracted from SAXS analysis with respect to those of the crystallinity index  $x_{c(\text{WAXS})}$  extracted from WAXS, indicate that part of amorphous phase is located outside of the lamellar stacks, and confined at boundary regions.



**Figure 4.13:** Self-correlation function (SCF) (A, C) and interface distribution function (IDF), calculated from the desmeared profiles of a film obtained by casting water solution of the sample PVA 13-88 before (A, B) and after (C, D) annealing treatment at 170°C for 10 minutes. The main correlation triangle at the origin is shown (A, C). The evaluated values of  $L$  and  $l_c$  and  $l_a$  are indicated.

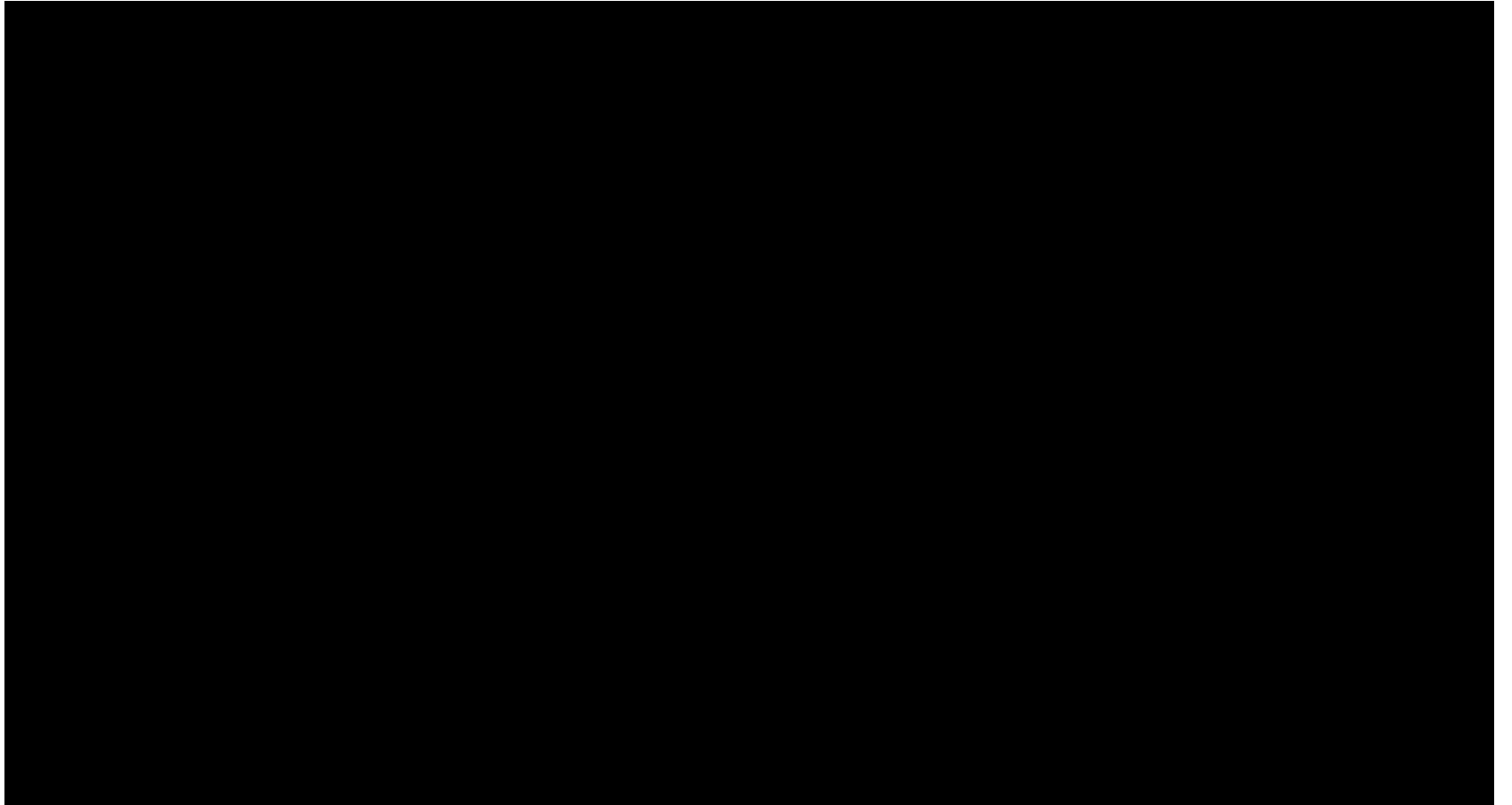
**Table 4.2:** Morphological parameters evaluated from the analysis of the SAXS profiles recorded at room temperature for films obtained by solution casting for the sample PVA 13-88 before and after annealing treatment at 170°C for 10 minutes. The values of the long spacing ( $L$ ), thickness of the crystalline lamellae ( $l_c$ ) and of the amorphous layers ( $l_a$ ) evaluated from the Lorentz-corrected profiles ( $L^*$ ,  $l_c^*$ ,  $l_a^*$ ), from the self-correlation function, SCF, ( $l_{c(SCF)}$ ,  $l_{a(SCF)}$ ,  $L_{(SCF)}$ ,  $l_{c(SCF)}/L_{(SCF)}$ ) and from the intensity distribution

function, IDF ( $l_{c(\text{IDF})}$ ,  $l_{a(\text{IDF})}$ ,  $L_{(\text{IDF})}$ ,  $l_{c(\text{IDF})}/L_{(\text{IDF})}$ ) are reported. The crystallinity index,  $x_{c(\text{WAXS})}$ , extracted from WAXS profiles is also reported.

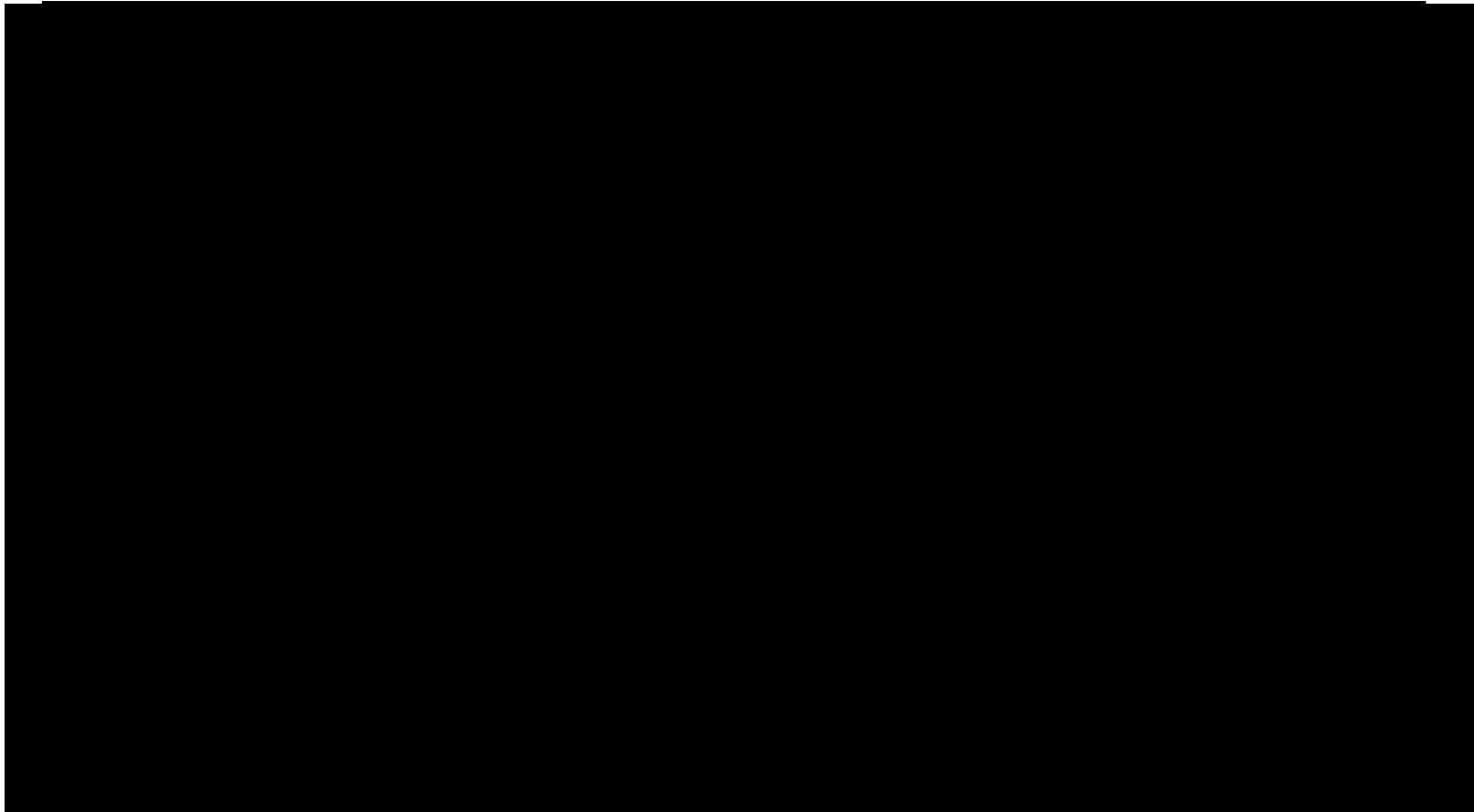
		PVA 13-88	PVA 13-88 annealed
Lorentz	$L^*$ (nm)	7.8	11.8
	$l_c^*$ (nm)	3.0	6.0
	$l_a^*$ (nm)	4.8	5.8
	$x_{c(\text{WAXS})}$ (%)	39	51
SCF	$L_{(\text{SCF})}$ (nm)	7.1	10.1
	$l_{c(\text{SCF})}$ (nm)	2.1	6.7
	$l_{a(\text{SCF})}$ (nm)	5.3	3.4
	$l_{c(\text{SCF})}/L_{(\text{SCF})}$ (%)	30	65
IDF	$L_{(\text{IDF})}$ (nm)	6.2	9.4
	$l_{c(\text{IDF})}$ (nm)	2.4	5.3
	$l_{a(\text{IDF})}$ (nm)	3.8	3.9
	$l_{c(\text{IDF})}/L_{(\text{IDF})}$ (%)	39	56

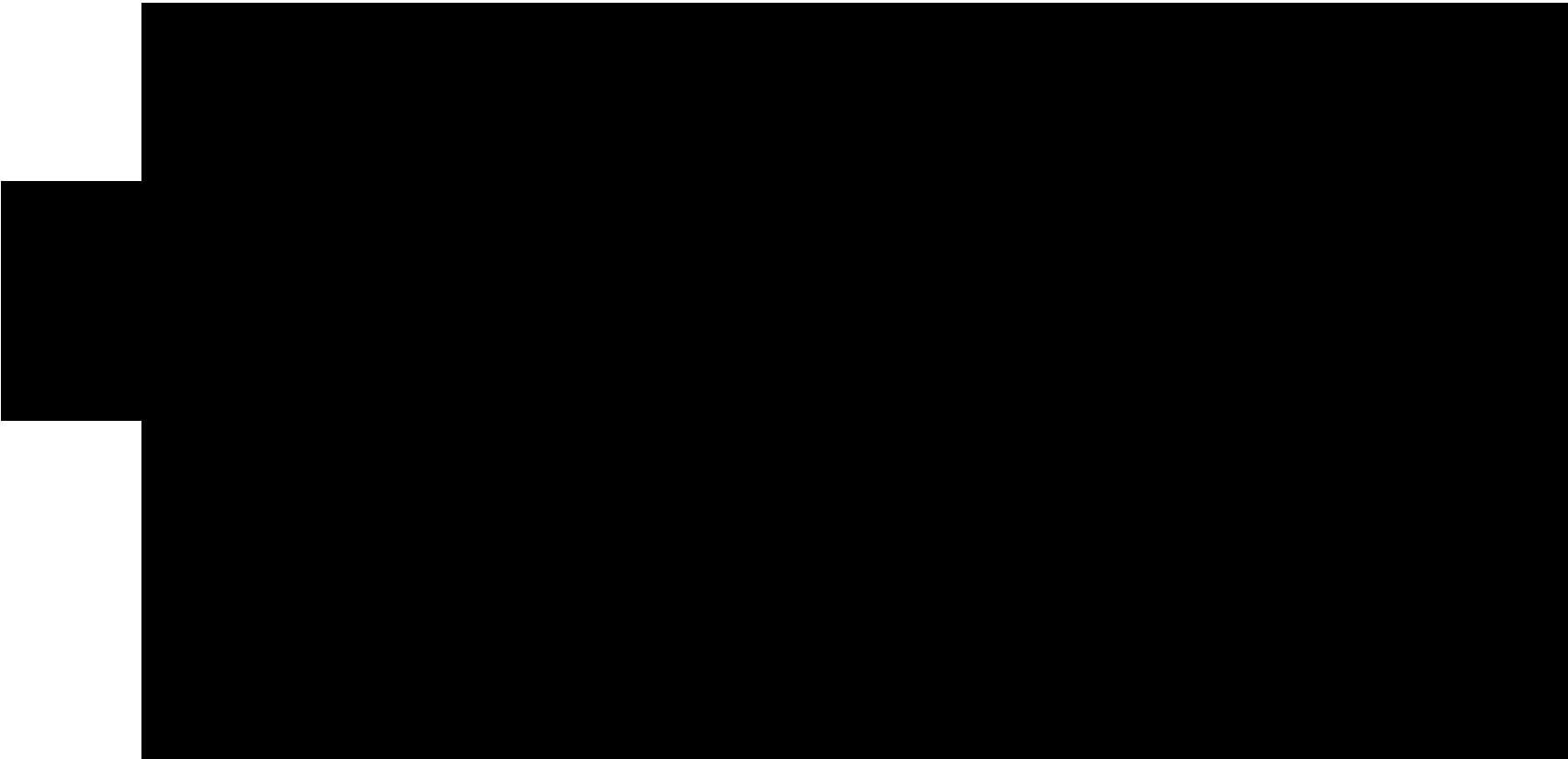


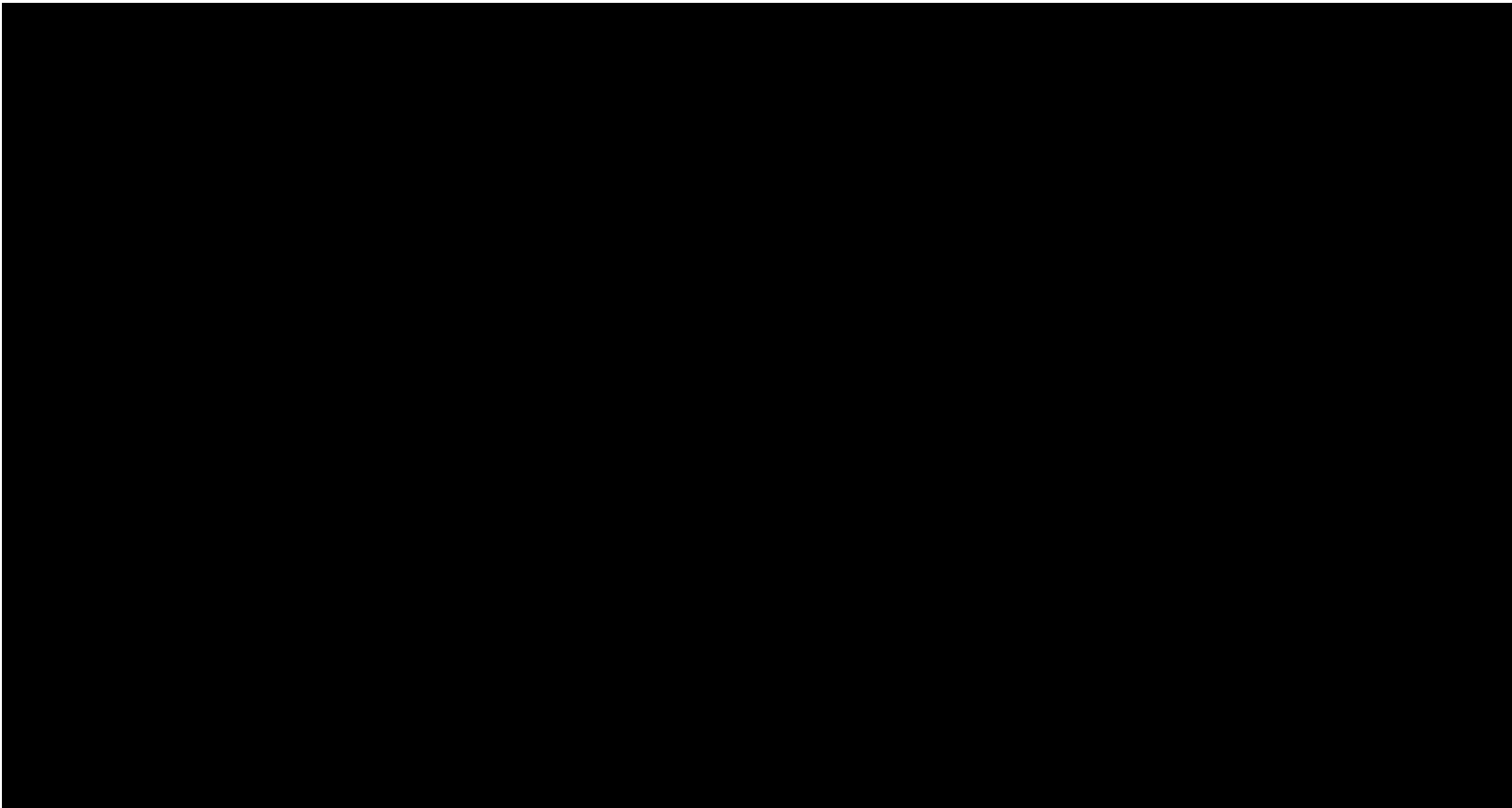















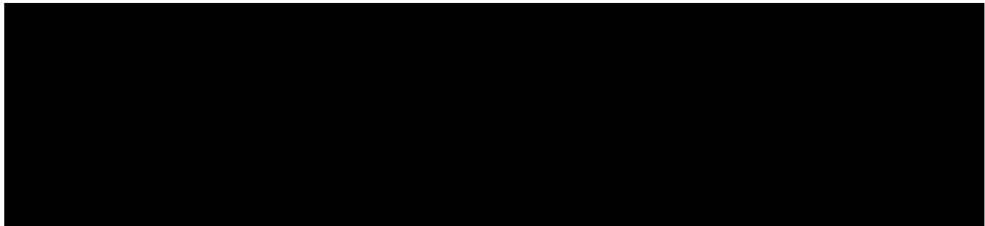
### 4.2.3 Re-crystallization kinetics

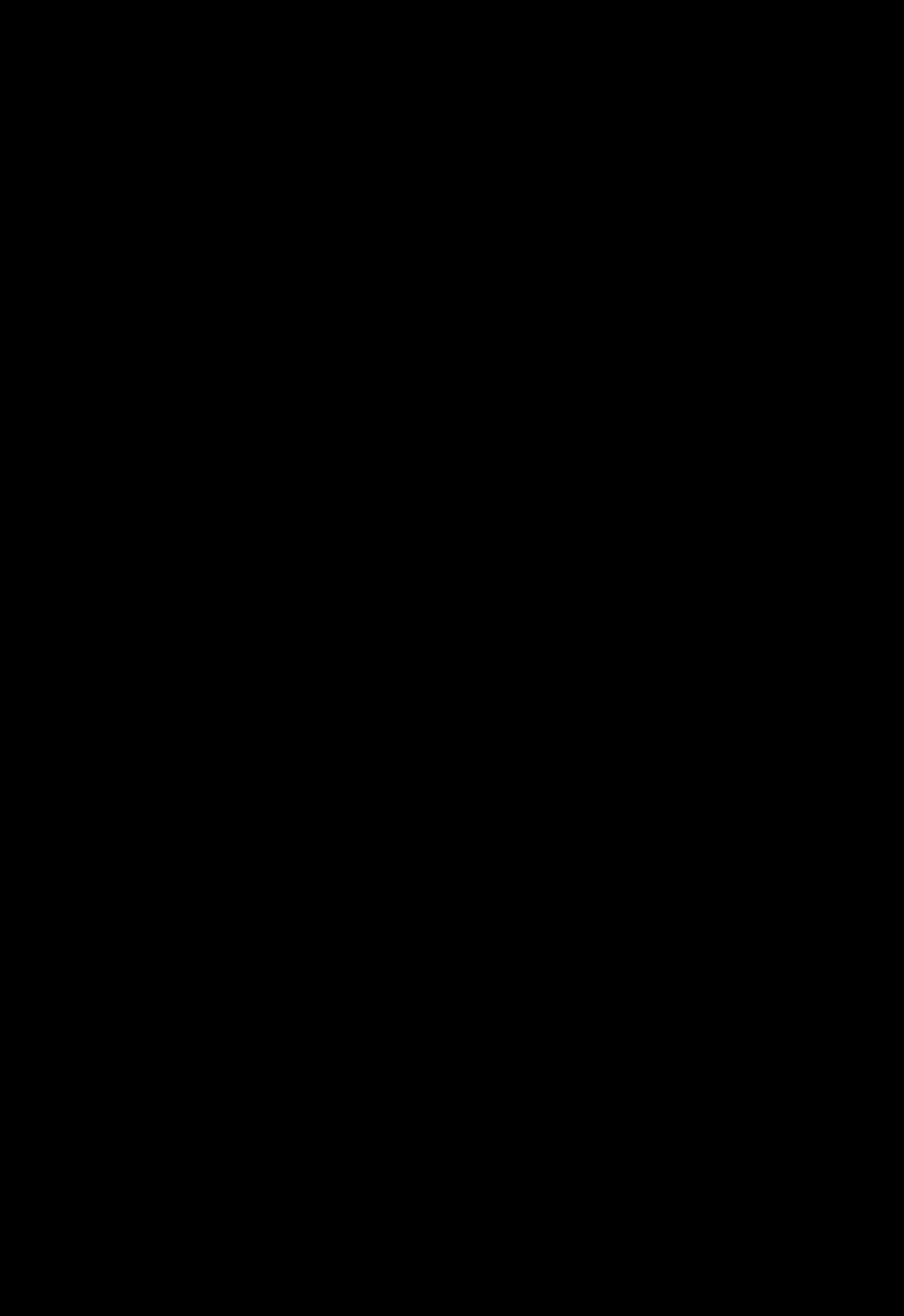
The effect of water addition on the structure of PVA films is followed, in more detail, resorting to WAXS analysis. This is illustrated in  where the WAXS profiles, recorded after additions of increasing amounts of water, are reported.  intensity of the (10 $\bar{1}$ ) reflection of PVA decreases by addition of water up to  $(m_w/m_{PVA})\% \approx 175\text{-}200\text{wt}\%$ .

The angular position of the (10 $\bar{1}$ ) reflection and, thus, the interplanar spacing is quite unaltered by water addition, indicating that water does not influence the crystal structure of PVA. The added water rather acts dissolving the crystals. Therefore, PVA crystals undergo dissolution by addition of water already at room temperature, albeit they melt at high temperature ( $\approx 180^\circ\text{C}$ ). The dissolution process is fast. Indeed, the diffraction profiles of  are recorded immediately after addition of the indicated quantity of water, and each measurement is performed in less than 10 min.

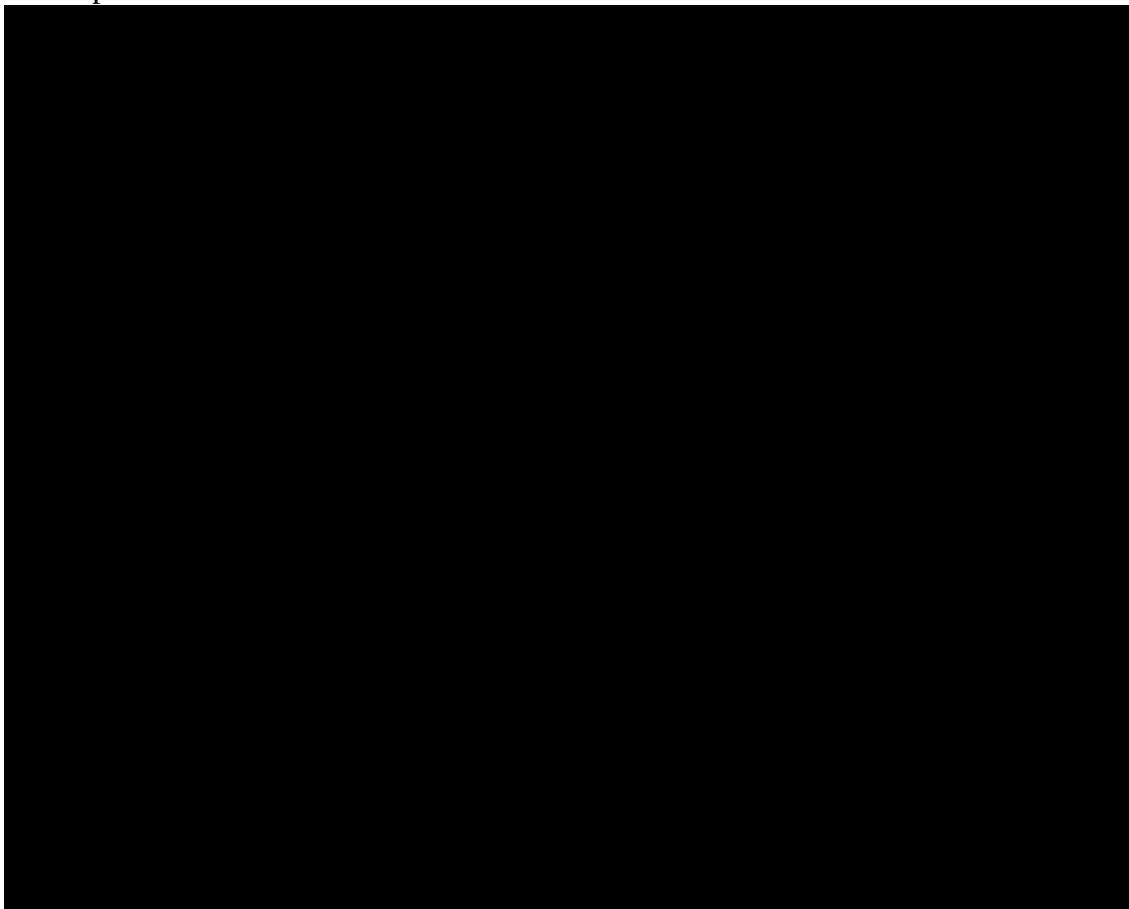
This suggests that the welding mechanism occurring at room temperature is controlled by water absorption. Indeed, the water diffused in the polymeric matrix is able to increase the mobility of chains and to dissolve the crystals. Afterward, the second essential process to take into account is the re-crystallization of PVA by water desorption. Hence, the interrogatives are: 1) after water evaporation, does crystallization in PVA films take place again? 2) if it does, after amorphization by addition of water, how long does this new crystallization need to take place?

The kinetics of the re-crystallization and of the simultaneous loss of water (desorption kinetics) were investigated, to determine the involved times of the re-crystallization process and the relationship with the water evaporation.



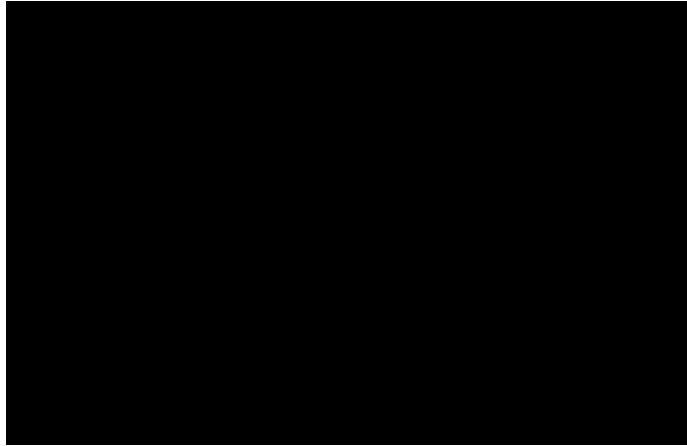


Two layers of PVA films were sealed by adding an amount of water large enough to melt the entire system, corresponding to  $(m_w/m_{PVA}) = 140\text{wt}\%$ , that is 58wt% of water over the total,  $m_w/(m_{PVA}+m_w)$ . WAXS data were recorded every 10-15 minutes to follow the crystallization (Figure 4.19). The loss of water with time was evaluated by gravimetry, as shown in Figure 4.20, on an independent set of samples, after addition of the same amount of water used for recording WAXS data. The temperature was kept at 25°C in these experiments.



The increase of intensity of the diffraction peak at  $2\theta=19.4^\circ$  in Figure 4.19, with increase of time, indicates that crystallization/amorphization are reversible processes by effect of water absorption/desorption. The degree of

crystallinity was calculated after subtracting to each profile the diffraction profile of pure water and the amorphous contribution, where the water contribution was scaled taking into account the amount of water contained in the sample at different times. The so-obtained values of crystallinity ( $x_c(t)$ ) were normalized for the maximum value of crystallinity achieved after complete water evaporation,  $x_\infty$ , to obtain the apparent degree of crystallinity  $x'_c(t)=x_c(t)/x_\infty$ , and plotted as a function of time in Figure 4.21. The apparent crystallinity values reach a plateau value in about 3-4 hours for both samples. Also the water desorption is completed within 4 hours (Figure 4.20). The apparent degree of crystallinity,  $x'_c(t)$ , is reported as a function of weight loss, due to water evaporation, in Figure 4.21-B. It is apparent that the maximum value of crystallinity is reached when the evaporation of water is almost complete.



The desorption process of water from the [REDACTED] was analyzed in the framework of Fick second law, in Figure 4.22-A, where the ratio  $M(t)/M_\infty$ , (with  $M(t)$  the mass of water which is desorbed at time,  $t$ , and  $M_\infty$  the mass loss at very long times) is reported as a function of  $t^{1/2}$ .

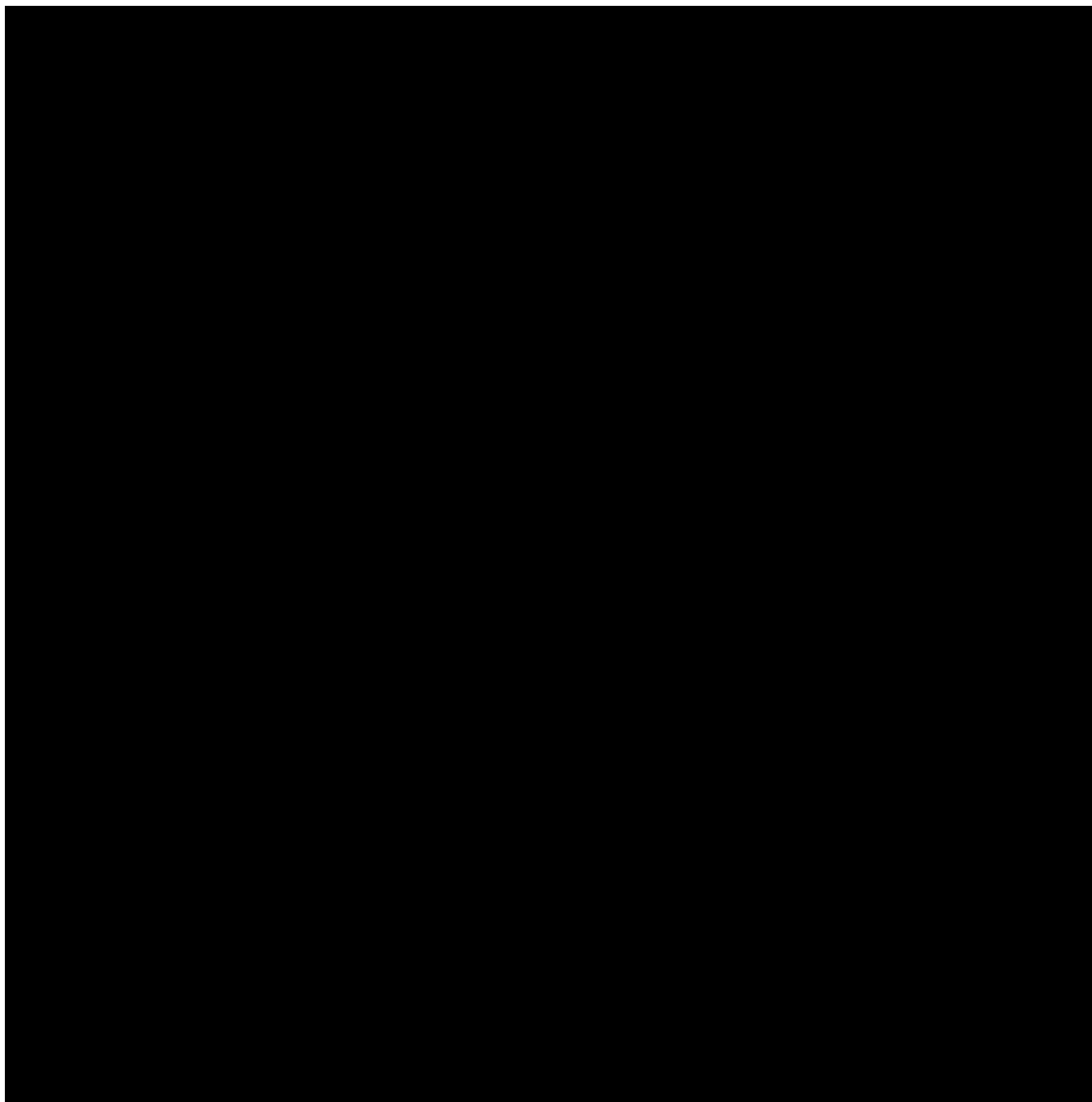
It is apparent that the desorption process of water from our PVA films is non Fickian but is an example of case II model (see section 4.1.5). Indeed, the quantity  $M(t)/M_\infty$  at low times does not increase linearly with  $t^{1/2}$  as the curves present a lag before the beginning of the linear increment. The curves can be fitted to the empirical Weibull function [38], [39], obtaining the rate constant for desorption,  $k_{desorption}$ :

$$\frac{M(t)}{M_\infty} = 1 - \exp(-k_{desorption} \cdot t)^\alpha \quad \text{eq. 4.31}$$

In eq. 4.31,  $\alpha$  is the shape parameter, characteristic for the curve ( $\alpha = 1$  for an exponential function,  $\alpha > 1$  in case of sigmoid with an inflection point and  $\alpha < 1$  describes a curve with a high initial slope followed by an exponential behavior). Even if eq. 4.19 is often used [38]–[41], it represents an empirical approach to describe the kinetics of absorption/desorption of a penetrant in a



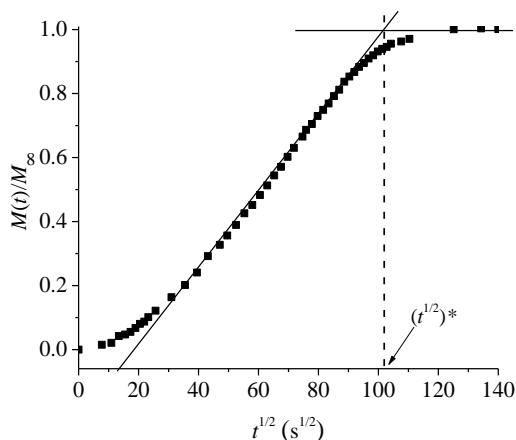
medium, where the parameter  $\alpha$  is of difficult interpretation in terms of a physical model [42].



In an alternative approach, using the same approximation that the diffusion is not a function of the solvent concentration, the apparent diffusion coefficient,  $D^*$ , can be determined using a graphical method. In details, the apparent diffusion can be calculated more directly using the relation:

$$D^* = \left(\frac{\pi}{16}\right) \cdot \left(\frac{l}{(t^{1/2})^*}\right)^2 \quad \text{eq. 4.34}$$

where  $l$  is the thickness of the film, expressed in cm, and  $(t^{1/2})^*$  corresponds to the time at which the linear part of the curve intersects the equilibrium line, as shown in Figure 4.23, as an example. The eq. 4.34 is obtained from the Crank solution of Fick's law, as described in section 4.1.4.



**Figure 4.23:** Graphical method to determine the characteristic value of  $(t^{1/2})^*$ , used to evaluate the apparent diffusion coefficient,  $D^*$ , by eq. 4.34.

The determination of the apparent diffusion coefficient by eq. 4.34 takes into account only the linear part of the curves of Figure 4.22-A, as only the linear part may be considered as Fickian.

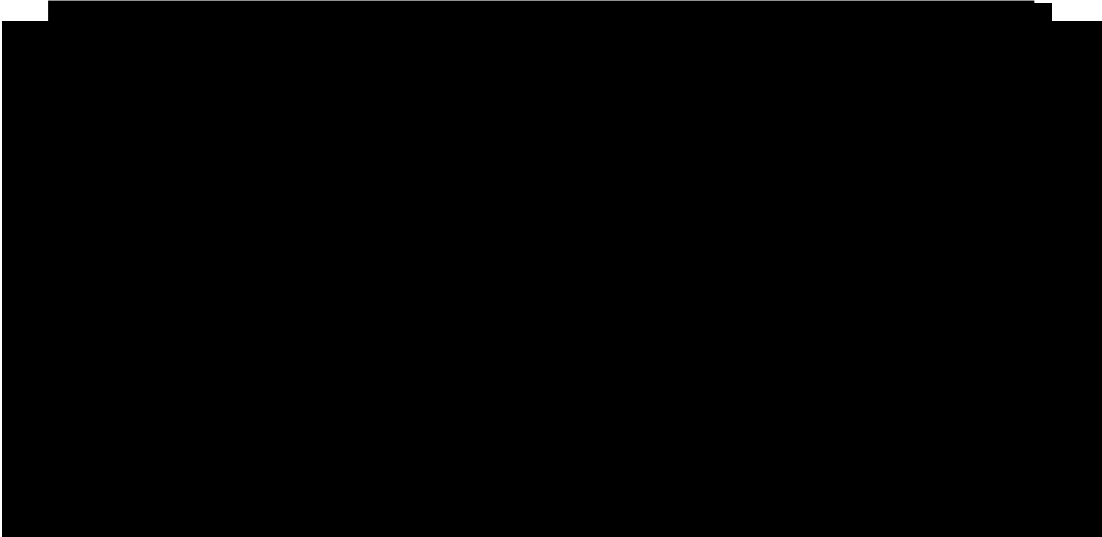
[REDACTED]

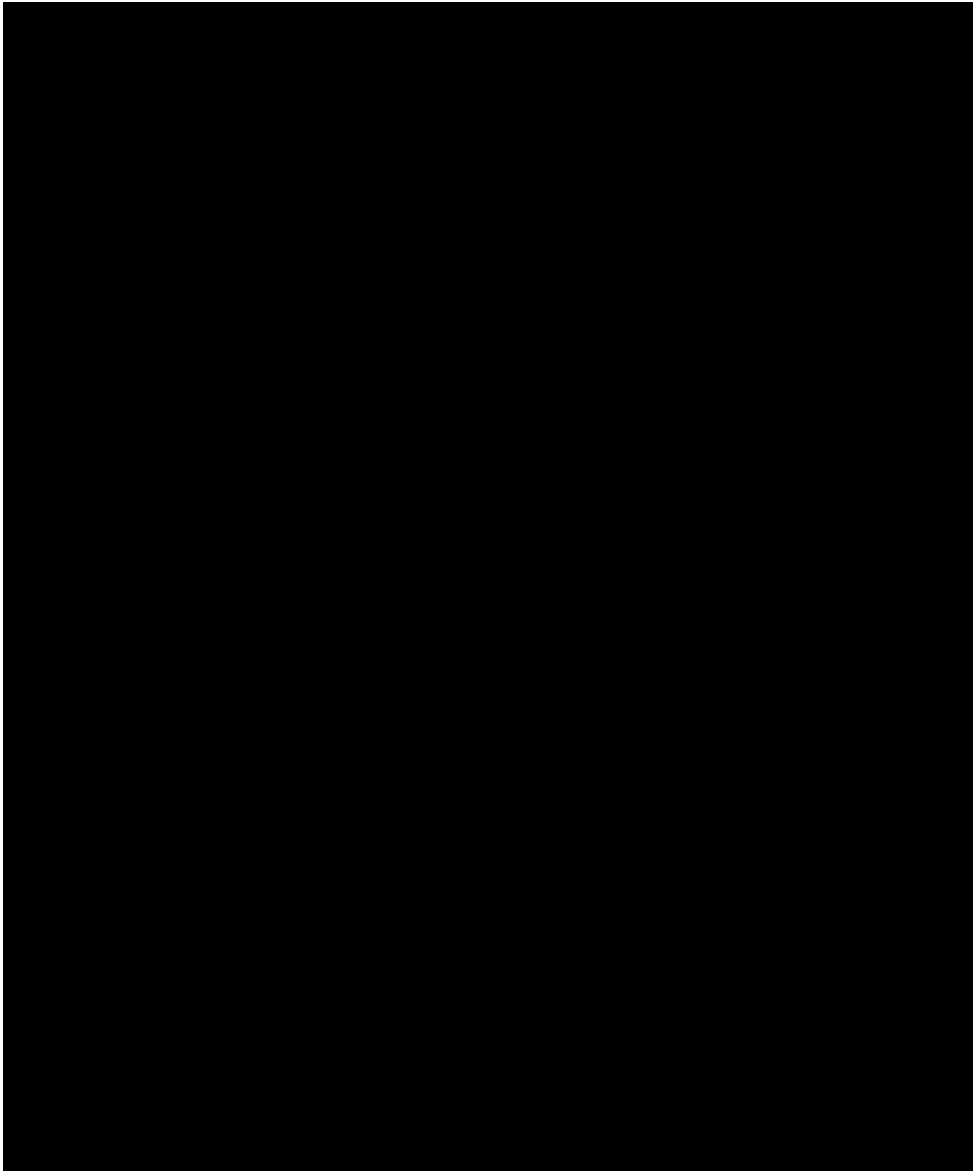
## 4.2.4 Water sorption of PVA films by Dynamic Vapor Sorption (DVS) technique

In order to determine the sorption isotherms and obtain information on the diffusion coefficient of water in PVA based films as a function of water

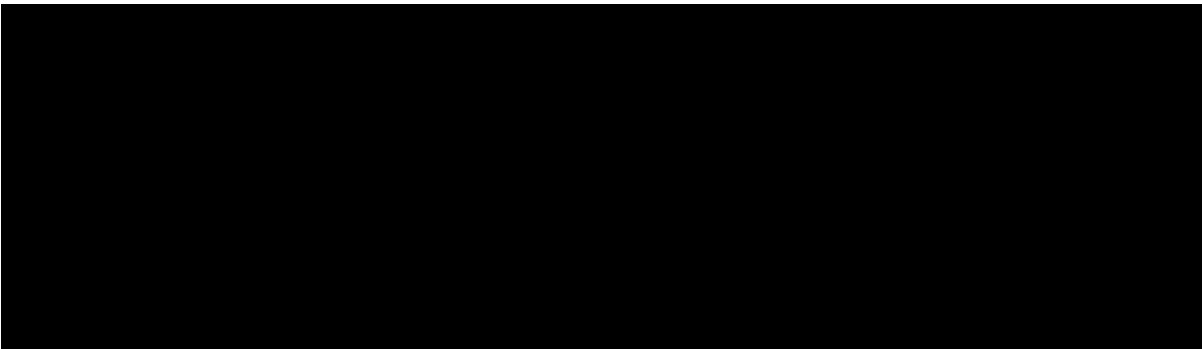
activity, Dynamic Vapor Sorption (DVS) technique has been used. This gravimetric technique measures the change in mass by altering the concentration of vapor surrounding the sample at fixed temperature. Hence, information about the amount and rate of absorption of a solvent by a sample can be obtained.

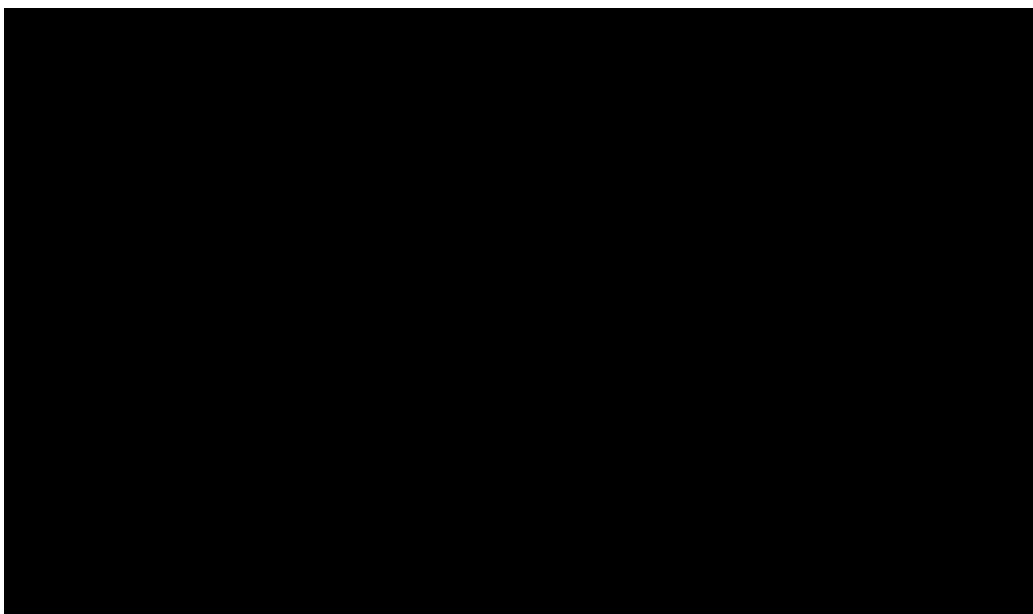
During the experiment the mass change is recorded while the relative humidity (RH) is changed step-wise in a selected range. Sorption measurements are performed increasing the RH value from 10%RH up to 80%RH and then, decreasing the RH value back to 10%RH at steps of  $\Delta$ RH of 10%. The RH is quickly increased/decreased at each step, after waiting for a time long enough to reach a constant mass of the sample, marking the achievement of equilibrium state. All the experiments were performed at 25°C. The typical curves of the mass change of a sample as function of time are reported in Figure 4.24. For each RH step, the equilibrium is reached in about 3-4 hours. During the first step at 10% RH, the mass tends to decrease for all the samples before stabilization. The loss of mass, occurring at the very beginning of DVS measurements, is due to desorption of the excess of water of the sample with respect to the equilibrium content at 10%RH. This loss was taken into account to establish the initial mass of dry samples. In the successive





From Figure 4.24- [redacted], the sorption and desorption isotherms can be extracted plotting the value of the mass change achieved at equilibrium as a function of the imposed relative humidity (Figure 4.26).





All the samples show reversible absorption/ desorption of water in the probed RH range with almost null hysteresis, as the absorption/desorption isotherms are coincident (Figure 4.26). The null hysteresis indicates that no irreversible structural changes occur in the adopted experiment conditions for DVS experiments. According to the classification described in section 4.1.8, the sorption/desorption isotherms for [REDACTED] films, follow a behavior of the second type. The process is controlled by the mutual interactions between the polymer and the permeant molecules.

[REDACTED]

[REDACTED]

[REDACTED]

[REDACTED]

[REDACTED]

[REDACTED]

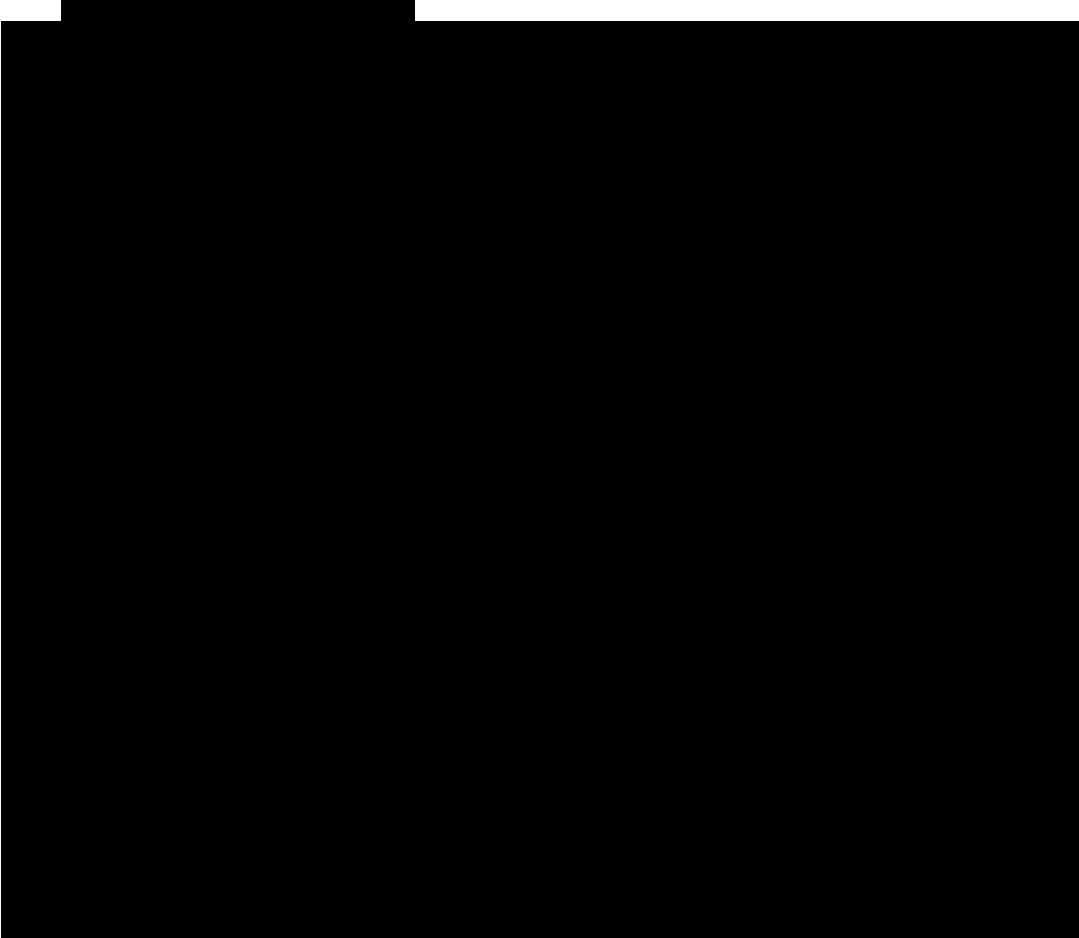
[REDACTED]

[REDACTED]

[REDACTED]

[REDACTED]

particular, the time profiles at each incremental DVS step is obtained plotting as a function of  $t_{1/2}$ , the mass increment at each step  $i$ ,  $M_i(t) - M_i(0)/M_i(\infty)$ , with  $M_i(0)$  and  $M_i(\infty)$  the mass achieved by the sample at the beginning and at the end of each step. A non-Fickian diffusion regime is observed for all the samples at low RH conditions. However, with increasing RH values, the absorption process can be approximated to a Fickian behavior. Since the non-linear part of each curve, corresponding to the non Fickian behavior, is small, the apparent diffusion coefficient,  $D^*$ , can be evaluated by eq. 4.34, after determination of the value of  $(t^{1/2})^*$  by graphical



C

D

[REDACTED]

[REDACTED]

The observed differences in the values of apparent diffusion coefficient,  $D^*$ , among the samples reflect the different composition [REDACTED], in terms of molecular mass, degree of hydrolysis and presence of [REDACTED]

[REDACTED]

It is worth noting that the values of the apparent diffusion coefficient  $D^*$ , deduced by gravimetry in the preceding paragraph during the desorption process of water for specimens obtained by direct addition of water in the case of the [REDACTED] are in close agreement with those measured by DVS, even though the values obtained with the two techniques may not be directly correlated. We recall that desorption is conducted in atmospheric conditions at (non-controlled) average RH conditions of  $\approx 50\%$ . Hence, the good agreement suggests that during the absorption/desorption experiments no irreversible microstructural transformations occur for the PVA based systems.

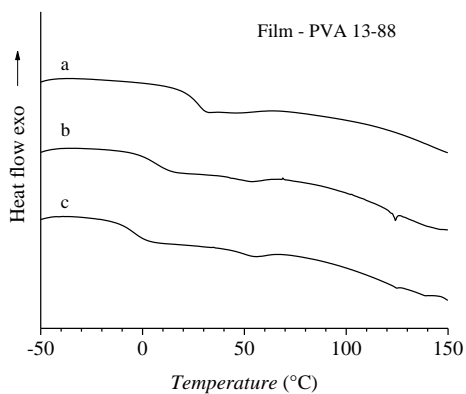
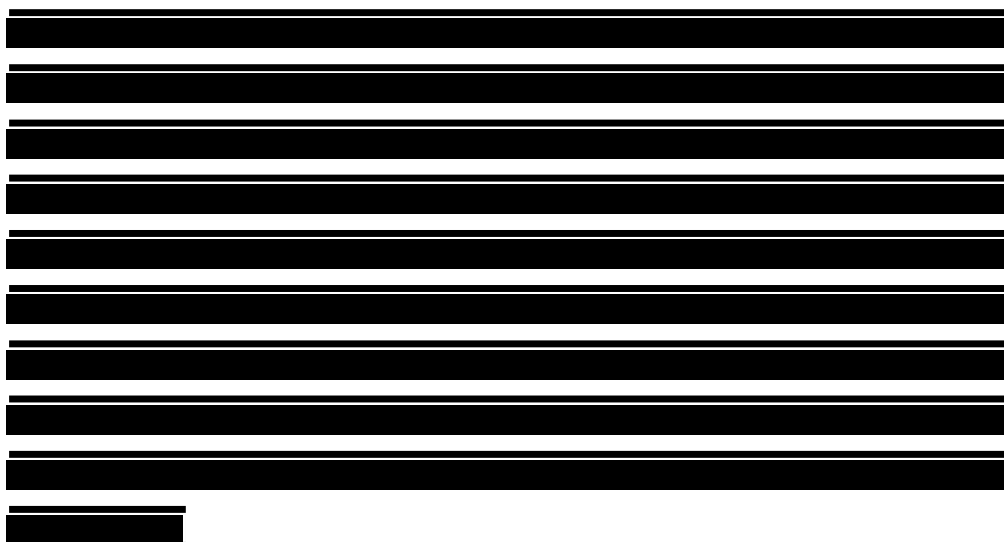
The apparent diffusion coefficients of vapors are usually found to be dependent on the penetrant concentration, controlled in our case through the external RH. The complex behavior of our samples may be explained by the concomitant effect of two processes. The first effect involves the progressive dissolution of PVA crystals with increasing the amount of the absorbed water and the



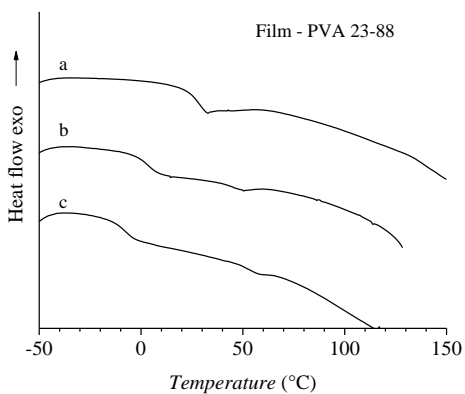
consequent increase of the amorphous fraction, which is more permeable to the solvent. The second effect involves the plasticizing action of water toward the amorphous PVA. This induces a variation of the segmental jumping frequency related to the free volume of the polymer-penetrant mixture. Consequently, the rates of diffusion increase with diffusant concentration.

#### 4.2.5 Plasticizing effect of water on glass transition temperature

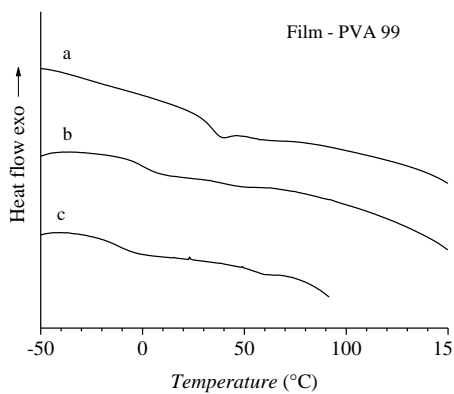
The glass transition temperatures were investigated for PVA films at different water content. Films of pure resin were obtained by water casting solutions. The selected thickness is  $\approx 80\mu\text{m}$ , [REDACTED]. [REDACTED] The casting procedure is described in section 2.1.1. To obtain films at controlled water content, dry films were exposed at different relative humidity (RH) for 16 hours, using the procedure described in section 2.1.3. After the water absorption, the samples were tested by means of DSC into hermetically sealed aluminum pans to avoid loss of water. Each pan was weighted after the thermal analysis to check the final water content. Heating scans at rate of  $10^\circ\text{C}/\text{min}$  from  $-70$  or  $-150$  to  $150^\circ\text{C}$  were carried out to individuate the  $T_g$  (Figure 4.29). As shown in [REDACTED]  $T_g$  decreases as the water content increases. This behavior can be explained assuming the plasticizing effect of water on the polymeric matrix. Moreover, the sample PVA A is characterized by higher transition temperature with respect to the other samples in the explored conditions, in agreement with the strong inter- and intra-chain interactions established by the charged groups, which increase the stiffness of the chains. The data were fitted with eq. 4.26, fixing the glass transition of water as  $-138^\circ\text{C}$  [32]. The fitting parameters are reported in Table 4.6.



**A**



**B**



**C**

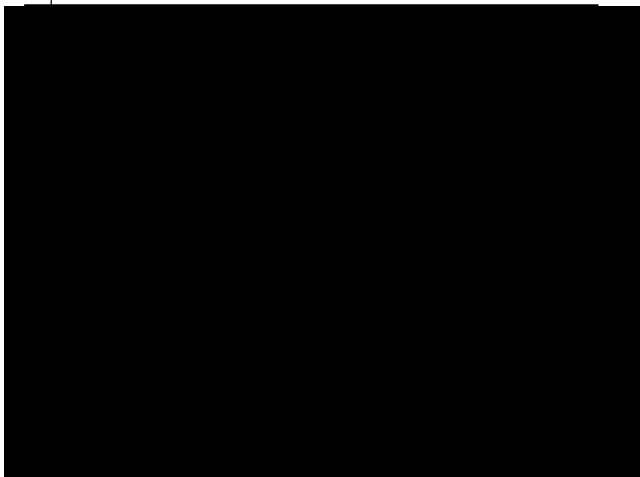
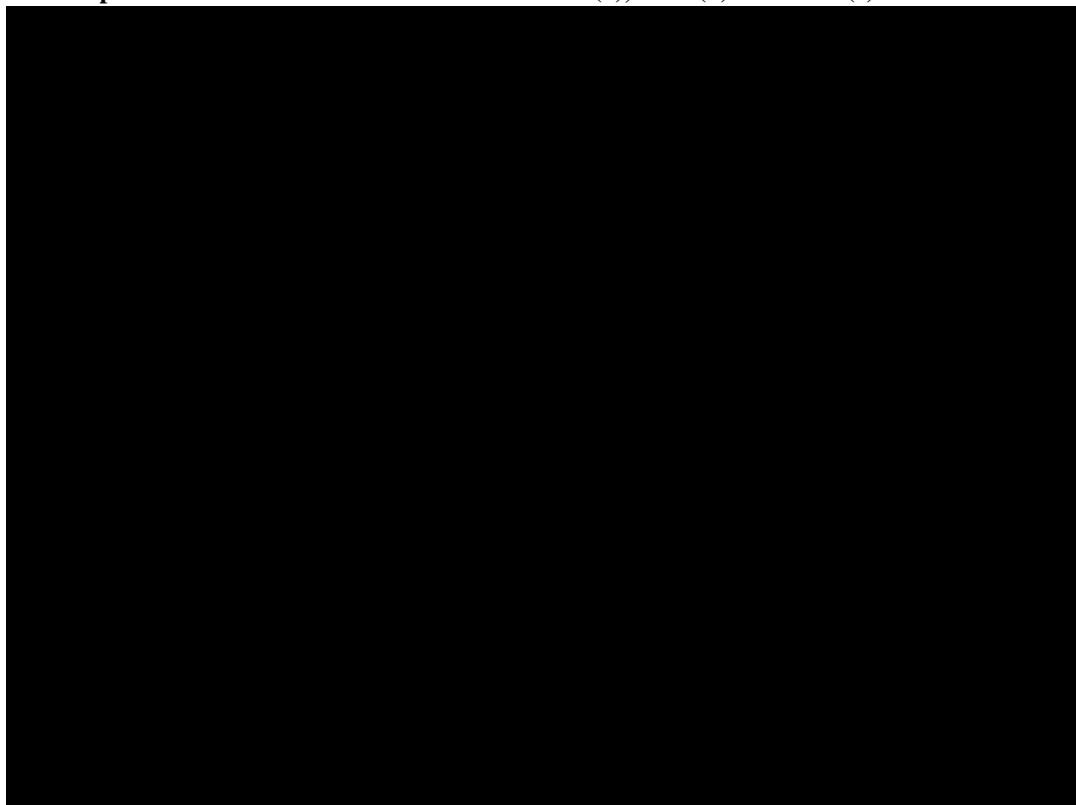


Figure 4.29: DSC thermograms from -70 to 150°C, at scanning rate of 10°C/min, recorded for films, obtained by casting water solutions of the resins PVA 23-88 (A), PVA 13-88 (B), PVA 99 (C) and [REDACTED] (D). The specimens were tested in sealed pans after exposition for 16 hours at different RH: 45% (a), 66% (b) and 79% (c).



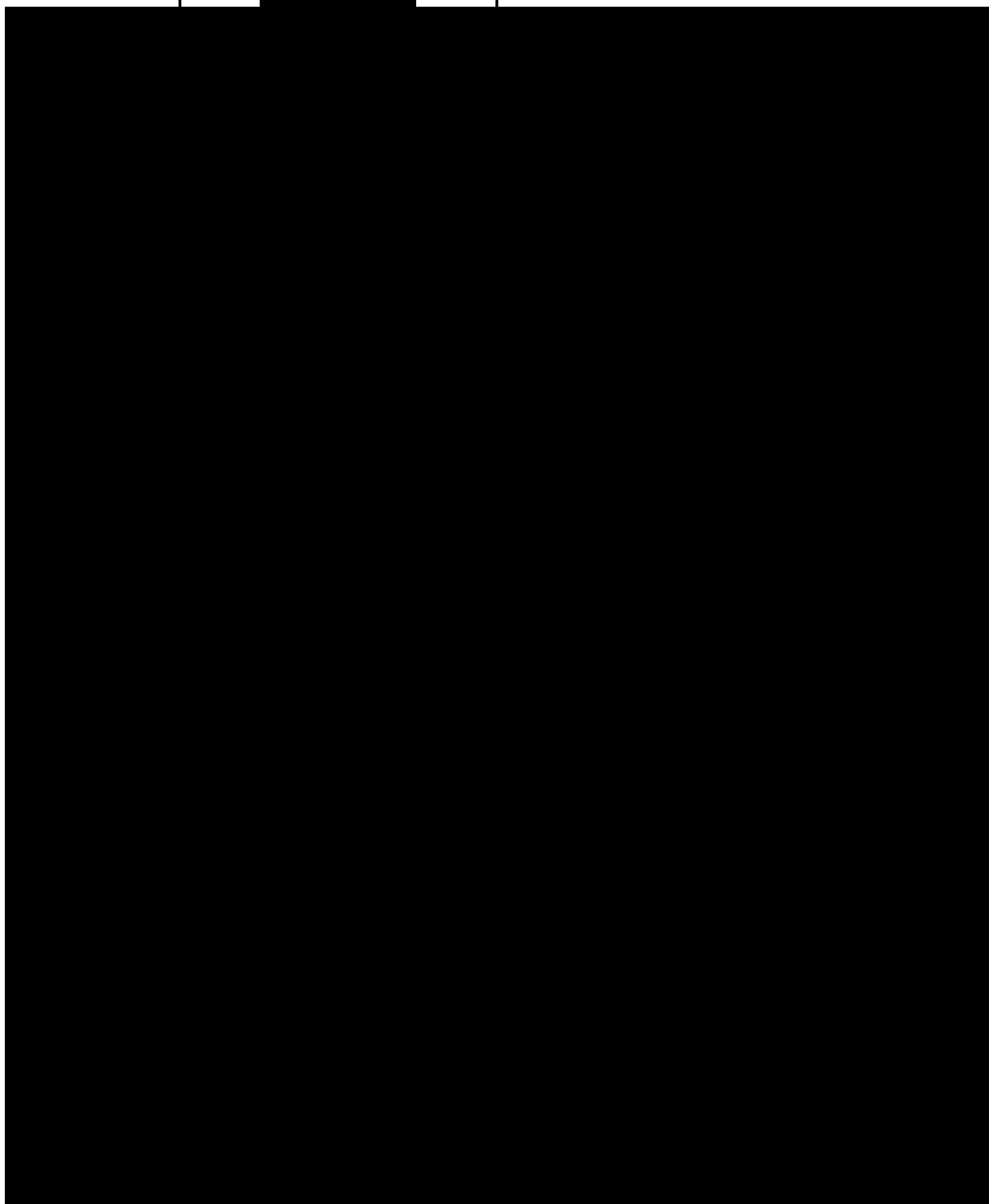
Casting Films of PVA resin samples		RH treatment			
		0	45	66	79
PVA 99	Water content ( $m_w/m_{PVA}$ )%	0	6.0	15.0	18.0
	$T_g$ (°C)	70.0	34.0	-1.3	-14.3
PVA 13-88	Water content ( $m_w/m_{PVA}$ )%	0	8.0	14.0	18.0
	$T_g$ (°C)	66.0	26.0	6.7	-5.0

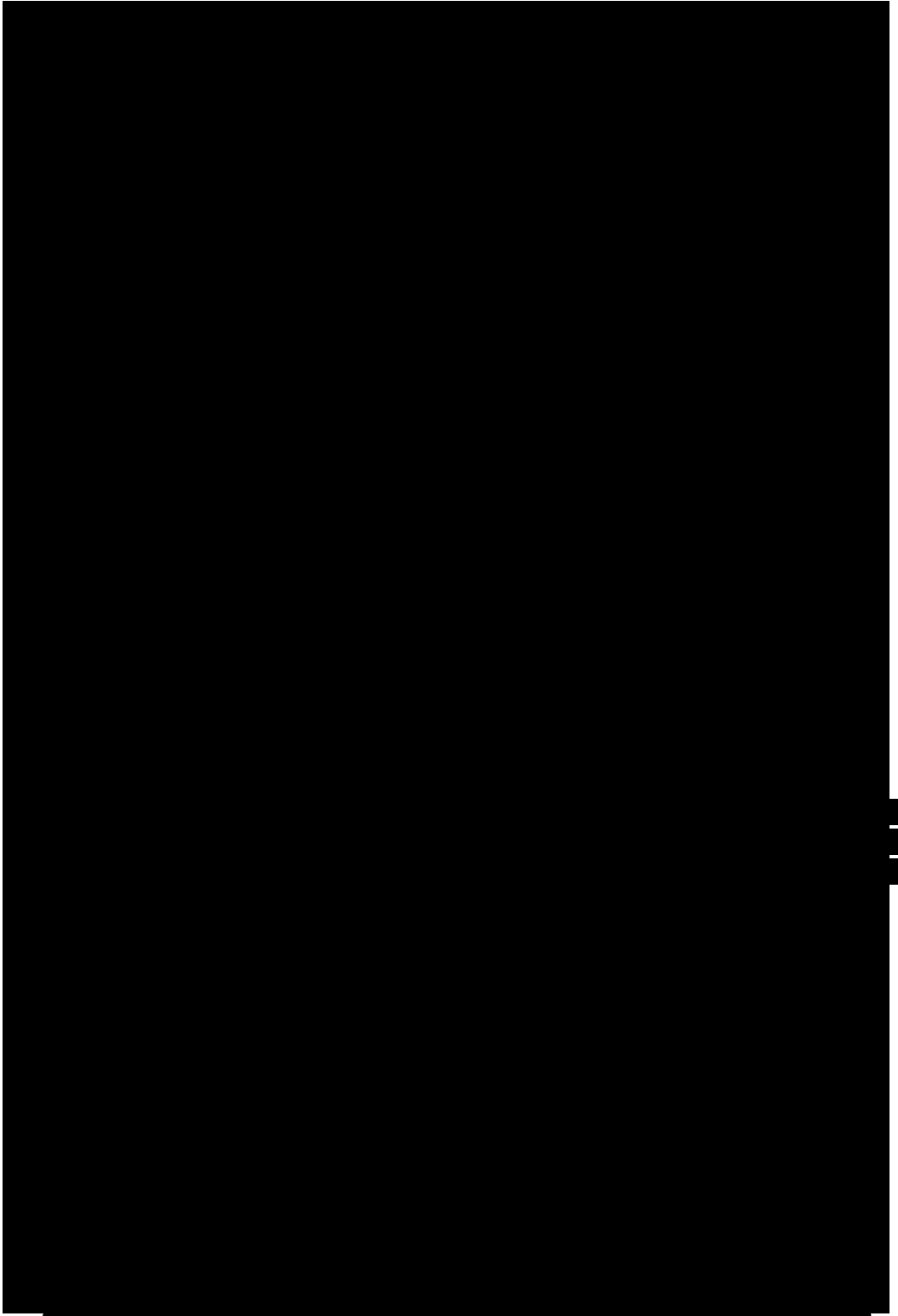
---

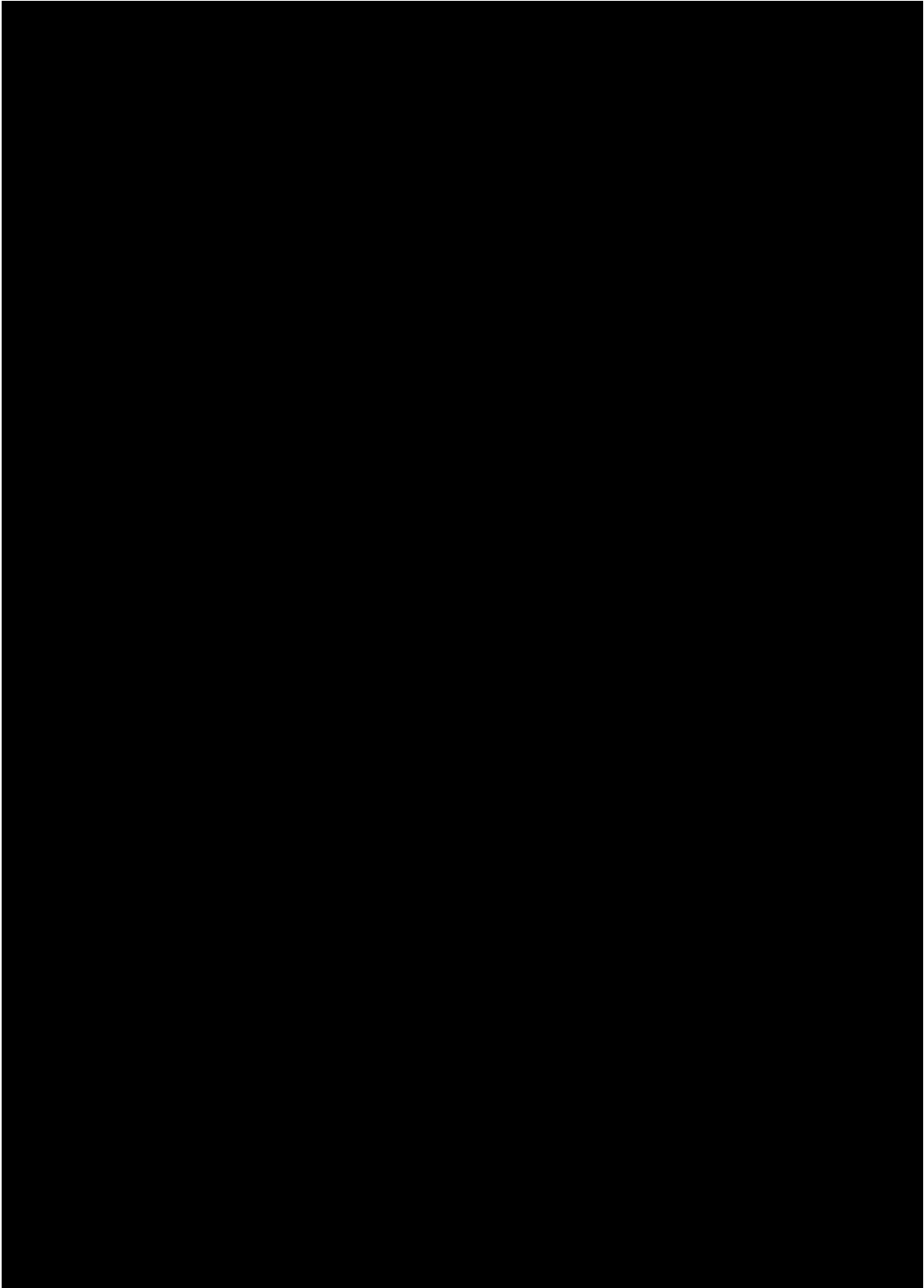
---

PVA 23-88	<b>Water content</b> <i>(m<sub>w</sub>/m<sub>PVA</sub>)%</i>	0	8.0	13.0	18.0
	<i>T<sub>g</sub></i> (°C)	67.0	28.0	3.5	-8.4

---







**Table 4.6: Fitting parameters obtained by fitting the data of [REDACTED] B with eq. 4.26.**

	PVA resins sample			
	PVA 23-88	PVA 13-88	PVA 99	[REDACTED]
$T_{g,l}$	$67 \pm 2$	$65 \pm 2$	$69 \pm 2$	[REDACTED]
$k$	$0.36 \pm 0.02$	$0.40 \pm 0.02$	$0.33 \pm 0.01$	[REDACTED]


## 4.2.6 Effect of water absorption on mechanical properties of PVA films

The effect of water as plasticizer was also observed testing the mechanical properties of the samples. After exposition of the samples at controlled humidity conditions, up to achieve the equilibrium absorption of water, the stress-strain curves for samples at different water contents were recorded in a closed chamber maintained at the same humidity conditions. The RH and the temperature were monitored during each experiment and kept constant. The stress-strain curves are shown in [REDACTED]

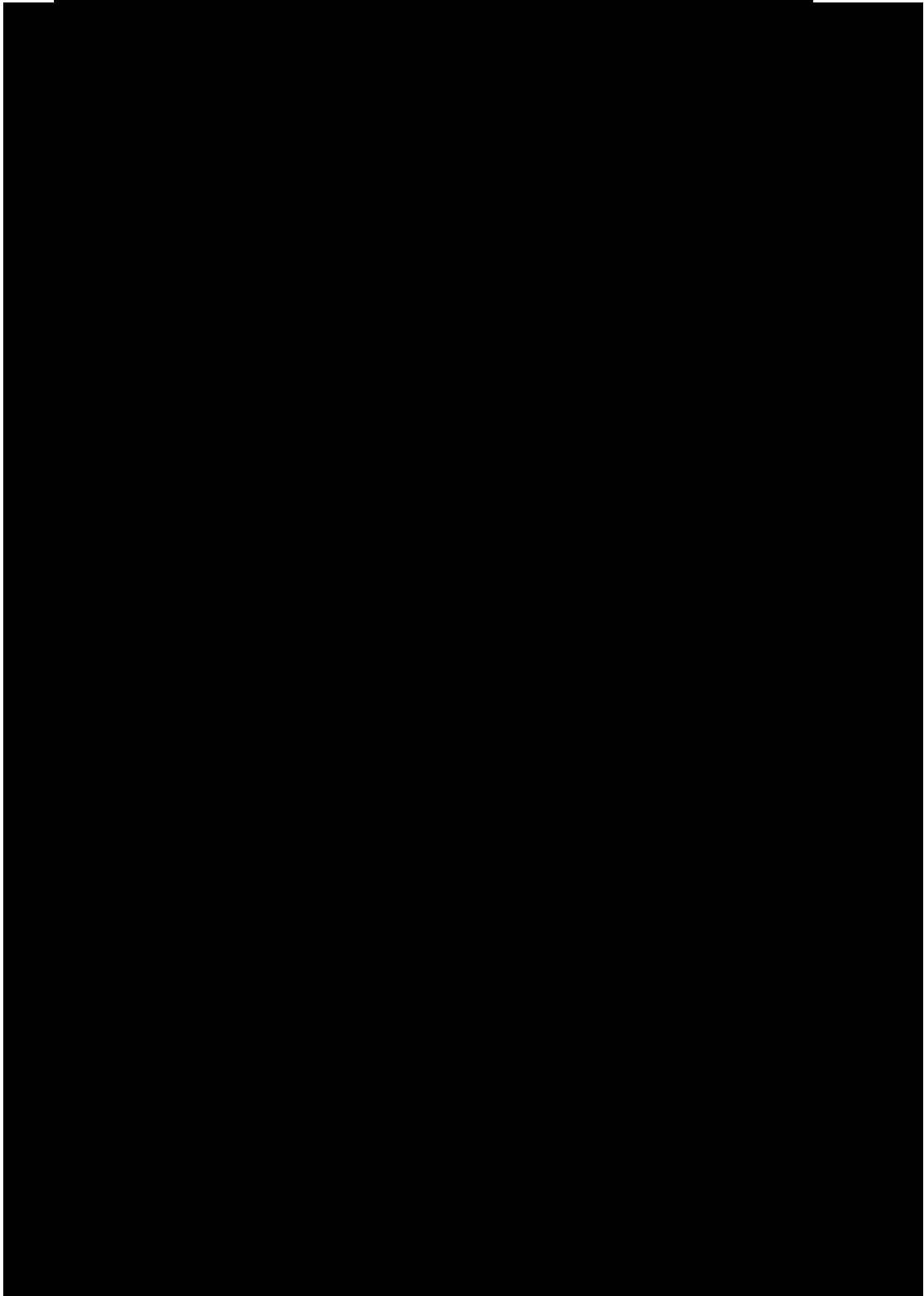
The values of the Young's modulus ( $E$ ), elongation at yield ( $\epsilon_y$ ) and yield stress ( $\sigma_y$ ) as function of water uptake are reported in [REDACTED] and in Table 4.7. Negative value of the weight change corresponds to samples dried at 80°C for 16 hours and then stored in presence of silica gel, which lose up to 20% of their initial weight, because of loss of solvent and/or additives. The value of

modulus decreases, as the water uptake increases, in agreement with the decrease of crystallinity by effect of water [REDACTED]. For high values of absorbed water the samples show almost elastomeric behavior. The yield point, instead, is shifted at high value of elongation and lower stress, and becomes gradually less marked. This result is due to the plasticizing effect of water. As evidenced from WAXS analysis, the water, which is initially absorbed by the amorphous phase, induces also a decrease of the crystallinity, as it acts dissolving the PVA crystals. Therefore, the decrease of Young modulus, is also due to the decrease of crystallinity with increase of water uptake.

The results of the present analysis indicate that the PVA films are able to keep a relatively high mechanical strength even after absorption of high quantities of water.











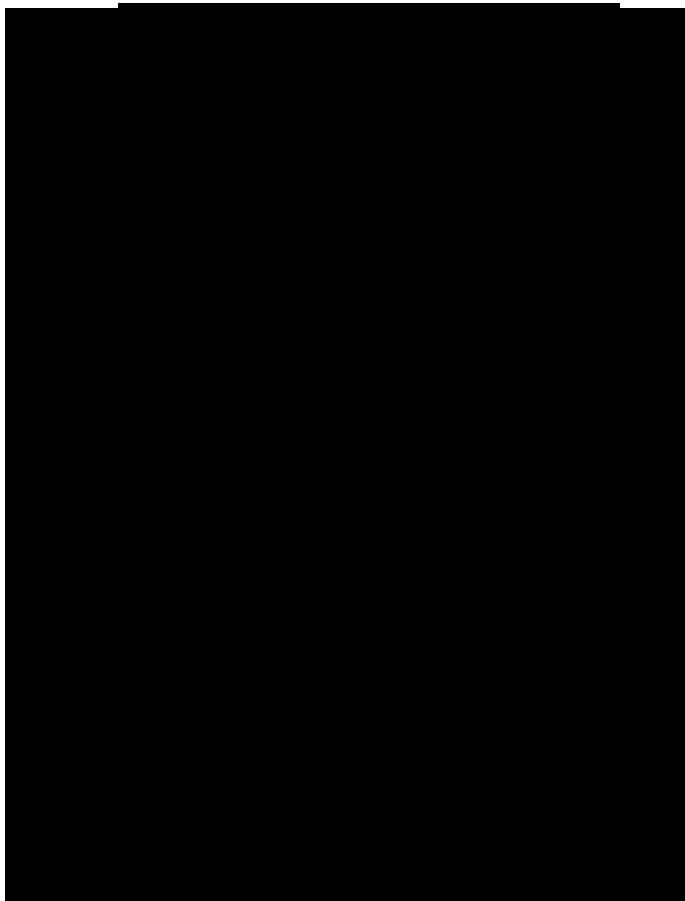


[REDACTED]

[REDACTED]

[REDACTED]





[Redacted text block consisting of multiple lines of blacked-out content]









### 4.3 Conclusion to Chapter 4

The main results of this section can be summarized as it follows. The analyzed PVA resins and [REDACTED] a high tendency to adsorb high quantities of water. All sample contain about 40-50 wt% of non-freezable water strongly interacting with the polymer matrix. SAXS analysis indicate that water is well dispersed at molecular scale in PVA samples. [REDACTED]

[REDACTED] The correlation peak due to lamellar stacking, instead, progressively shifts toward lower angular positions, up to disappear, by addition of increasing amount of water. Simultaneously also the Bragg peaks disappear, indicating that water acts dissolving PVA crystals. Upon water evaporation, the PVA sample recrystallize. The re-crystallization process occurs almost simultaneously with the loss of the water. [REDACTED]

The sorption kinetics of water at vapor activity lower than 80%, was also measured, obtaining values for the apparent diffusion coefficient in agreement with those determined in the desorption experiments. Differences in absorption kinetics and absorption isotherms for the different samples may be ascribed to the difference in molecular mass, degree of PVA hydrolysis, [REDACTED]

Water also influences the glass transition temperature and the mechanical properties of PVA samples. Therefore, the role of water as plasticizing agent, as swelling agent of PVA chains, and its ability to completely dissolve the PVA crystals at concentration of 60wt% is highlighted. These data suggest that the amorphization of PVA, by addition of water, should be an important step in the welding process.

---

## References

- [1] R. B. Bird, W. E. Stewart, and E. N. Lightfoot, *Transport phenomena*. New York, 1960.
- [2] M. H. Cohen and D. Turnbull, "Molecular Transport in Liquids and Glasses," *J. Chem. Phys.*, vol. 31, no. 5, pp. 1164–1169, 1959.
- [3] J. S. Vrentas and C. M. Vrentas, "Evaluation of Free-Volume Theories for Solvent Self-Diffusion in Polymer-Solvent Systems," *J. Polym. Sci. Part B Polym. Phys.*, vol. 31, pp. 69–76, 1993.
- [4] N. Ramesh and J. L. Duda, "Diffusion in Polymers below the Glass Transition Temperature: Comparison of Two Approaches Based on Free Volume Concepts," *Korean J. Chem. Eng.*, vol. 17, no. 3, pp. 310–317, 2000.
- [5] P. M. Budd, N. B. McKeown, and D. Fritsch, "Free volume and intrinsic microporosity in polymers," *J. Mater. Chem.*, vol. 15, no. 20, pp. 1977–1986, 2005.
- [6] A. Peterlin, "Dependence of diffusive transport on morphology of crystalline polymers," *J. Macromol. Sci. Part B Phys.*, no. B11(1), pp. 57–87, 1975.
- [7] J. L. Duda and J. M. Zielinski, "Free Volume Theory," in *Diffusion in Polymers*, P. Neogi, Ed. New York, 1996, p. 143.
- [8] R. H. Lacombe and I. C. Sanchez, "Statistical thermodynamics of fluid mixtures," *J. Phys. Chem.*, vol. 80, no. 23, pp. 2568–2580, 1976.
- [9] I. C. Sanchez and R. H. Lacombe, "An elementary molecular theory of classical fluids. Pure fluids," *J. Phys. Chem.*, vol. 80, no. 21, pp. 2352–2362, 1976.
- [10] I. C. Sanchez and R. H. Lacombe, "Statistical thermodynamics of

- polymer solutions,” *Macromolecules*, vol. 11, no. 6, pp. 1145–1156, 1978.
- [11] R. Simha and T. Somcynsky, “On the Statistical Thermodynamics of Spherical and Chain Molecule Fluids,” *Macromolecules*, vol. 2, no. 4, pp. 342–350, 1969.
- [12] C. Panayiotout and I. C. Sanchez, “Hydrogen Bonding in Fluids: An Equatio-of-State Approach,” *J. Phys. Chem.*, vol. 95, no. 24, pp. 10090–10097, 1991.
- [13] C. Panayiotou, M. Pantoula, E. Stefanis, I. Tsivintzelis, and I. G. Economou, “Nonrandom Hydrogen-Bonding Model of Fluids and Their Mixtures . 1 . Pure Fluids,” *Ind. Eng. Chem. Res.*, vol. 43, pp. 6592–6606, 2004.
- [14] J. Crank, *The mathematics of diffusion*, Clarendon. Oxford, 1975.
- [15] F. Preda, A. Bocahut, L. Fillot, D. R. Long, and P. Sotta, “Investigation of Water Diffusion Mechanisms in Relation to Polymer Relaxations in Polyamides,” *Macromolecules*, vol. 48, pp. 5730–5741, 2015.
- [16] T. J. Alfrey, E. F. Gurnee, and W. G. Lloyd, “Diffusion in glassy polymers,” ... *Sci. Part A-2 Polym. ....*, vol. 12, pp. 249–261, 1966.
- [17] R. A. Grinsted, L. Clark, and J. L. Koenig, “Study of Cyclic Sorption-Desorption into Poly(methyl methacrylate) Rods Using NMR Imaging,” pp. 1235–1241, 1992.
- [18] N. . Thomas and A. . Windle, “A theory of case II diffusion,” *Polymer*, vol. 23, no. 4, pp. 529–542, Apr. 1982.
- [19] N. Thomas and A. H. Windle, “Transport of methanol in poly(methyl methacrylate),” *Polymer*, vol. 19, no. 3, pp. 255–265, 1978.
- [20] N. Thomas and A. H. Windle, “Discontinuous shape changes associated with Case II transport of methanol in thin sheets of PMMA,” *Polymer*,

- vol. 18, no. 11, p. 1195, 1977.
- [21] T. Wang, T. Kwei, and H. Frisch, "Diffusion in glassy polymers. II," *J. Polym. Sci. Part A-2*, vol. 7, pp. 879–887, 1969.
- [22] A. Peterlin, "Diffusion in a network with discontinuous swelling," *Polym. Lett.*, vol. 3, pp. 1083–1087, 1965.
- [23] A. Peterlin, "Diffusion in a Glassy Polymer with Discontinuous Swelling II. Concentration Distribution of Diffusant as function of time," *Die Makromol. Chemie*, vol. 124, no. 3009, pp. 136–142, 1969.
- [24] A. Peterlin, "Diffusion with discontinuous swelling. V. Type II diffusion into sheets and spheres," *J. Polym. Sci. Polym. Phys. Ed.*, vol. 17, no. 10, pp. 1741–1756, Oct. 1979.
- [25] C. H. M. Jacques, H. B. Hopfenberg, and V. Stannet, *Permeability of Plastic Films and Coatings to Gases, Vapors, and Liquids*, Plenum., vol. 6. New York, 1974.
- [26] G. Astarita and G. C. Sarti, "A class of mathematical models for sorption of swelling solvents in glassy polymers," *Polym. Eng. Sci.*, vol. 18, no. 5, pp. 388–395, Apr. 1978.
- [27] P. J. Flory, "Flory theory for Polymers," in *Principles of Polymer Chemistry*, Cornell Un., Ithaca, 1953.
- [28] I. Blume, E. Smit, M. Wessling, and C. A. Smolders, "Diffusion through rubbery and glassy polymer membranes," *Makromol. Chemie. Macromol. Symp.*, vol. 45, no. 1, pp. 237–257, 1991.
- [29] W. Vieth and W. F. Wuerth, "Transport properties and their correlation with the morphology of thermally conditioned polypropylene," *J. Appl. Polym. Sci.*, vol. 13, no. 4, pp. 685–712, 1969.
- [30] M. Gordon and J. S. Taylor, "Ideal copolymers and the second-order transitions of synthetic rubbers. I. non-crystalline copolymers," *J. Appl.*

- Chem.*, vol. 2, no. 9, pp. 493–500, 1952.
- [31] F. N. Kelley and F. Bueche, “Viscosity and glass temperature relations for polymer-diluent systems,” *J. Polym. Sci.*, vol. 50, no. 154, pp. 549–556, 1961.
- [32] P. G. Debenedetti and E. H. Stanley, “Supercooled and glassy water,” *Phys. Today*, vol. 56, no. 6, pp. 40–16, 2003.
- [33] S. Ichihara, “Glass Transition Temperature of Homogeneous Blends and Copolymers,” *Polym. J.*, vol. 32, pp. 823–827, 2000.
- [34] Z. H. Ping, Q. T. Nguyen, S. M. Chen, J. Q. Zhou, and Y. D. Ding, “States of water in different hydrophilic polymers - DSC and FTIR studies,” *Polymer.*, vol. 42, no. 20, pp. 8461–8467, 2001.
- [35] G. R. Filho and W. A. Bueno, “Water state of Cuprophan (hemodialysis membrane),” *J. Memb. Sci.*, vol. 74, no. 1–2, pp. 19–27, 1992.
- [36] J. R. Scherer, G. F. Bailey, S. Kint, R. Young, D. P. Malladi, and B. Bolton, “Water in polymer membranes. 4. Raman scattering from cellulose acetate films,” *J. Phys. Chem.*, vol. 89, no. 2, pp. 312–319, 1985.
- [37] A. Seidlitz and T. Albrecht, “Small-Angle X-ray Scattering for morphological analysis of semicrystalline polymers,” in *Polymer Morphology: Principles, Characterization and Processing*, John Wiley., Q. Guo, Ed. New York, 2016, pp. 153–163.
- [38] V. Papadopoulou, K. Kosmidis, M. Vlachou, and P. Macheras, “On the use of the Weibull function for the discernment of drug release mechanisms,” *Int. J. Pharm.*, vol. 309, no. 1–2, pp. 44–50, 2006.
- [39] O. Ismail, “Peleg and Weibull models for water absorption of copolymer gels crosslinked on polyethylene glycol dimethacrylates,” *Res. Chem. Intermed.*, vol. 40, no. 4, pp. 1327–1335, 2014.



- [40] K. S. Fancey, "A latch-based weibull model for polymerie creep and recovery," *J. Polym. Eng.*, vol. 21, no. 6, pp. 489–510, 2001.
- [41] K. H. Ramteke, P. A. Dighe, A. R. Kharat, and S. V. Patil, "Mathematical Models of Drug Dissolution: A Review," *Sch. Acad. J. PharmacyOnline) Sch. Acad. J. Pharm*, vol. 3, no. 5, pp. 388–396, 2014.
- [42] P. Costa and J. M. S. Lobo, "Modelling and Comparison of Dissolution Profiles," *Eur. J. Pharm. Sci.*, vol. 13, pp. 123–133, 2001.
- [43] S. Sastry, P. G. Debenedetti, and F. H. Stillinger, "Signatures of distinct dynamical regimes in the energy landscape of a glass-forming liquid," *Nature*, vol. 393, pp. 554–557, 1998.



# Chapter 5

## Polymer diffusion investigated by rheological tools

*I am among those who think that science has great beauty.  
A scientist in his laboratory is not only a technician:  
He is also a child placed before natural phenomena,  
which impress him like a fairy tale.*

*Marie Curie*

## 5.1 Introduction

The sealing process of two polymeric films of polyvinyl-alcohol (PVA) in presence of water is driven by the dynamics of polymer chains at the interfacial region. The process involves coating of a PVA film with a layer of water and successive coupling of the wet film with a second PVA film on the top of it. As PVA is readily dissolved by water a thin layer of PVA/water solution is formed at the surface in the first instants of coating. For this reason, it is of interest to study the diffusion process of PVA chain in water as a function of concentration. This study is faced resorting a rheological investigation of PVA solutions at relevant concentrations, emulating the local concentration of PVA in the water layers in the first 10 min after coating and before sealing, corresponding to  $\approx 8\text{-}15\text{wt}\%$  of PVA.

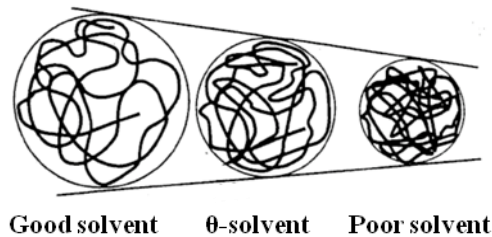
### 5.1.1 Polymeric solutions

In the last decades, polymeric solutions have offered a flourishing field of research because of their practical applications, arousing the interest to the fundamental understanding of their properties. In this scenario, PVA has a prominent role as water soluble polymer.

Many efforts have been made by several researchers to model the diffusion phenomena occurring in polymer solutions and to validate an unified theory at different concentration regimes for different polymers [1]–[4]. The behavior is related to parameters such as the temperature, concentration, nature of the solvent, flexibility of chains and the polymer-solvent interactions.

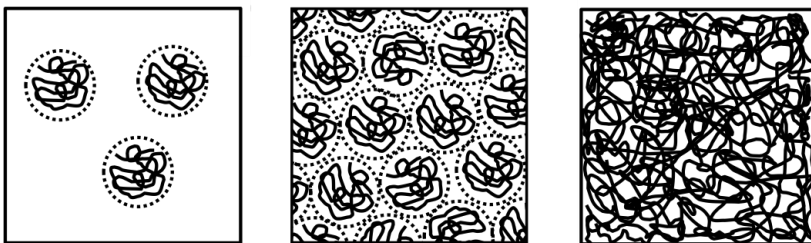
Polymer chains in solutions usually adopt a random coil conformation [5], with size dependent on the competition between polymer/polymer, solvent/solvent and polymer/solvent interactions (Figure 5.1). If the

interactions between polymer segments and solvent molecules are energetically favorable, the polymer coil tends to swell. This is the case of a *good solvent*. From the point of view of interactions involving the sole segments belonging to a single polymer chain, repulsive forces prevail and the coil dimension becomes large because of the excluded volume effect. On the contrary, in a *poor solvent*, polymer-polymer interactions are preferred and the chain is led to assume a compact set of conformations. The solvent, for which the excluded volume effect is cancelled, due to slightly unfavorable polymer-solvent interactions, is called  $\theta$ -solvent. This condition is satisfied for a certain temperature, named  $\theta$ -temperature.



**Figure 5.1:** Polymer random coil in *good*,  $\theta$  and *poor* solvent.

Moreover, according to the concentration, polymers in solutions behave differently. Graessley [6] classified polymer solutions behavior into different concentration regimes: dilute, semi-dilute and concentrated regimes (Figure 5.2). The existence of different behaviors can be interpreted considering the increase of intermolecular interactions with increasing concentration.





where  $N_A$  is the Avogadro number. The regime near the *overlap concentration* ( $c \approx c^*$ ) corresponds to the semi-diluted regime which is modelled by the Rouse theory [10]. This model describes polymer chains interacting without forming entanglements. The viscosity of the polymer solution and relaxation time increase with the concentration according to the following scaling laws:

$$\eta \propto c^{\frac{1}{3 \cdot v - 1}} \quad \text{eq. 5.4}$$

$$\tau \propto c^{\frac{2 - 3 \cdot v}{3 \cdot v - 1}} \quad \text{eq. 5.5}$$

where  $v$  is a dimensionless scaling exponent related to the volume occupied by the coil in solution: usually  $v = 0.5$  in a  $\theta$ -solvent and 0.588 in good solvent. Thus, the value of the exponent for the viscosity is 1.3 and 2, respectively, in case of *good* and  $\theta$  solvent, while for the relaxation time the exponent is typically 0.3 in a *good* solvent and 1 in a  $\theta$  solvent.

If  $c \gg c^*$ , the coils can no longer remain individual and become prone to form entanglements (Figure 5.2-C). The concentration at which the entangled regime starts is named entanglement concentration,  $c_e$ . Together with  $c^*$ , these crossover concentrations can be evaluated by the variation of scaling laws. As shown in section 1.2, the *reptation* theory for entangled systems, introduced by de Gennes [11], [12], provides a good interpretation of the chain diffusion in melt and in concentrated solutions. In this regime, according to the Doi-Edwards tube model, developed on the basis of the *reptation* theory, the motion of a chain is confined in a tube defined by entanglement and the power law dependence of viscosity on the concentration, in the case of a *good* solvent becomes:

$$\eta \propto c^{\frac{3}{3 \cdot v - 1}} \propto c^{3.75} \quad \text{eq. 5.6}$$

whereas, in the case of a  $\theta$ -solvent:

$$\eta \propto c^{4.7} \quad \text{eq. 5.7}$$

Finally, the behavior of the chain relaxation is described in a *good* solvent by:

$$\tau \propto c^{\frac{3-3\nu}{3\nu-1}} \propto c^3 \quad \text{eq. 5.8}$$

and in a  $\theta$ -solvent by:

$$\tau \propto c^{\frac{7}{3}} \quad \text{eq. 5.9}$$

However, the tube model can underestimate the molar mass dependence of viscosity and relaxation time, resulting in exponents higher than those predicted by theory for the description of experimental data.

## 5.2 Experimental approach

An investigation of rheological properties of PVA-water solutions was carried out with the aim to identify the characteristic relaxation times of PVA chains in the resins. In particular, the effect of concentration and of the molecular mass on relaxation time was studied. This characteristic time is directly related to the mobility of chains at the interface.

The longest relaxation time of a polymer can be simply determined as the inverse of the angular frequency at which the elastic modulus  $G'$  and viscous modulus  $G''$  moduli cross each other, that is the frequency at which the rubbery behavior regime ends and the viscous flow of the chains starts. In order to determine the crossover frequency, dynamical mechanical measurements by means of a rotational rheometer were performed in the linear viscoelastic regime, over a certain range of frequencies.

[REDACTED]

[REDACTED]

[REDACTED]

[REDACTED]

[REDACTED]

[REDACTED]

[REDACTED]



Moreover, to individuate the cross-over concentrations,  $c^*$  and  $c_e$ , viscosity measurements through mechanical rheometer were carried out.

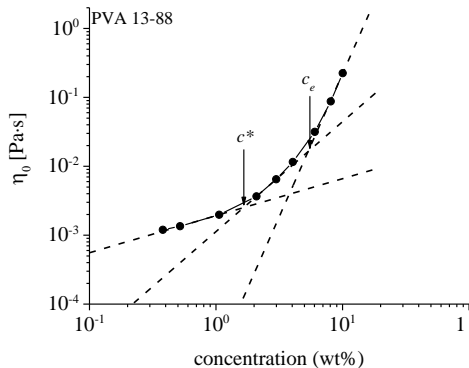
### 5.3 Experimental results

Water solutions of three PVA resins (PVA 23-88, PVA 13-88 and PVA A) at different concentrations were analyzed. We recall that the first two resins have the same degree of hydrolysis (88%)

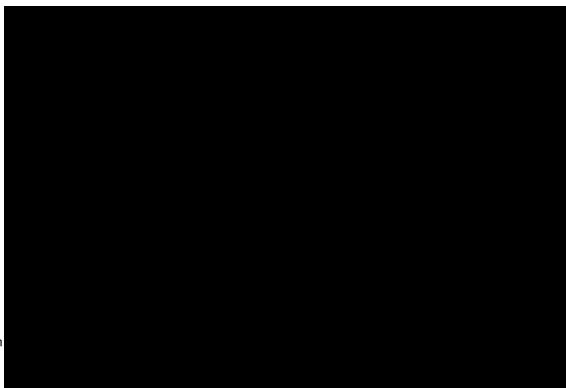
The sample PVA 23-88 has a higher degree of polymerization than those of the other resins and, thus, a higher molecular mass. Technical information on the used experimental setup and about the procedure adopted to prepare the samples for both techniques are provided in sections 2.2.9-2.2.10.

In Figure 5.3 the values of zero shear rate viscosity,  $\eta_0$ , are reported as a function of the concentration for the three samples. Three regimes can be identified on the basis of the power law dependence of  $\eta_0$  on the concentration

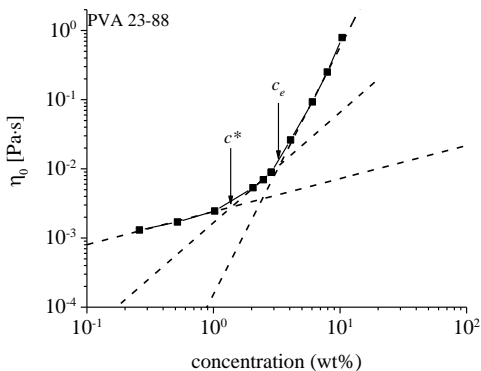
(Table 5.1).



A



B



C

Figure 5.3: Zero shear viscosity,  $\eta_0$ , as a function of PVA concentration (wt%) for the samples PVA 23-88 (A), PVA 13-88 (B) and [redacted] dissolved in water. Dashed lines are the fit to the data according to a power law of concentration.

Table 5.1: Values of the exponents,  $n$ , in the scaling law  $\eta \propto c^n$ , obtained by fitting the data of Figure 5.3 in the three identified regimes, and extrapolated values of overlap concentration,  $c^*$ , and entanglement concentration,  $c_e$ .

Sample	$n$ (dilute regime)	$n$ (semi-dilute regime)	$n$ (concentrated regime)	$c^*$ (wt%)	$c_e$ (wt%)
PVA 13-88	$0.53 \pm 0.04$	$1.79 \pm 0.08$	$4.1 \pm 0.3$	1.8	5.4
PVA 23-88	$0.48 \pm 0.05$	$1.80 \pm 0.07$	$4.1 \pm 0.3$	1.3	3.4
[redacted]	[redacted]	[redacted]	[redacted]	[redacted]	[redacted]

At low concentrations, the viscosity smoothly increases up to a limiting concentration value, according to a power law dependence on the PVA concentration with an exponent,  $n$ , of about 0.5 for PVA 23-88 and 13-88 [15].

These values are lower than the expected values for dilute regime in a good solvent (about 1) and appear to be closer to the values described by the Fuoss law for charged systems of polyelectrolyte solutions in absence of salts ( $\eta \propto c^{0.5}$ ) [16]. The weak variation of  $\eta$  in this first regime can suggest that the interactions between chains are strongly attenuated by the presence of the solvent molecules forming hydrogen bonds with the OH groups of PVA.

In the intermediate regime, the exponents become 1.8 for PVA 23-88/13-88 [15]. The observed values are close to the scaling exponents reported for semi-dilute regime in a  $\theta$  solvent. It is worth noting that for a  $\theta$ -solvent,  $\eta$  is proportional to  $c^2$ , indicating that in the samples PVA 23-88 and 13-88, even if water is a good solvent, mutual interactions between the chains start to be preferred with respect to solvent/polymer interactions, starting to exclude water molecules from the coil.

Finally, in the third range of concentration, a steep increase of the slope is observed with exponents of about 4 for the samples PVA 23-88 and 13-88 [15]. The samples PVA 23-88 and 13-88 show values slightly higher than the value of 3.75 proposed for polymers in a good solvent. Similar scaling exponents have been reported for associating polymers [17], where the intramolecular interaction are replaced by intermolecular interactions, causing a power law dependence of viscosity on the concentration higher than 3.75. Such behavior has been observed in other polymer solutions in good solvent [18].

The concentration at crossover between the different regimes correspond to  $c^*$ , the overlap concentration, and  $c_e$ , the concentration marking the onset of formation of entanglements. The overlap concentration  $c^*$  of PVA is 1.3wt% for the sample PVA 23-88 with the highest molecular mass and increases to 1.8 and 1.5 for the resins with lower molecular mass PVA 13-88 [REDACTED]

The values of  $c_e$ , instead, are 3wt % for the sample at highest molecular mass, PVA 23-88, and around 5 wt% for PVA 13-88 [REDACTED]

The values of viscosity of the resins are compared in [REDACTED] The values of zero shear rate viscosity of the sample PVA 13-88 are lower than those of sample PVA 23-88, regardless of concentration, in agreement with lower molecular mass. [REDACTED]

[REDACTED] regime are higher than those of the samples PVA 23-88 and PVA 13-88, whereas in the semi-dilute regime, they are in between. In the third regime, [REDACTED]

[REDACTED]

[REDACTED]

[REDACTED]

[REDACTED]

[REDACTED]

[REDACTED]

In an alternative approach, the viscosity data of PVA solutions can be fitted resorting to an empirical approach devised in ref. [19] and [20], based on the use of a simple equation valid over the whole concentration range, virtually containing no fitting parameters, as it depends on the characteristic length scales of the polymer itself in solution.

According to this approach, the key parameters that control the viscosity of a polymer solution across the dilute, semi-dilute and concentrated regimes are the hydrodynamic and gyration radii of a single coil ( $R_h$  and  $R_g$ , respectively) and the correlation length  $\xi$ , that is, in semidilute polymer solutions, the distance over which local fluctuations of monomer concentration persist, which is equivalent to the average distance between entanglements (mesh size), or to the distance over which hydrodynamic interactions are screened (screening length) [6].

The universal equation describing the effect of concentration on the viscosity over the whole concentration range for a polymer solution is:

$$\frac{\eta_0}{\eta_s} = \exp \left[ \frac{\gamma}{RT} \left( \frac{R_h}{R_g} \right)^\alpha \left( \frac{c}{c^*} \right)^{\alpha\beta} + D \right] \quad \text{eq. 5.10}$$

where  $\eta_s$  is the dynamic viscosity of the solvent ( $\eta_s = 8.9 \cdot 10^{-4}$  Pa s for pure water at 25°C),  $\gamma$  is a system-dependent parameter expressed in terms of energy,  $R$  the gas constant,  $\beta$  a scaling exponent (for a three-dimensional polymer coil in a good solvent  $\beta=3/4$ ) and  $\alpha$  is a parameter connected with the regime of polymer concentration, different for entangled and non-entangled systems. It is approximated as  $\beta-1$  in non-entangled solutions and  $R_h R_g^{-1} \beta^{-1}$  in the entangled ones [19], [20]. Finally  $D$  is equal to zero for non-charged polymers, and non zero for charged polymer chains.

In eq. 5.11 the quantity in the exponent  $R_g \left( \frac{c}{c^*} \right)^{-\beta}$  corresponds to the correlation length  $\xi$ , that is:

$$\xi = R_g \left( \frac{c}{c^*} \right)^{-\beta} \quad \text{eq. 5.11}$$

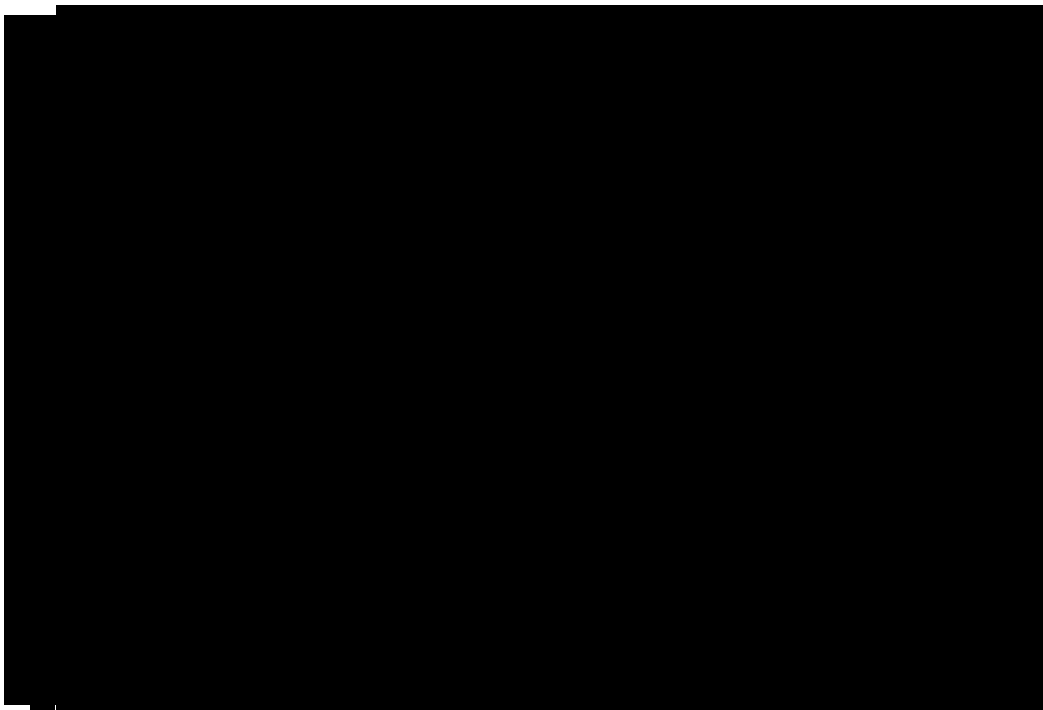
In practice, eq. 5.10 accounts for the effect of chain entanglement on viscosity treating the viscous flow as an activated process, following the Eyring rate theory.[21], [22]. The analogy with the Eyring's rate theory emerges considering that for uncharged polymers ( $D=0$ ) the exponent corresponds to an activation energy  $\Delta E_a$  ( $= \frac{\gamma}{RT} \left( \frac{R_h}{R_g} \right)^a \left( \frac{c}{c^*} \right)^{\alpha\beta}$ ), suggesting that the viscosity scaling can be written in terms of the Arrhenius equation as:

$$\eta_0 = \eta_s \exp \left[ - \frac{\Delta E_a}{RT} \right] \quad \text{eq. 5.12}$$

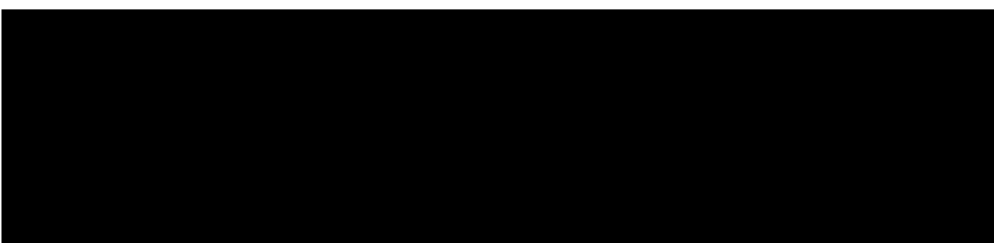
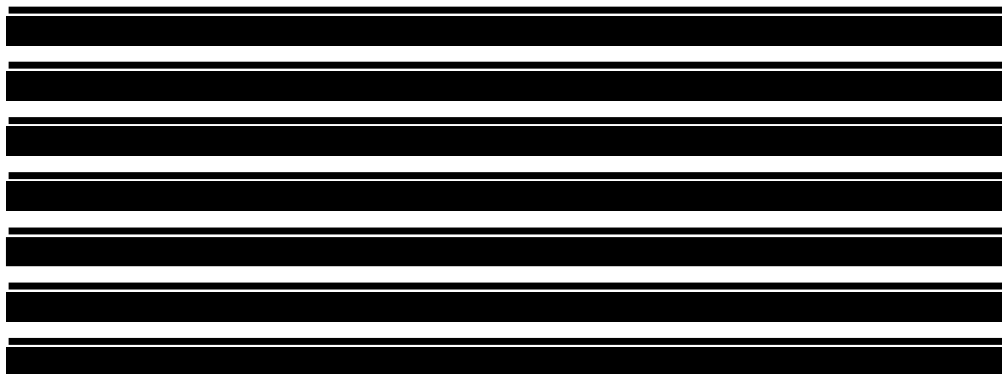
In the lack of precise measurements of the hydrodynamic and gyration radii of a single coil ( $R_h$  and  $R_g$ , respectively), the viscosity data of PVA resins of Figure 5.4 may be fitted to eq. 5.10, by setting  $B = \frac{\gamma}{RT} \left( \frac{R_h}{R_g} \right)^a \left( \frac{1}{c^*} \right)^A$  and  $A = \alpha\beta$ , using the following reduced equation:

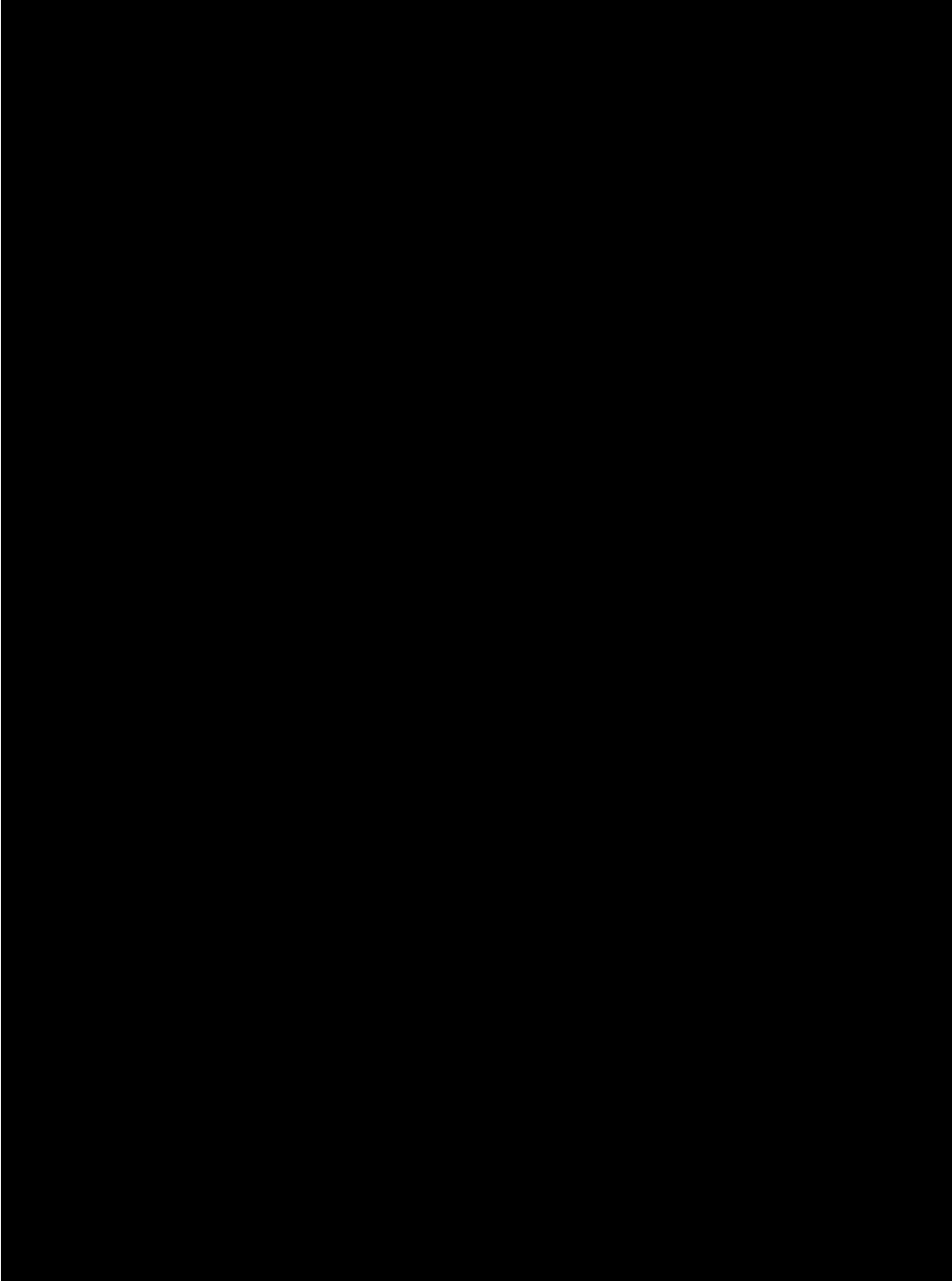
$$\ln \left( \frac{\eta_0}{\eta_s} \right) = B c^A + D \quad \text{eq. 5.13}$$

The fit to the data with eq. 5.13 is shown in Figure 5.5. Values of  $A \approx 0.8$ ,  $B = 0.7-1$  are obtained by setting  $D = 0$  in the case of solutions of uncharged samples PVA 23-88 and PVA 13-88 and  $D = 0.54$



The values of the elastic ( $G'$ ) and the viscous ( $G''$ ) moduli as a function of the angular frequency for water solutions of PVA resins are reported in Figure 5.6 The data were obtained at low frequencies by using classical rheology and at high frequencies using DWS measurements. Measurements are performed for solutions in the concentration range 7.5-20wt% of PVA. In all cases, the explored range evidences a crossover between  $G'$  and  $G''$ .







[REDACTED]

[REDACTED]

[REDACTED]

[REDACTED]

[Redacted text]

[Redacted text]

[Redacted text]

[Redacted text]

[Redacted text]

[Redacted text]

[Redacted text]

[Redacted text]

[Redacted text]

[Redacted text]

[Redacted text]

[Redacted text]

[Redacted text]

[Redacted text]

[Redacted text]

[Redacted text block]

[Redacted text block]

[Redacted text block]

[Redacted text block]

[Redacted text block]

[Redacted text block]

## 5.4 Conclusions to Chapter 5

In this section the rheological properties of PVA in water solutions is probed, encompassing a wide-range of concentration, from the dilute to concentrated regimes. In particular, measurements of the effect of PVA concentration on the zero shear rate viscosity  $\eta_0$  were interpreted in terms of classical approach of  $\eta_0$  dependence on a power law of concentration, and using a generalized phenomenological model with virtually no fitting parameter, based on the Eyring concept that viscosity is a thermally activated process.

The viscosity measurements allowed identifying for the different resins the concentration regimes marking the overlap concentration, and the concentration at onset of entanglement formation.

Rheological measurements indicate that the longest relaxation time for PVA chain in water solutions at relevant concentration for the welding process is of  $\approx 3$  ms. More precisely, this relaxation times, which is indicative of the mobility of the chains, depend on the polymer concentration, molecular mass,  $\dots$  of PVA chains, secondary interactions among the chains. Characteristic times of the order of ms entail that the chain dynamics is much faster than PVA re-crystallization process, taking place in hours.

## References

- [1] Y. Liu, Y. Jun, and V. Steinberg, “Concentration dependence of the longest relaxation times of dilute and semi-dilute polymer solutions,” *J. Rheol. (N. Y. N. Y.)*, vol. 53, no. 5, pp. 1069–1085, 2009.
- [2] Z. Zhou and P. J. Daivis, “Molecular dynamics study of polymer conformation as a function of concentration and solvent quality,” *J. Chem. Phys.*, vol. 130, no. 22, pp. 1–10, 2009.
- [3] A. V Dobrynin, R. H. Colby, and M. Rubinstein, “Scaling Theory of Polyelectrolyte Solutions,” *Macromolecules*, vol. 28, no. 6, pp. 1859–1871, 1995.
- [4] F. Del Giudice, S. J. Haward, and A. Q. Shen, “Relaxation time of dilute polymer solutions: A microfluidic approach,” *J. Rheol. (N. Y. N. Y.)*, vol. 61, no. 2, pp. 327–337, 2017.
- [5] M. Rubinstein and R. H. Colby, *Polymer Physics*, Oxford Uni. New York, 2003.
- [6] W. W. Graessley, *The Entanglement Concept in Polymer Rheology*. .
- [7] B. H. Zimm, “Dynamics of polymer molecules in dilute solution: Viscoelasticity, flow birefringence and dielectric loss,” *J. Chem. Phys.*, vol. 24, no. 2, pp. 269–278, 1956.
- [8] M. Muthukumar, “Concentration dependent relaxation times of linear polymers in dilute solutions,” *Macromolecules*, vol. 17, no. 4, pp. 971–973, 1984.
- [9] S. F. Doi, M.; Edwards, *The Theory of Polymer Dynamics*. Clarendon Press: Oxford, U.K., 1986.
- [10] P. E. Rouse, “A theory of the linear viscoelastic properties of dilute solutions of coiling polymers,” *J. Chem. Phys.*, vol. 21, no. 1, pp. 1272–

- 1280, 1953.
- [11] P. G. De Gennes, "Reptation of a polymer chain in the presence of fixed obstacles," *J. Chem. Phys.*, vol. 55, no. 2, pp. 572–579, 1971.
- [12] F. Brochard and P. G. De Gennes, "Polymer-Polymer Interdiffusion," *Europhys. Lett.*, vol. 1, no. 5, pp. 221–224, 1986.
- [13] F. C. C. MacKintosh and C. F. F. Schmidt, "Microrheology," *Curr. Opin. Colloid Interface Sci.*, vol. 4, no. 4, pp. 300–307, 1999.
- [14] T. Narita, K. Mayumi, and G. Ducouret, "Viscoelastic properties of poly(vinyl alcohol) hydrogels having permanent and transient cross-links studied by microrheology, classical rheometry, and dynamic light scattering," *Macromolecules*, vol. 46, no. 10, pp. 4174–4183, 2013.
- [15] T. Narita, A. Knaebel, J. P. Munch, M. Zrínyi, and S. J. Candau, "Microrheology of chemically crosslinked polymer gels by diffusing-wave spectroscopy," *Macromol. Symp.*, vol. 207, pp. 17–30, 2004.
- [16] M. Fuoss, "Polyelectrolites," *Discuss. Faraday J.*, vol. 11, pp. 125–134, 1951.
- [17] M. Rubinstein and A. N. Semenov, "Dynamics of entangled solutions of associating polymers," *Macromolecules*, vol. 34, no. 4, pp. 1058–1068, 2001.
- [18] T. Narita, A. Knaebel, J. P. Munch, and S. J. Candau, "Microrheology of poly(vinyl alcohol) aqueous solutions and chemically cross-linked gels," *Macromolecules*, vol. 34, no. 23, pp. 8224–8231, 2001.
- [19] A. Wisniewska, K. Sozanski, T. Kalwarczyk, K. Kedra-Krolik, and R. Holyst, "Scaling Equation for Viscosity of Polymer Mixtures in Solutions with Application to Diffusion of Molecular Probes," *Macromolecules*, vol. 50, no. 11, pp. 4555–4561, 2017.
- [20] A. Wiśniewska, K. Sozański, T. Kalwarczyk, K. Kędra-Królik, C.

- Pieper, S. A. Wieczorek, S. Jakiela, J. Enderlein, and R. Hołyst, “Scaling of activation energy for macroscopic flow in poly(ethylene glycol) solutions: Entangled - Non-entangled crossover,” *Polymer*, vol. 55, no. 18, pp. 4651–4657, 2014.
- [21] H. Eyring, “Viscosity, plasticity, and diffusion as examples of absolute reaction rates,” *J. Chem. Phys.*, vol. 4, no. 4, pp. 283–291, 1936.
- [22] R. E. Powell, W. E. Roseveare, and H. Eyring, “Diffusion, Thermal Conductivity, and Viscous Flow of Liquids,” *Ind. Eng. Chem.*, vol. 33, no. 4, pp. 430–435, 1941.



# Chapter 6

## Film adhesion

*We are stuck with technology  
when what we really want is just stuff that works.  
How do you recognize something that is still technology?  
A good clue is if it comes with a manual.  
Douglas Adams*





[REDACTED]

[REDACTED]

[REDACTED]

[REDACTED]

[REDACTED]

[Redacted]

[Redacted]

[Redacted]

[Redacted]

[Redacted]

[Redacted]

[Redacted]

[Redacted]

[Redacted]

[Redacted]

[Redacted]

[Redacted]

[Redacted]

[Redacted]

[Redacted]

[Redacted]

[Redacted]

[Redacted]

[Redacted]

[Redacted]

[Redacted]

[Redacted]

[Redacted]

[Redacted]

[Redacted]

[Redacted]

[REDACTED]

[REDACTED]

[REDACTED]

[REDACTED]

[REDACTED]

[REDACTED]

[REDACTED]

[REDACTED]

[REDACTED]

[REDACTED]

[REDACTED]

[REDACTED]

[REDACTED]

[REDACTED]

[REDACTED]

[REDACTED]

[REDACTED]

[REDACTED]

[REDACTED]

[REDACTED]

[REDACTED]

[REDACTED]

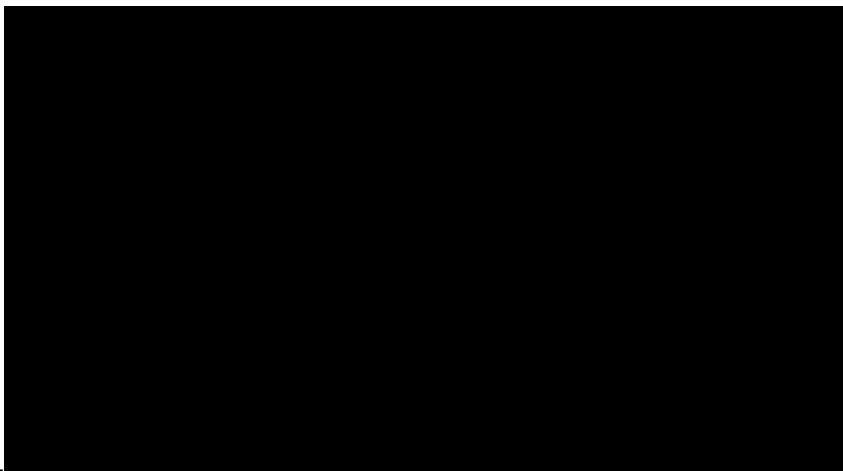
[REDACTED]

[REDACTED]





[Redacted text block]



[Redacted text block]

[Redacted text block]

[Redacted text block]

[Redacted text block]

[Redacted text block]

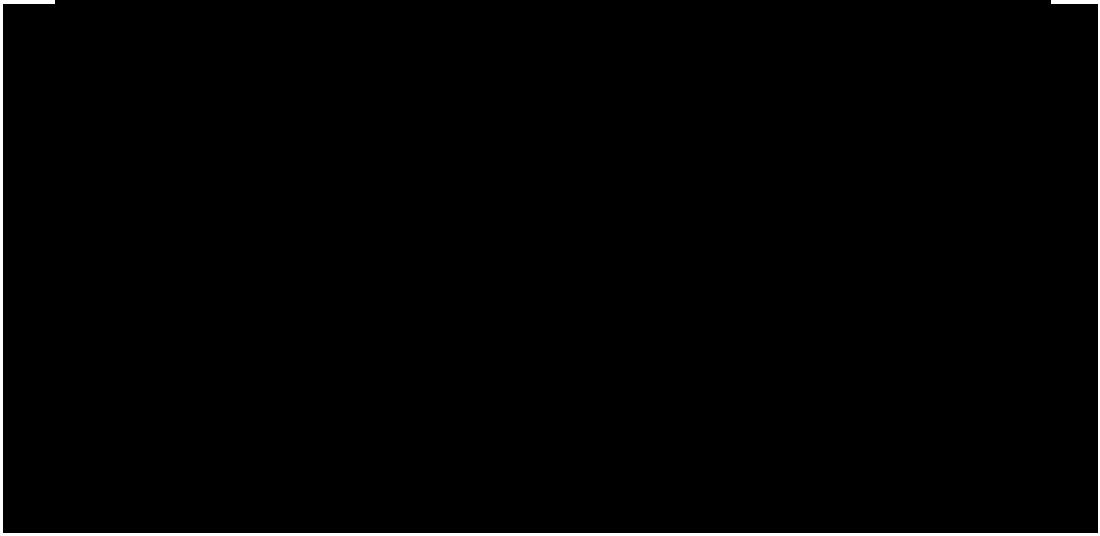
[Redacted text block]

[Redacted text block]

[Redacted text block]

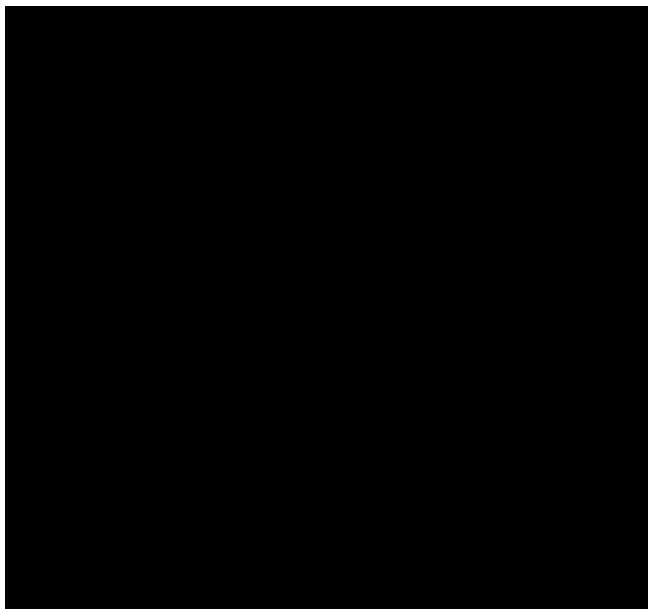






[Redacted text block consisting of multiple lines of blacked-out content]

[REDACTED]



[REDACTED]

[REDACTED]

[REDACTED]

[REDACTED]

[REDACTED]

[REDACTED]

[REDACTED]

[REDACTED]

[REDACTED]

[REDACTED]

[REDACTED]





# Conclusions

*One never notices what has been done;  
one can only see what remains to be done*

*Marie Curie*

## Conclusions

---

[REDACTED]

[REDACTED]

[REDACTED]



















[REDACTED]

[REDACTED]

[REDACTED]

[REDACTED]

[REDACTED]

[REDACTED]

[REDACTED]

[REDACTED]

[REDACTED]

[REDACTED]

[REDACTED]

[REDACTED]

[REDACTED]

[REDACTED]

[REDACTED]

[REDACTED]

[REDACTED]

[REDACTED]

[REDACTED]

[REDACTED]

[REDACTED]

[REDACTED]

[REDACTED]

[REDACTED]

[REDACTED]

[REDACTED]

[REDACTED]

[REDACTED]































Sequence Distribution in Vinyl Alcohol-Vinyl Acetate Copolymers,”  
*Macromolecules*, vol. 10, no. 3, pp. 532–535, 1977.

- [10] L. Greenspan, “Humidity fixed points of binary saturated aqueous solutions,” *J. Res. Natl. Bur. Stand. Sect. A Phys. Chem.*, vol. 81, no. 1, pp. 89–96, 1977.